9-2012

Retrieval of Sub-Pixel-Based Fire Intensity and its Application for Characterizing Smoke Injection Heights and Fire Weather in North America

David Peterson
University of Nebraska-Lincoln, david.peterson@huskers.unl.edu

RETRIEVAL OF SUB-PIXEL-BASED FIRE INTENSITY AND ITS APPLICATION FOR CHARACTERIZING SMOKE INJECTION HEIGHTS AND FIRE WEATHER IN NORTH AMERICA

By

David A. Peterson

A DISSERTATION

Presented to the Faculty of

The Graduate College at the University of Nebraska

In Partial Fulfillment of Requirements

For the Degree of Doctor of Philosophy

Major: Earth and Atmospheric Sciences

(Meteorology/Climatology)

Under the Supervision of Professor Jun Wang

Lincoln, Nebraska

September, 2012

RETRIEVAL OF SUB-PIXEL-BASED FIRE INTENSITY AND ITS APPLICATION FOR CHARACTERIZING SMOKE INJECTION HEIGHTS AND FIRE WEATHER IN NORTH AMERICA

David A. Peterson, Ph.D.

University of Nebraska, 2012

Adviser: Jun Wang

For over two decades, satellite sensors have provided the locations of global fire activity with ever-increasing accuracy. However, the ability to measure fire intensity, know as fire radiative power (FRP), and its potential relationships to meteorology and smoke plume injection heights, are currently limited by the pixel resolution. This dissertation describes the development of a new, sub-pixel-based FRP calculation (FRP_f) for fire pixels detected by the MODerate Resolution Imaging Spectroradiometer (MODIS) fire detection algorithm (Collection 5), which is subsequently applied to several large wildfire events in North America. The methodology inherits an earlier bi-spectral algorithm for retrieving sub-pixel fire area and temperature, but also makes a new and important advancement for the derivation of FRP_f by accounting for solar and atmospheric effects as a function of Earth-satellite geometry at the MODIS fire detection channels. The retrieved fire (flaming) area is assessed using high-resolution airborne data (3-50 meters), and shows that the FRP_f, in combination with retrieved fire area, allows a large fire burning at a low intensity to be separated from a small fire burning at a high intensity. While variations in the atmospheric profile may increase the potential for error, the algorithm is much more sensitive to errors in 11 μm background brightness temperature, where an error of only 1.0 K may alter the retrieved fire area by an order of

magnitude or more. These sources of uncertainty can be reduced through the summation of individual pixel-level retrievals for large clusters of fire pixels, which can be defined based on the resolution of a mesoscale model grid. An independent test reveals that unlike the standard MODIS pixel-based FRP, the flux of FRP_f per fire pixel cluster, defined as FRP_f divided by the retrieved fire area, has a stronger and statistically significant correlation with surface (10-meter) wind speed ($R = 0.55$) and air temperature ($R = 0.77$), especially for large fire events. Comparisons between FRP_f flux and smoke plume height data, provided by the Multi-angle Imaging SpectroRadiometer (MISR), also produce a much stronger correlation ($R = 0.49$) compared to the current MODIS FRP ($R = 0.16$). These strong relationships, combined with additional applications in the North American boreal forest, uniquely demonstrate that FRP_f flux not only provides an enhanced characterization of fire weather, but is also an improved quantitative tool for identifying the thermal buoyancy required to estimate smoke plume heights. This information can be used to advance the prediction of smoke emissions and transport, especially when applied to the next generation of satellite sensors.

Dedication

To my parents, family, and friends for providing the unwavering encouragement and support that allowed me to accomplish my goals.

My parents, David and Diane Peterson.

Acknowledgements

First of all, none of this would have been possible without my family and friends. Special thanks to my parents, David and Diane, for your patience, support, and love.

While in grad school, I was very fortunate to be a part of a strong department and research group. I am especially thankful for the support, advice, and encouragement from my adviser, Dr. Jun Wang. His unwavering commitment to success provided me with a variety of opportunities that I never imagined were possible. I would also like to thank my committee members: Dr. Mark Anderson, Dr. John Lenters, and Dr. Bob Oglesby at the University of Nebraska – Lincoln, as well as Dr. Charles Ichoku at the NASA Goddard Space Flight Center for their constructive comments and encouragement. I thank Dr. David Watkins, our department chair, for advice, support, and making sure that Bessey Hall is an orderly and enjoyable place to work. I am also grateful to our secretaries, Tina Gray and Janelle Gerry, for logistical support. My appreciation goes to Laura Judd and Zhifeng Yang for their assistance in the later stages of this project, and to my fellow grad students for many fun experiences over the past few years.

Along with my committee members, Dr. Edward Hyer played a key role in my graduate studies, provided mentorship, and enabled me to spend a summer working alongside the talented scientists at the Naval Research Laboratory in beautiful Monterey, CA. I also acknowledge Luke Ellison for his programming expertise, as well as Dr. Lorraine Remer, Dr. Wilfrid Schroeder, Dr. Doug Westphal, Dr. Ralph Kahn, Maria Petrenko, and the many others who have given me scientific advice. We are all grateful to Vincent Ambrosia and the AMS wildfire measurement team at the NASA Ames Research Center for providing the airborne (AMS) fire data used in this study.

Grant and Fellowship Information

The NASA Earth and Space Science Fellowship funded this project from September 2009 to August 2012. The Naval Research Enterprise Intern Program, at the Naval Research Laboratory in Monterey, California, provided additional support during my visit in the summer of 2011. I am also grateful to the support from NASA's New Investigator Program and Radiation Science Program (to Dr. Jun Wang).

Statement of Originality

While I worked as part of several teams, this dissertation highlights my contribution to the satellite remote sensing and fire weather communities. This work has resulted in three first-authored papers (Peterson et al., 2012a, 2012b; Peterson and Wang, 2012), currently in various stages of the publication process, and was partially motivated by my Master's thesis (Peterson et al., 2010). In addition, this work was the focus of a variety of conference proceedings between 2010 and 2012. Any data or work provided by others is noted within this dissertation.

Table of Contents

List of Tables

List of Figures

Figure Page

Chapter 1. Background and Scope of the Dissertation

1.1 Introduction and Motivation

Observed in many regions of the globe, biomass burning is a key component to the Earth-atmosphere system, climate change, and operational forecasts of meteorology and air quality. Individual fires can be ignited by natural causes, such as lightning strikes (e.g. Peterson et al., 2010) or by anthropogenic causes, such as agriculture and forest clearing (e.g. Koren et al., 2007; van der Werf et al., 2008). Regardless of cause, these fires subsequently burn large tracts of land across the globe every year. For example, Roy et al. (2008) estimated that nearly 3.7 million square kilometers burned globally from July 2001 to June 2002. Wildfires also create concerns for air quality by releasing enormous amounts of aerosols and trace gases into the atmosphere (e.g. Spracklen et al., 2007; Jordan et al., 2008). Above the boundary layer, smoke particles can be transported thousands of miles (e.g. Westphal and Toon 1992; Damoah et al., 2005; Sapkota et al., 2005; Duck et al., 2007) creating health concerns and interacting with meteorological processes a great distance from a fire (e.g. Wang et al., 2006; Wang et al., 2012). In some cases, wildfires can even generate pyroconvection, which has been shown to inject smoke aerosols and trace gasses into the upper troposphere and even into the stratosphere (Fromm et al., 2010). In addition, deposition of fire-generated black carbon particles on ice sheets (e.g. Figure 1.1) has been shown to reduce the surface albedo causing atmospheric warming and increased melting (Randerson et al., 2006; Kopacz et al., 2011).

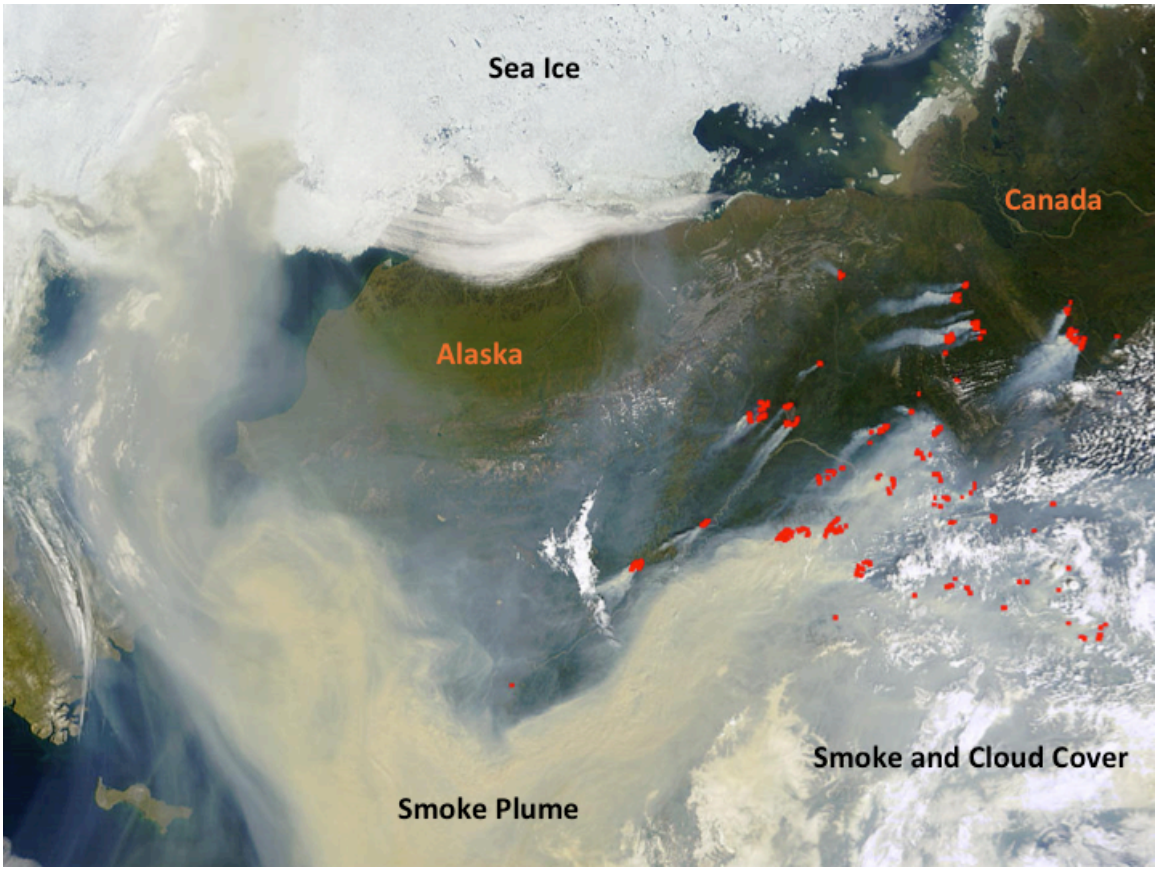

Figure 1.1: MODIS true color image for a large fire event in central Alaska on 01 July 2004. MODIS fire detections (fire pixels or counts) are displayed in red.

Over the past three decades, several satellite sensors have been able to provide observations of fire locations at different spatial scales and temporal frequencies. These include the NOAA Advanced Very High Radiometer (AVHRR), Geostationary Orbiting Environmental Satellite (GOES), Advanced Spaceborne Thermal Emission and Reflection Radiometer (ASTER), and the MODerate Resolution Imaging Spectroradiometer (MODIS). Some of these sensors also map burned areas. The MODIS sensor is especially important because (1) MODIS has the highest saturation temperature of ~500 K at its 4 μm fire detection channel (Justice et al., 2002; Kelha et al., 2003; Gao et al., 2007), which allows a high percentage of detected fires to be

characterized through fire radiative power (FRP) – a quantitative measure of fire intensity (Kaufman et al., 1998a), and (2) the twin MODIS sensors aboard the Terra (launched in 1999) and Aqua (launched in 2002) satellites allow wildfires to be observed globally up to four times each day; twice in the daytime and twice at night. Figure 1.1 shows an example true color MODIS image for a large fire event in central Alaska, highlighting fire pixel locations and their associated smoke plumes.

Even though a large region may be burned by a fire over its lifetime, only a portion of the burn area is actually in flames (fire front) at any given observation time (Lee and Tag, 1990; Kaufman et al., 1998a). Despite much advancement in fire remote sensing during the last couple of decades, all satellite sensors, including MODIS, provide fire locations as pixels that are flagged as containing fires (red dots in Figure 1.1). Unfortunately, the pixel resolution is usually too coarse to resolve the size of small fire hot spots that may be very intense relative to large, but low-intensity fires. As mentioned above, fire intensity is currently quantified using MODIS FRP, which is also proportional to both the fire's fuel consumption and smoke emission rates (e.g. Wooster et al., 2002, 2003, 2005; Ichoku and Kaufman 2005; Roberts et al., 2005, 2009; Ichoku et al., 2008a, 2008b; Jordan et al., 2008). Direct derivation of smoke emissions from satellite-based FRP can overcome the spatial errors in the traditional estimate of fire emission, in which the variation of land surface types within the sensor pixel play an important role (Hyer and Reid, 2009). Val Martin et al. (2010) further show that regions of intense burning (high FRP) commonly result in higher altitude smoke plumes and a greater chance of smoke transport into the free troposphere. However, similar to fire detections, the primary drawback for current MODIS FRP data is that they are estimates of fire radiative

power released over a pixel area. In reality, it is the rate of energy release over the fire area (the fire intensity, Byram, 1959) that is directly related to the thermal buoyancy (Lavoue et al., 2000; Kahn et al., 2007), which influences the smoke injection height and the transport of smoke plumes into the free troposphere. Therefore, the primary goal of this dissertation is to develop a sub-pixel-based retrieval of FRP, which may serve as a valuable addition to the current suite of satellite fire products.

1.1.1 The Need and Method for a Sub-Pixel-Based Calculation of FRP

In contrast to earlier sensors, MODIS is currently the only operational satellite sensor designed to specifically measure FRP globally (e.g. Kaufman et al., 1998a, 1998b; Ichoku et al., 2008a). Prior to MODIS Collection 5 (the current data version during this study), the MODIS fire detection algorithm retrieved FRP with respect to the individual pixel areas, or in units of Watts per pixel area (Kaufman et al., 1998a). In Collection 5, FRP is multiplied by the pixel area (FRP_p), and is provided in units of Megawatts. The specific MODIS FRP_p methodology dates back to the late 1990s (Kaufman et al. 1998a), and employs a best-fit equation for a wide variety of simulated burning scenarios (Figure 1.2). Drawing from this information, FRP_p is calculated for all fire pixels (top-of-atmosphere) using only the 4 μm channels:

$$FRP_p = 4.34 \times 10^{-19}(T_4^8 - T_{4b}^8)A_p \qquad (1.1)$$

where T_{4b} is the background brightness temperature (in K), T_4 is the brightness temperature of the fire pixel, and A_p is the area of the pixel (Kaufman et al., 1998a; 1998b, 2003; Giglio, 2010). Therefore, FRP_p in Collection 5 is a function of satellite viewing zenith angle. Regardless of data collection, FRP_p is useful for estimating the

total radiation from the fire, and consequently, may be related to the total amount of trace gases and particles emitted by the fire, which is useful for mesoscale modeling with a large model grid (e.g. Wang et al., 2006). In addition, FRP_p is currently being used for near real-time emissions maps at a global scale (Kaiser et al., 2009).

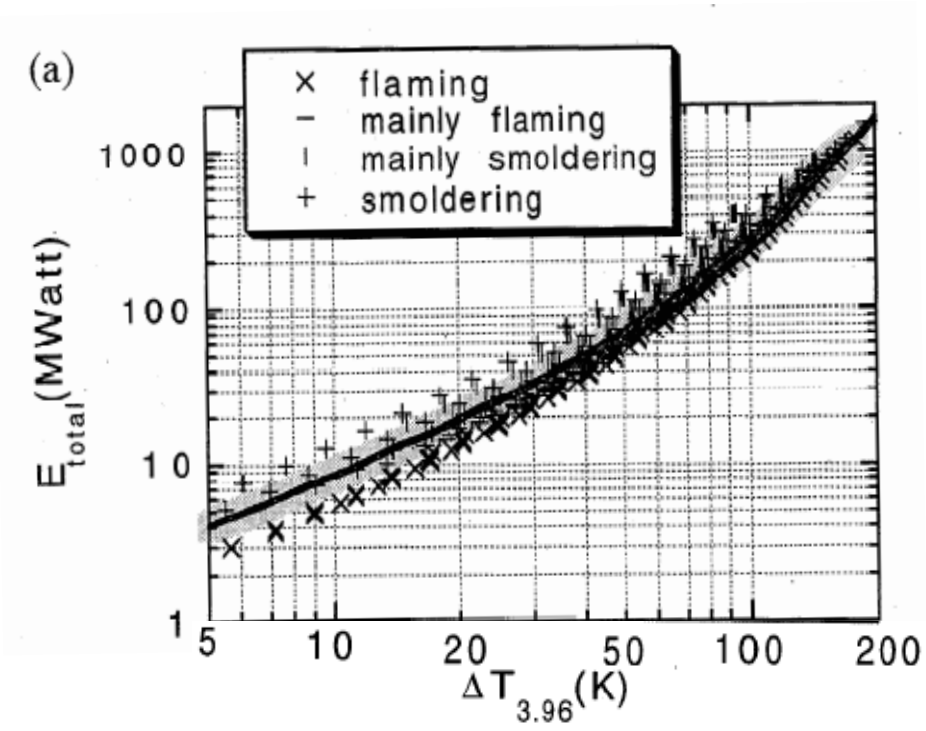

Figure 1.2: Relationship between the total energy emitted from the fire (E_{total} or FRP_p) and the difference between the temperature of the fire pixel and the surrounding background region at the primary 4 μm MODIS fire detection channel ($\Delta T_{3.96}$). This figure, adapted from Kaufman et al. (1998a), was constructed from thousands of fire simulations (denoted by each symbol) by varying the temperatures of the smoldering and flaming regions, as well as the fraction of the MODIS pixel covered by each of them. The solid black line indicates the resulting best-fit FRP_p approximation (equation 1.1).

While the use of FRP_p for estimating the fire emissions is well recognized (Vermote et al., 2009), its potential use for other applications, such as estimating smoke injection heights and fire intensity, is limited by the lack of sub-pixel information for

fires (Eckmann et al., 2010). This can be understood via a simple example in which the FRP_p value is equal for two pixels covering the same area, but containing different burning scenarios: (1) a large fire with burning at a low intensity or (2) a small fire burning at a high intensity. Not surprisingly, a large difference in fire behavior and the thermal buoyancy to drive the rise of smoke plumes can be expected between (1) and (2). However, it will not be discernable in the current MODIS FRP_p product unless sub-pixel information of fire area and temperature is retrieved.

In contrast to the current MODIS FRP_p calculation (equation 1.1), retrieved sub-pixel information (described in Chapter 2) can be used to produce the first direct fire area and temperature-based calculation of MODIS FRP for each sub-pixel fire (FRP_f). Similar to Zhukov et al. (2006), the FRP_f equation (units of Megawatts, above the mean background) uses the Stefan-Boltzmann relationship in the 4 μm channel

$$FRP_f = \sigma(T_f^4 - T_{4b}^4)A_f \tag{1.2}$$

where σ is the Stefan-Boltzmann constant (5.6704×10^{-8} W m^{-2} K^{-4}), T_f is the retrieved kinetic fire temperature at the surface (not the pixel temperature), T_{4b} is the background brightness temperature, and A_f is the retrieved fire area. At cool 4 μm brightness temperatures, atmospheric effects, especially from water vapor content, are minor, which allows T_{4b} to be used as an approximation of surface kinetic background temperature (Kaufman et al., 1998a, also explored in Chapter 4). While each FRP method is different for the same fire, the FRP_f (fire area and temperature-based FRP), in theory, should be strongly correlated to the pixel-based FRP_p value. This assumption can be used because at 4 μm, the radiative power from flaming usually overwhelms that from smoldering within any MODIS pixel (Kaufman et al., 1998a). However, an exact match is not likely

because FRP_p (equation 1.1) is based on a best-fit curve from theoretic simulations of many sub-pixel fire scenarios, including variations in fire temperature, fire area, and smoldering or flaming regions (Figure 1.2). FRP_p also disregards the atmospheric attenuation of infrared radiation, and hence may contain relatively large uncertainties for individual fire events (Kaufman et al., 1998a).

1.1.2 Satellite Observations of Fire Activity and Meteorology

In addition to the estimation of smoke plume injection heights, satellite fire data can be used, in combination with meteorological data, for the analysis and prediction of changes in fire activity. For example, Peterson et al. (2010) incorporated the number and location of MODIS fire pixels (also known as fire counts) to quantify the impact of the synoptic pattern and convective instability on dry lightning strikes and fire ignition. Similarly, Peterson et al. (2012b) attempted to link day-to-day changes in MODIS fire counts to variations in several meteorological variables in the North American boreal forest during the large fire seasons of 2004 and 2005. This analysis resulted in the development of a fire prediction tool that will forecast the growth, decay, or persistence of a given fire event (see Appendix). It was also shown that the fire prediction model is an improvement over the forecast of persistence currently used in several smoke emissions inventories (e.g. Reid et al., 2009), but high levels of noise in the observed number of satellite fire pixels (or fire counts) limited the prediction skill. FRP_p data were not used due to the limitations described in the previous section. Therefore, the incorporation of sub-pixel-based FRP_f data may be very useful for fire weather analysis and prediction, especially when forecasting changes in fire intensity for ongoing events. In addition, an improved understanding of the mechanisms that produce large and intense

(high FRP_f) fire events is directly related to improved estimates of smoke emissions, potentially improving smoke transport forecasts.

1.2 Specific Objectives

This dissertation is based on a sub-pixel retrieval of fire area and temperature that is used to calculate FRP_f (via equation 1.2) for fire pixels detected by the MODIS fire detection algorithm (Collection 5). The following are key objectives:

1) Drawing from previous studies, develop a sub-pixel retrieval of fire area and temperature that accounts for solar and atmospheric effects as a function of Earth-satellite geometry at the MODIS fire detection channels.
2) Assess the retrieved fire area using high resolution (3-50 meters) airborne data collected near-coincident with the MODIS overpass times, and investigate several indirect effects on the retrieval that are difficult to characterize, including the point-spread-function and the distribution of sub-pixel hot spots.
3) Examine the sensitivity of retrieved fire area and FRP_f to potential errors in several direct input variables and assumptions, including the column water vapor amount, background emissivity, and background brightness temperature.
4) Building upon (3), apply an operational version of the sub-pixel algorithm to an independent, large wildfire event to examine the overall performance, limitations, and utility of the retrieval.
5) Identify relationships between retrieved FRP_f and smoke plume heights, as well as relevant fire weather variables and indices obtained from numerical weather

prediction. Use this information to explore potential fire weather and smoke forecasting applications.

1.3 Organization of this Dissertation

In general, the structure of this dissertation follows the key objectives identified in the previous section. Chapter 2 describes the history of sub-pixel retrieval methodologies, the potential sources of error, and the specifics of a modified sub-pixel retrieval methodology for MODIS. The initial assessment of the sub-pixel retrieval, including a description of the impacts originating from several sources of indirect error, is provided in Chapter 3. Chapter 4 is devoted to a sensitivity analysis based on several direct input variables and assumptions. Chapter 5 describes the application of an operational version of the algorithm to a recent case study, and Chapter 6 explores potential applications in the context of smoke plume heights and fire weather. The last chapter is dedicated to conclusions and suggestions of future work. The Appendix describes a short-term predictor of satellite fire activity that is currently based on MODIS fire counts, but can be modified to incorporate the additional fire size and intensity information provided by the sub-pixel retrieval (described in Chapters 2-7).

Chapter 2. Sub-Pixel Algorithm Development

2.1 Introduction

Prior to the calculation of FRP_f the sub-pixel fire area and temperature must be retrieved, which is commonly accomplished via a bi-spectral approach (Dozier, 1981; Matson and Dozier, 1981; Flannigan and Vonder Haar, 1986; Prins and Menzel, 1992; Langaas, 1993; Peterson et al., 2012a) or a multispectral approach (Dennison et al., 2006; Eckmann et al., 2008, 2009, 2010). Regardless of the methodology, a variety of potential error sources, such as improper background temperature selection and band-to-band coregistration issues, may impact the retrieved fire area and temperature (e.g. Giglio and Kendall, 2001; Shephard and Kennelly, 2003; Giglio and Justice, 2003). As a result of these limitations, sub-pixel retrievals have been used sparingly over the past three decades, aside from those developed by Prins and Menzel (1992, 1994) for the Geostationary Operational Environmental Satellite (GOES). However, the coarser resolution provided by the geostationary satellite sensor reduces the sensitivity to wildfires, making it difficult to use FRP_f from GOES quantitatively.

With many potential challenges to overcome in the development of a sub-pixel retrieval, this chapter focuses primarily on: (1) developing an algorithm to retrieve sub-pixel fire information for MODIS with atmospheric and daytime solar effects taken into consideration and (2) calculating the sub-pixel-based FRP using this retrieved information. Subsequent sections of this chapter describe the history of previous sub-pixel retrievals, as well as the potential sources of error that must be considered in the unique methodology of the MODIS sub-pixel retrieval.

2.2 Background: Sub-Pixel Retrievals of Fire Area and Temperature

Dozier (1981) made the first attempt to derive a sub-pixel fire (target) retrieval using a bi-spectral approach. This "Dozier" method uses the spectral contrast between a sub-pixel hot target and the surrounding (presumably uniform) background of the pixel for the 3.8 μm middle infrared (MIR) and 10.8 μm thermal infrared (TIR) channels. Although originally developed for the AVHRR, the Dozier method, in principle, can be applied to any sensor having similar MIR and TIR channels. Using MODIS fire detection as an example, the calculation is performed for each wavelength used in fire detection (~4 and 11 μm) providing two equations that can be solved for the fire temperature (T_f) and the fractional area of the pixel covered by the fire (P), where $0 < P < 1$, located within a uniform background at temperature T_b (surface kinetic temperature). The observed radiances at 4 and 11 μm (top-of-atmosphere), denoted by L_4 and L_{11}, respectively, are

$$L_4 = PB(\lambda_4, T_f) + (1-P)B(\lambda_4, T_b) \tag{2.1}$$

$$L_{11} = PB(\lambda_{11}, T_f) + (1-P)B(\lambda_{11}, T_b) \tag{2.2}$$

where $B(\lambda,T)$ is the Planck function and T_b is estimated from a temperature dataset. The fire (hot target) and background are assumed to be blackbodies with unit emissivity in both channels (Giglio and Kendall, 2001). In addition, all atmospheric effects are neglected, allowing the computation of $B(\lambda,T)$ to be considered a top-of-atmosphere value. With these assumptions, the surface kinetic temperatures, T_f and T_b, can be

considered as brightness temperatures and can be used for both channels; otherwise equations (2.1) and (2.2) are not valid.

Due to the small size of sub-pixel fires and the lack of high spatial and high thermal resolution data, the original Dozier retrieval is difficult to validate. Nevertheless, it was applied to several satellite sensors in the 1980s and 1990s (e.g. Matson and Dozier, 1981; Flannigan and Vonder Haar, 1986; Prins and Menzel, 1992; Langaas, 1993). For example, Matson and Dozier (1981) found an absolute area of 847 m^2 (fraction of ~0.0007 for a 1.1 km pixel) for a gas flare in the Persian Gulf. Prins and Menzel (1992) found fire absolute area values as large as $5x10^6$ m^2, which corresponds to a fraction of 0.1 for a 7 km pixel from GOES VAS observations. When considering all early application studies and their respective pixel resolutions, fire (target) temperatures were found to range from 401 to 790 K. In addition, Langaas (1993) discovered that the retrieved fractional area and fire temperature are extremely sensitive to the selection of T_b. From a validation standpoint, Green (1996) and Riggan et al. (1993) were able to measure fire area fraction and/or temperature using high resolution (~20 meter resolution), airborne instruments in Brazil. However, detailed comparisons with Dozier retrievals from lower resolution satellite data were not undertaken. A more extensive review of the Dozier method and its applications from 1981 to 200l can be found in Giglio and Kendall (2001). The following sections highlight the modifications to the Dozier method over the last decade with a focus on the uncertainty analysis and challenges for validation. This is subsequently followed by the description of the sub-pixel methodology unique to this study.

2.2.1 Previous Modifications of Sub-Pixel Retrievals

Not surprisingly, the assumptions used in the original Dozier retrieval can be unrealistic. For example, atmospheric effects, such as water vapor content, undoubtedly have a major impact on the retrieval, and the fire and background are not perfect blackbodies. Therefore, to create a more realistic retrieval, several studies modified the retrieval by adding relevant terms to the equations (e.g. Prins and Menzel, 1992; Giglio and Kendall, 2001). With these modifications, the observed radiances at 4 and 11 μm, respectively, are

$$L_4 = \tau_4 \left[PB(\lambda_4, T_f) + e_{4b}(1-P)B(\lambda_4, T_b) + (1-P)(1-e_{4b})I_{4ref} \right] \quad (2.3)$$

$$L_{11} = \tau_{11} \left[PB(\lambda_{11}, T_f) + e_{11b}(1-P)B(\lambda_{11}, T_b) \right] \quad (2.4)$$

where e_{4b} and e_{11b} respectively denote the background emissivity at 4 and 11 μm, I_{4ref} is the reflected solar radiance in the 4 μm channel at the surface (equal to zero at night), and τ_4 and τ_{11} are the upward MIR atmospheric transmittance and the upward TIR atmospheric transmittance, respectively. The relationships in equations (2.3) and (2.4) contain several unknowns, and therefore require the aid of a radiative transfer model for closure. The emissivity of the fire is commonly assumed to be equal to one (e.g. Giglio and Kendall, 2001), which has been shown to be a reasonable assumption for most fire events with thick fire fronts. As a result, equations (2.3) and (2.4) do not include emissivity in the fire term.

By assuming identical surface and atmospheric conditions, the MODIS fire product estimates background brightness temperatures (or radiances at the top-of-atmosphere) for the 4 and 11 μm channels by averaging several neighboring, fire-free

pixels (Justice et al., 2002; Giglio et al., 2003). These background radiances, denoted by L_{4b} and L_{11b}, can be expressed respectively, as

$$L_{4b} = \tau_4 \left[e_{4b} B(\lambda_4, T_b) + (1 - e_{4b}) I_{4ref} \right] \tag{2.5}$$

$$L_{11b} = \tau_{11} e_{11b} B(\lambda_{11}, T_b). \tag{2.6}$$

Substituting equations (2.5) and (2.6) into (2.3) and (2.4) produces

$$L_4 = \tau_4 P B(\lambda_4, T_f) + (1 - P) L_{4b} \tag{2.7}$$

$$L_{11} = \tau_{11} P B(\lambda_{11}, T_f) + (1 - P) L_{11b} \tag{2.8}$$

where P and T_f are the only unknown variables. Therefore, fire fraction and fire temperature can be retrieved simultaneously from a combined use of the MODIS-observed background and fire pixel radiances.

2.2.2 Sources of Error, Limitations, and Recent Improvements

Even with improved calculations, two distinct hindrances to the Dozier retrieval have become obvious: (1) the validation difficulty and (2) the potential sources for error in the retrieval. For proper validation, the sensor providing the 'ground truth' must do so at a relatively fine spatial resolution and the observation time must be very close to that of the satellite sensor under scrutiny. Unfortunately, such measurements are typically not available in sufficient quantities to accomplish a significantly representative validation. While the validation issues are relatively straight forward, understanding the potential for error is much more complex. Sources of error may include band-to-band coregistration issues, improper selection of background temperature and atmospheric transmittance, instrument noise, varying sub-pixel proportions of flaming, smoldering, and unburned areas, the solar contribution to the MIR, and the variation of surface emissivity between

MIR and TIR, etc. (e.g. Giglio et al., 1999; Giglio and Kendall, 2001; Shephard and Kennelly, 2003; Giglio and Justice, 2003).

Due to the small size of the fire in comparison to the pixel, the potential impact from the 4 and 11 μm point-spread-functions (PSFs), including their coregistration, becomes a critical source of error for a bi-spectral retrieval, regardless of satellite sensor. For example, the MODIS PSF displayed in Figure 2.1 shows that the fire pixel brightness temperature, for a given sub-pixel fire size and temperature, will greatly decrease when the sub-pixel fire is located near the edge of the pixel, and increase for fires near the pixel center (Calle et al., 2009; Schroeder et al., 2010). Additionally, the 4 and 11 μm PSFs may deviate near the pixel edge (misregistration), thereby increasing the potential error in retrieved fire area and temperature in these cases.

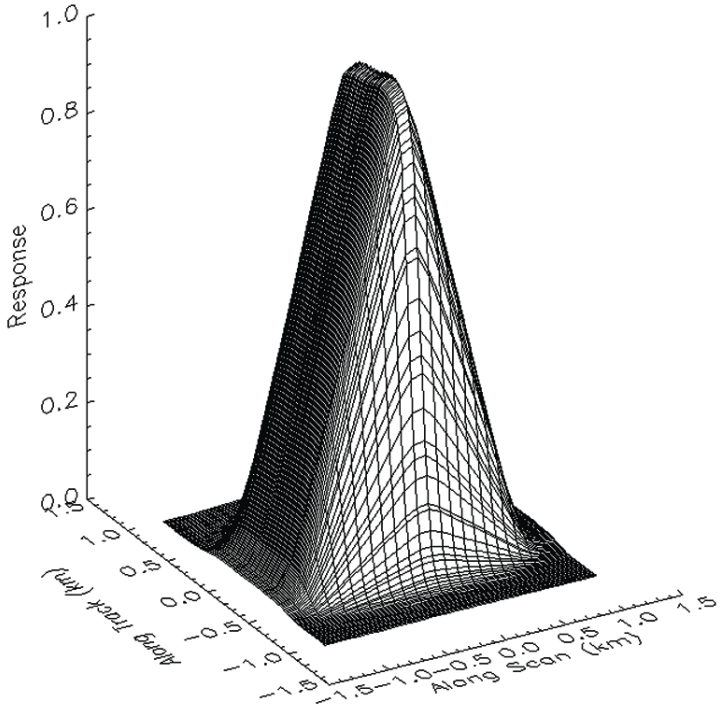

Figure 2.1: Three-dimensional representation of the 4 μm point spread function for MODIS (adapted from Schroeder et al., 2010).

Daytime solar reflection in the MIR channel can also have an impact on sub-pixel retrievals. Specifically, Li et al. (2001) showed that the contribution of reflected solar radiation in the AVHRR MIR channel increases as the surface temperature decreases. The solar contribution was also found to be highly dependent on the solar geometry and surface albedo. When considering the potential error sources (aside from coregistration), Giglio and Kendall (2001) found that the Dozier retrieval is possible when the fraction of the pixel encompassed by fire is greater than ~0.005 (0.003 for MODIS). Above this threshold, random retrieval errors will be within 50% and 100 K, at one standard deviation, for fire fractional area and temperature, respectively. However, uncertainties increase rapidly below the threshold.

Despite the potential for error, several advances have been made to sub-pixel retrievals over the past decade. One example is the Bi-Spectral Infrared Detection (BIRD) small satellite mission (operational from 2001-2004). The BIRD satellite had a pixel size of 185 meters, saturation temperature of ~600 K, and MIR and TIR channels of 3.8 and 8.8 μm, respectively (Zhukov et al., 2006). In contrast to MODIS, the BIRD fire detection algorithm specifically included a component for a modified Dozier retrieval. To avoid the potential error sources, especially coregistration errors, the BIRD algorithm created pixel clusters using any adjacent hotspot pixels (Zhukov et al., 2005, 2006; Wooster et al., 2003). The modified Dozier retrieval was then performed on these clusters rather than individual pixels. Ground validation tests for controlled fires were performed (e.g. Oertel et al., 2004; Zhukov et al., 2005), but detailed assessments of wildfires, using higher resolution sensors, were not undertaken.

In recent years, a modified approach, using multiple endmember spectral mixture analysis (MESMA) to retrieve sub-pixel fire properties, has been developed (Dennison et al., 2006; Eckmann et al., 2008, 2009, 2010). MESMA assumes the radiative signature of each pixel is a result of a linear combination of sub-pixel features (or endmembers), and thus the radiances at multiple channels can be used to disentangle the area fraction of each end-member (such as fire and non-fire) provided that the number of channels is larger than the number of sub-pixel features to be retrieved. The original method was used for classification of land surface type. In that case, a finite number of endmembers, each having unique land surface characteristics, were incorporated into the analysis. However, the application to wildfires is not straightforward because the number of fire classes can be infinite. Nevertheless, Eckmann et al., (2008, 2009, 2010) produced fire endmembers for a variety of temperatures over a variety of wavelengths. Therefore, the MESMA retrieval is essentially a Dozier retrieval over a variety of wavelengths instead of two channels. Results from the MESMA and Dozier-type retrievals have been compared, but neither retrieval method could be shown to be superior with the available validation data (Eckmann et al., 2009).

2.3 Developing a Sub-Pixel Retrieval for MODIS

Since MODIS data became available from Terra in February of 2000, few attempts have been made to implement a MODIS sub-pixel retrieval, which is likely a result of the large potential for error, especially from atmospheric effects (Giglio and Kendall, 2001). In this study, output from the Santa Barbara DISORT Atmospheric

Radiative Transfer (SBDART) model is uniquely incorporated to provide a representation of atmospheric effects prior to the calculation step, which avoids creating additional terms for atmospheric transmittance (as in equations 2.3 and 2.4). Specifically, SBDART considers many processes known to affect the ultraviolet through the infrared wavelengths allowing for detailed computations of plane-parallel radiative transfer within the Earth's atmosphere and at the surface (Ricchiazzi et al., 1998). Therefore, SBDART also includes the solar reflectivity term (I_{4ref}) in equations (2.3) and (2.4). Based on previous studies, e_{4b} and e_{11b} are assumed to be respectively equal to 0.95 and 0.97 (e.g. Giglio et al., 1999; Petitcolin and Vermote; 2002; Tang et al., 2009), which is true for relatively dense, green vegetation, such as the temperate evergreen forests used in this study. With this configuration and by including the MODIS spectral response function, SBDART is ready to incorporate all terms in equations (2.3) and (2.4) to simulate the MODIS observation at its two fire detection channels (3.96 and 11.0 μm).

2.3.1 Lookup Tables

As a preliminary step, SBDART is run repeatedly for different combinations of the possible geometry values, background temperatures, and sub-pixel fire temperatures, and the output results are saved together with the input parameters as a lookup table at 4 and 11 μm. The input temperature values are the kinetic temperatures (not brightness temperatures) at the bottom of the atmosphere and range from the lower limits for a background temperature (277 K) to the upper limit for a sub-pixel fire (1500 K). Based on the analysis in subsequent chapters, the atmospheric profile is assumed to be a representative mid-latitude summer profile, which includes 2.9 g/cm^2 of water vapor in

the atmospheric column. However, the sensitivity to variations in the atmospheric profile is examined in Chapter 4.

Additional key entries in the lookup tables include various sets of L_{4b} and L_{11b}, which can be used in place of T_b, e_{4b} and e_{11b} (equations 2.5 and 2.6) because the MODIS fire detection algorithm, under the assumption of identical surface and atmospheric conditions, provides an estimate of the top-of-atmosphere (TOA) brightness temperature for the surrounding fire-free (background) pixels that can be used to directly compute L_{4b} and L_{11b} (Giglio et al., 2003; Giglio, 2010). Therefore, for any given MODIS fire pixel, T_f and P can be extracted from the lookup tables by matching the viewing geometries, incorporating L_{4b} and L_{11b} as entries, and using L_4 and L_{11} as constraints. While the MODIS fire product provides an estimate of L_{4b} and L_{11b}, the simulation of TOA radiance in the lookup tables requires the consideration of emissivity and atmospheric effects (e.g. τ_4 and τ_{11}) to ensure physical consistence in equations (2.3) - (2.6). As a result, the retrieval may be sensitive to these parameters (see Chapter 4).

The final SBDART output allows a lookup table, containing input surface temperature, solar zenith (SZA), viewing zenith (VZA), and relative azimuth (RAZ) angles, to be created as a function of TOA radiance. An example is displayed in Figure 2.2, corresponding to the sub-pixel retrieval's lookup table for a single fire pixel when the VZA = 14^o, SZA = 48^o, and RAZ = 165^o. Each dashed curve represents the pixel temperatures at 4 and 11 μm that result from specified values of fire area fraction for varying fire temperatures. Each solid curve, on the other hand, represents the pixel temperatures that result from specified values of fire temperature for varying fire area fractions. These lookup tables are referenced repeatedly in the main retrieval process.

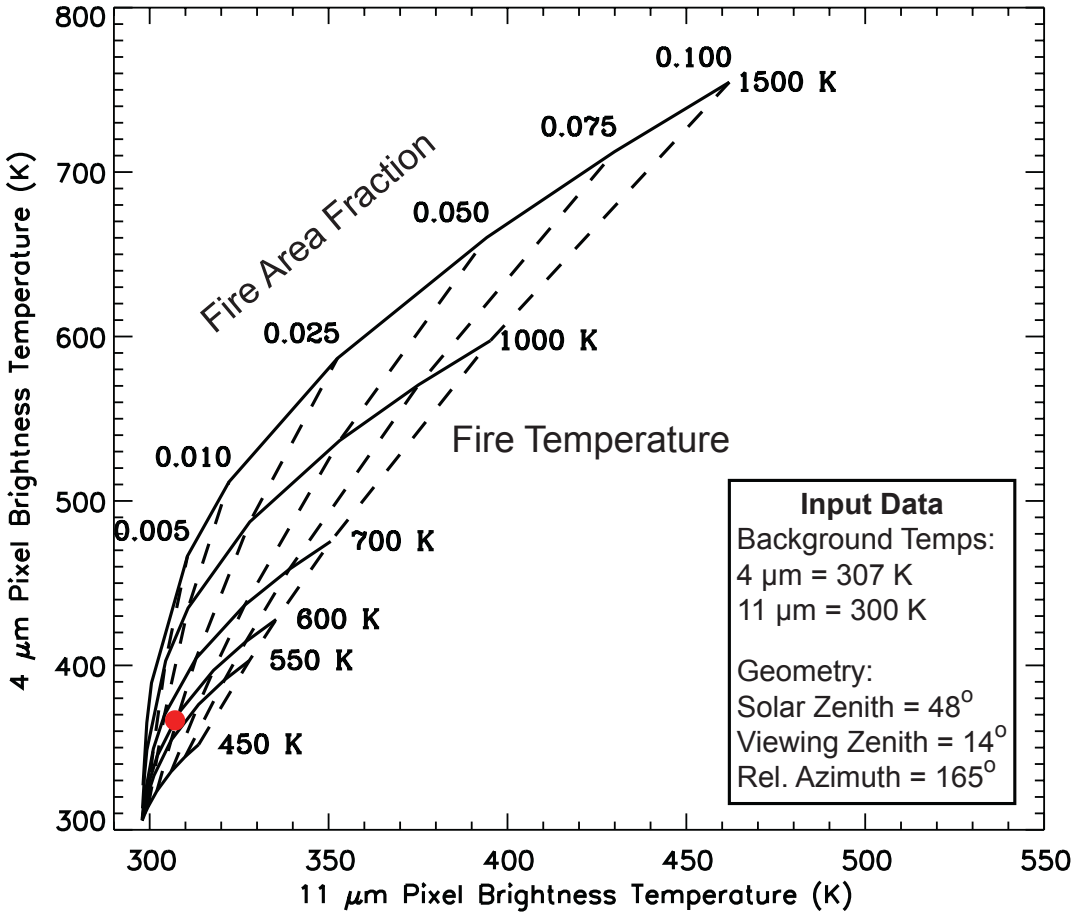

Figure 2.2: Visualization of a lookup table for the input data shown in the black box. Each dashed curve represents the relationship between the 4 and 11 μm pixel brightness temperatures at specified values of fire area fraction for varying fire temperatures. Each solid curve represents the relationship between the 4 and 11 μm pixel brightness temperatures at specified values of fire temperature for varying fire area fractions. The superimposed red dot indicates a MODIS fire pixel corresponding to the input data.

2.3.2 Retrieval Methodology

The actual retrieval, which is summarized in Figure 2.3, implements the lookup tables to aid in solving equations (2.3) and (2.4) for each MODIS fire pixel in any given MODIS scene (granule). However, the non-linear equations require the use of a multistep, iterative process to obtain fire area fraction and temperature. To begin, the

observed MODIS geometries and the first input temperature are matched to the lookup table to obtain the top-of-atmosphere radiance of the pixel containing the fire. The algorithm then continues to cycle through all input temperatures (e.g. potential fire temperatures) and calculates the fire fraction using a variation of the method developed by Shephard and Kennelly (2003). A residual calculation is used to keep track of the fire temperature and area fraction corresponding to the best fit in the observed radiances for the 4 and 11 μm channels and the final fire temperature and area fraction are selected based on the lowest residual.

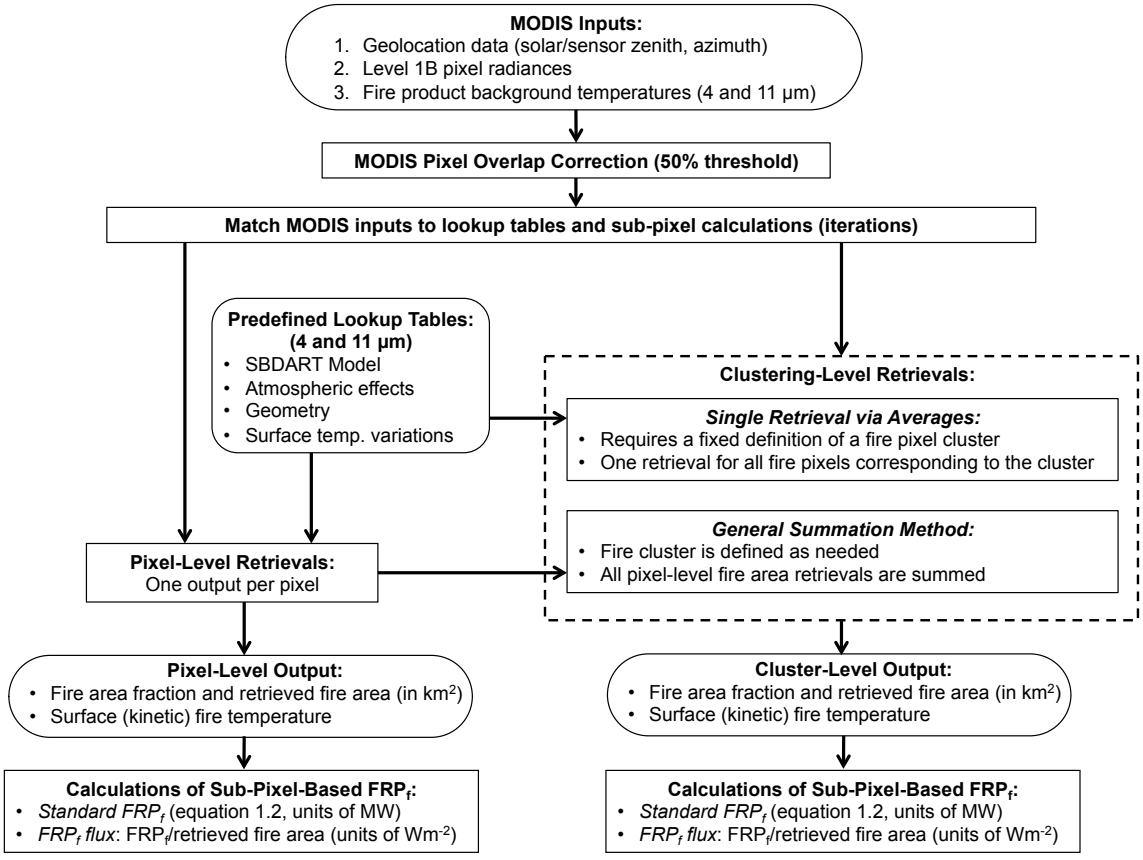

Figure 2.3: Flowchart illustrating the MODIS sub-pixel retrieval and the subsequent calculation of FRP_f.

Drawing from the BIRD satellite methodology, two clustering methods are implemented to alleviate random errors within the pixel-level retrievals. The first is a general summation method, where each individual pixel-level retrieved fire area is summed to obtain the area of an entire fire event. The second clustering method is a single retrieval (via averaging), which performs a single retrieval for all MODIS fire pixels corresponding to a given fire cluster. In this case, the sub-pixel calculations use the mean geometry values, mean pixel temperatures, and mean background temperatures of the fire pixel cluster. Overlapping MODIS pixels are removed a priori to reduce the change of artificially large fire clusters, especially for the general summation method (see Chapter 3). Following these pixel and cluster-level calculations, FRP_f is calculated via equation (1.2). Therefore, there are three major outputs from the retrieval at both the pixel and cluster-levels: fire area, fire temperature, and FRP_f. As mentioned in Section 2.2.2, specific sources of error can stem from indirect effects (e.g. PSF coregistration) to the direct inputs and assumptions of background temperature, surface emissivity, and water vapor, etc. Chapter 3 examines the uncertainties from indirect error sources, while a detailed examination of sensitivity to direct error sources is described in Chapter 4.

2.4 Summary

In an effort to provide a fire area and temperature-based FRP product, this chapter has developed the first MODIS sub-pixel retrieval algorithm for fire area and temperature, which are used to calculate FRP_f. The retrieval was designed such that it can be run on any MODIS granule across the globe, and a radiative transfer model was

used to account for atmospheric effects and variations in Earth-satellite geometry. Using a lookup table approach, the retrieval can be run at both the pixel and cluster levels and corrections are made for overlapping pixels. Currently, fire pixel locations as well as the 4 and 11 μm background temperatures are direct inputs from the MODIS fire product (Collection 5). However, the MODIS sub-pixel-retrieval can easily be applied to the next generation of satellite sensors, such as the Visible Infrared Imaging Radiometer Suite (VIIRS) on board the recently launched Suomi NPP satellite (Csiszar et al., 2011) and the Geostationary Operational Environmental Satellite – R Series (Schmidt et al., 2011, GOES-R, http://www.goes-r.gov), which will be described in Chapter 7.

Chapter 3. Initial Assessment of Retrieved Fire Area and FRP_f

3.1 Introduction

Validations of sub-pixel retrievals are difficult due to the need for high-resolution data that are coincident in time and space with observation of the satellite sensor (e.g. Dozier, 1981). Fortunately, multispectral, high-resolution data (3-50 meters), obtained from the airborne Autonomous Modular Sensor (AMS) are now available for numerous fire events in the western United States (e.g. Ambrosia and Wegener, 2009). In many cases, the AMS flight scan can be spatiotemporally collocated with MODIS scenes (Figure 3.1), allowing for an unprecedented representation of the flaming, smoldering, and background regions within a given MODIS fire pixel. By using the collocated data, a quantitative assessment of a MODIS sub-pixel retrieval of fire information can be conducted for multiple fire events in various biomes. The AMS data can also be used to validate background temperatures and to isolate the various sources of error known to affect sub-pixel retrievals. This chapter is partially devoted to developing an AMS-derived fire (hot spot) detection algorithm that is used to assess the accuracy of the retrieved sub-pixel fire area from MODIS. The remainder of the chapter focuses on the comparison of MODIS retrieved fire area with AMS observations and comparisons between the MODIS FRP_p and sub-pixel-based FRP_f for several fire events occurring between August and October 2007 (Figure 3.1).

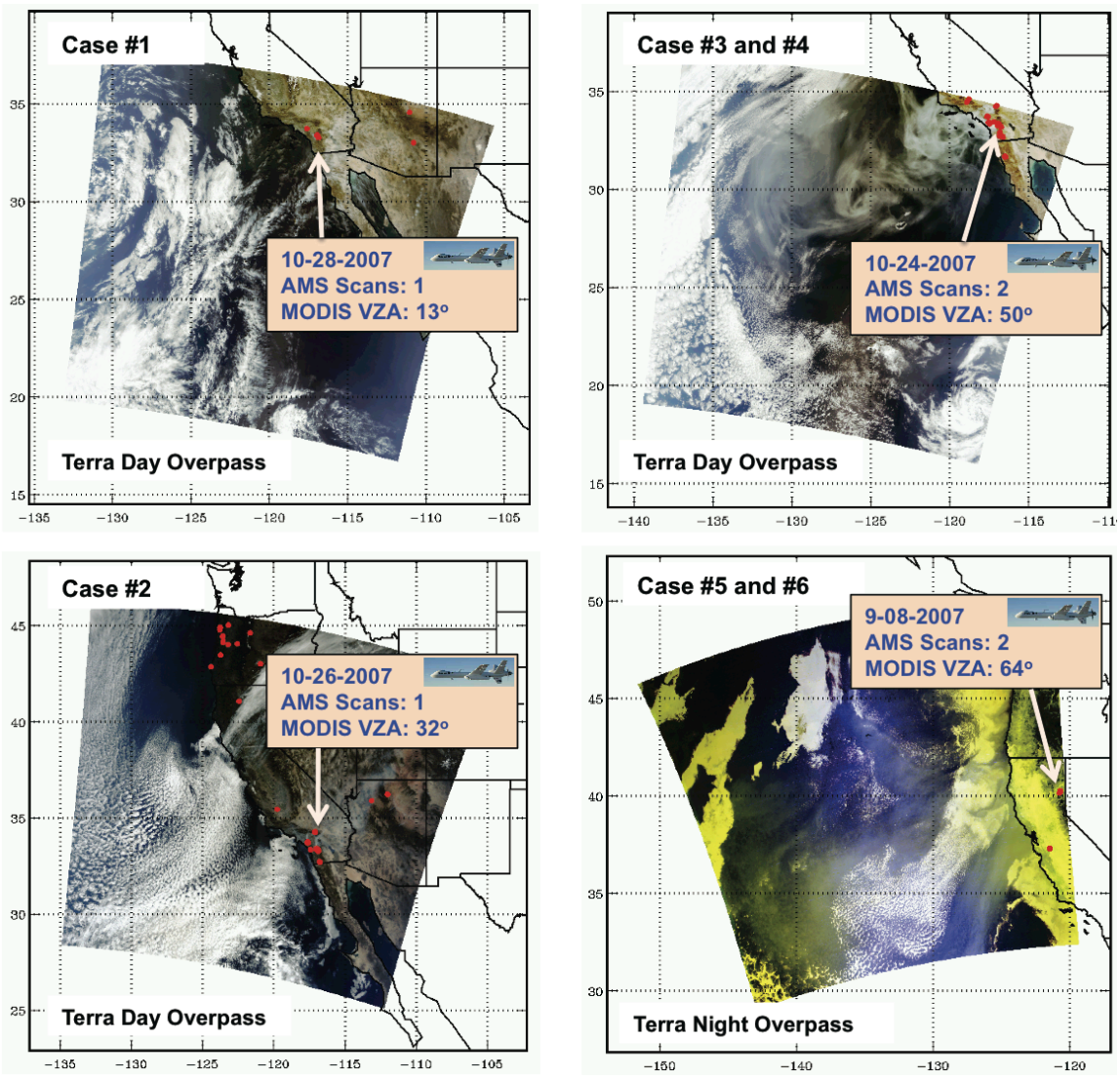

Figure 3.1: Projections of the four MODIS scenes that contain the six AMS flight scans (details provided in Table 3.1). Red dots denote the locations of MODIS fire pixels (not to scale) and arrows highlight the fire pixels that are collocated with at least one AMS scan. While two collocations may come from the same MODIS scene, steps are taken to minimize overlap.

3.2 Data Sources: MODIS and the Airborne AMS

MODIS sub-pixel fire information is retrieved from an integrated use of the following three data products, either from MODIS/Terra or MODIS/Aqua, at a spatial resolution of 1 km^2 at nadir: (1) level 1B radiance data (MOD021KM/MYD021KM), (2)

geolocation data (MOD03/MYD03), and (3) level 2 fire product data (MOD14/MYD14). Data sources (1) and (2) are used to provide the radiance of the entire pixel and all relevant geometry information, such as the SZA, RAZ, and VZA (e.g. Wolfe et al., 2002), while the fire product (3) provides information on fire locations, background temperature, and FRP_p. The sub-pixel retrieval is only applied to the pixels that are flagged as fire pixels by the standard MODIS fire product (3). MODIS algorithms (including the fire algorithm) are periodically updated, producing different versions, which are used to generate a series of collections of the data products. This study uses Collection 5 for data sources (1) – (3), which can be found at http://ladsweb.nascom.nasa.gov/data/search.html (obtained in June 2010).

3.2.1 MODIS Fire Products: Fire Detection and FRP_p

MODIS is unparalleled in fire detection because of its ability to differentiate a wide range of fire intensities, as a result of the synergy between its two 4 μm (more precisely 3.96 μm) channels whose dynamic ranges are complementary (Justice et al., 2002). In the standard MODIS fire detection algorithm, fire pixels are retrieved using a hybrid, contextual process, which includes absolute and relative detection pathways. For absolute detection, a set of thresholds for reflectance at 0.86 μm and brightness temperature at the 4 μm and 11 μm infrared channels are used. The reflectance values of the 0.86 um channel are employed to reduce the "false-positive" effects of bright reflective surfaces and sun glint characteristics in a given scene that contains a mix of fire and those non-fire, highly reflective surface features. The brightness temperature thresholds at the 4 μm and 11 μm infrared channels are used to identify potential fire

pixels (Justice et al., 2002; Giglio et al., 2003). The relative detection check is then incorporated to compare a pixel's spectral signature to surrounding background pixels. Finally, both checks are combined (as a Boolean union) to classify a potential pixel as a real fire pixel. The MODIS FRP_p (Collection 5) is subsequently calculated for all fire pixels via equation (1.1). The higher saturation temperatures of MODIS allow for the derivation of FRP_p for nearly every fire it detects, because 1 km^2 pixels with $T_4 > 500$ K seldom occur in nature (Ichoku et al., 2008a).

The major sources of uncertainty in the current MODIS fire products are sun glint, coastal false alarms (water reflectance), and dense cloud cover, all of which may affect the accuracy of fire detections. However, these potential impacts are usually identified a priori by applying water masks and cloud masks within the fire detection algorithm (Kaufman et al., 1998a; Giglio et al., 2003). Using 30 m validation data (from ASTER and ETM+), Schroeder et al. (2008) show that the probability of detection approaches 80% when the number of 30 m fire pixels (contained within a MODIS fire pixel) approaches 75. The smallest detectable fire size in any given MODIS fire pixel was found to be ~100 m^2 (Giglio et al., 2003). Though hard to validate directly and globally, MODIS FRP_p was found to be in fair agreement with FRP_p measurements by other sensors in several sub-global spatial domains (Wooster et al., 2003; Roberts et al., 2005; Ichoku et al., 2008a). The FRP_p detection limits are about 9 and 11 MW for Terra and Aqua, respectively (Schroeder et al., 2010).

3.2.2 Autonomous Modular Sensor (AMS) Observations

The AMS, flown aboard the NASA Ikhana Unmanned Airborne System (UAS) and additional piloted aircraft, provide the high-resolution data for the initial assessment

of the MODIS sub-pixel retrieval. The AMS was put into operations in 2005 and offers pertinent spectral measurement capabilities, such as derivation of fire size, temperature, and serves as a potential airborne, higher spatial resolution FRP validation sensor. Both NASA and the United States Forest Service (USFS) have collaborated on the use of the AMS for supporting wildfire observations. The Ikhana UAS performance characteristics allow mission profiles that can extend from the Mexican border in the south to the Canadian border in the north and from the Pacific Ocean in the west to the Rocky Mountains in the east when operating out of it's home base at NASA-Dryden Flight Research Center, Edwards, California (Ambrosia et al., 2011b; Ambrosia and Wegener, 2009). In addition, the Ikhana is capable of supporting day and night operations with a ~24 hour endurance, 150-200 knots airspeed, ~13720 meters (45,000 ft) altitude, and flight legs of over 7408 km (4000 nautical miles). A pilot located at a ground control station remotely controls the Ikhana. Piloted operations on various aircraft (Beechcraft B200 King-Air, etc) have also been accomplished, though with shorter flight profile capabilities.

The AMS spatial resolution is controlled by the platform altitude and commonly falls in a range from 3 to 50 meters. The total field of view (FOV) can be set at 43^{o} or 86^{o}, and the instantaneous field of view (IFOV) can be set at 1.25 milliradians (mrad) or 2.5 mrad (Ambrosia and Wegener, 2009). Both the FOV and IFOV are user selectable based on the mission requirements. For example, an altitude of 7011 meters (23,000 ft) Above Ground Level (AGL), with a 2.5 mrad IFOV would provide a spatial resolution of 15 meters (Ambrosia and Wegener, 2009). The AMS is a multispectral instrument with 12 spectral channels in the visible through thermal-infrared (Ambrosia et al., 2011a,

2011b). Fire hot spots are detected near 4 and 11 μm using AMS channel 11 (3.75 μm) and channel 12 (10.76 μm) (Ambrosia et al., 2011b; Ambrosia and Wegener, 2009). Originally applied to AVHRR imagery (Li et al., 2000a), the AMS fire detection algorithm is based on that developed by the Canadian Center for Remote Sensing (CCRS) and provides general hot spot information for each AMS scan (Li et al., 2000a, 2000b, 2001; Flasse and Ceccato, 1996; Cahoon et al., 1992).

In this chapter, a separate AMS fire detection algorithm, developed specifically for an initial assessment, is used to identify the individual flaming regions within a given MODIS fire pixel (see Section 3.4). This new algorithm is based on the unique challenges encountered when applying the AMS to obtain the precise area of a sub-pixel fire. For example, changes in flight altitude and surface topography can affect the AMS background temperature and fire detection thresholds within a scan or from scan-to-scan. Therefore, in the initial assessment algorithm, each threshold is image-based and allowed to vary within the boundaries of each MODIS fire pixel. The AMS data collected in 2007 are saturated in the 4 μm channel, with saturation temperatures varying from 510 to 530 K, depending on the flight characteristics. At spatial resolutions of 50 meters or larger, this saturation level means that many fire pixels are saturated, which precludes fire temperature or FRP investigations using these data. Approximations of fire temperature can also be achieved using the unsaturated 11 μm channel, but limitations are introduced due to the lower sensitivity at higher temperatures.

3.2.3 AMS and MODIS Collocation

Several AMS flight data scans, from August - October 2007, were available for this study (obtained in early 2010 from http://asapdata.arc.nasa.gov/ams/missions.html),

which include both single fires and multiple fire events. The high spatial resolution (~15 m) AMS data, collected near-coincident with MODIS acquisitions, allow for a determination of the fire hot spots within the MODIS fire pixels corresponding to a given fire event (Figure 3.2). With a wide range in topography and biomass type (Westerling et al., 2003), the western United States is known to experience a wide variety of burning conditions. These variables affect the fire rate of spread, which can reach 34 meters per minute (~0.5 km per 15 minutes) in the chaparral of Northern California (Stephens et al., 2008), suggesting that some fires may change drastically in a short time period. The large Zaca Fire example in Figure 3.2, has a time lag of approximately an hour between the MODIS overpass and the AMS flight, which explains some fire location dissimilarities between the MODIS and AMS detections. Therefore, to produce an accurate assessment, the temporal difference between AMS and MODIS was limited to a maximum of 15-17 minutes before or after the MODIS overpass, ensuring that MODIS and AMS are observing the same fire characteristics, near-simultaneously.

After applying the temporal limitation, a total of six collocated cases (displayed in Figure 3.1) are available from the 2007 dataset, which include day, night, nadir, and off-nadir MODIS observations. Specifically, four MODIS scenes (granules) are used to provide the six collocations. Of these, cases #1-4 are from a single Santa Ana burning event in Southern California (24-28 October 2007) and cases #5 and #6 are from a fire event in Northern California on 9 September 2007. The Ikhana commonly flies over the same fire event multiple times on adjacent flight tracks, used to derive a "mosaic" of the total fire event region. The AMS on the Ikhana has also been used to capture the same fire event during two (or more) time periods in a day to derive fire progression and some

AMS fire data scans can be as short as 3 minutes. Therefore, by examining neighboring, short duration AMS scans, it is possible for a single MODIS scene to provide more than one collocation (e.g. cases #5 and #6 in Figure 3.1). A spatial investigation is conducted to minimize any overlapping MODIS fire pixels between collocation cases. Even still, three fire pixels overlap between cases #3 and #4 and one fire pixel overlaps cases #5 and #6. The specific details for calculating MODIS pixel dimensions are provided in following section.

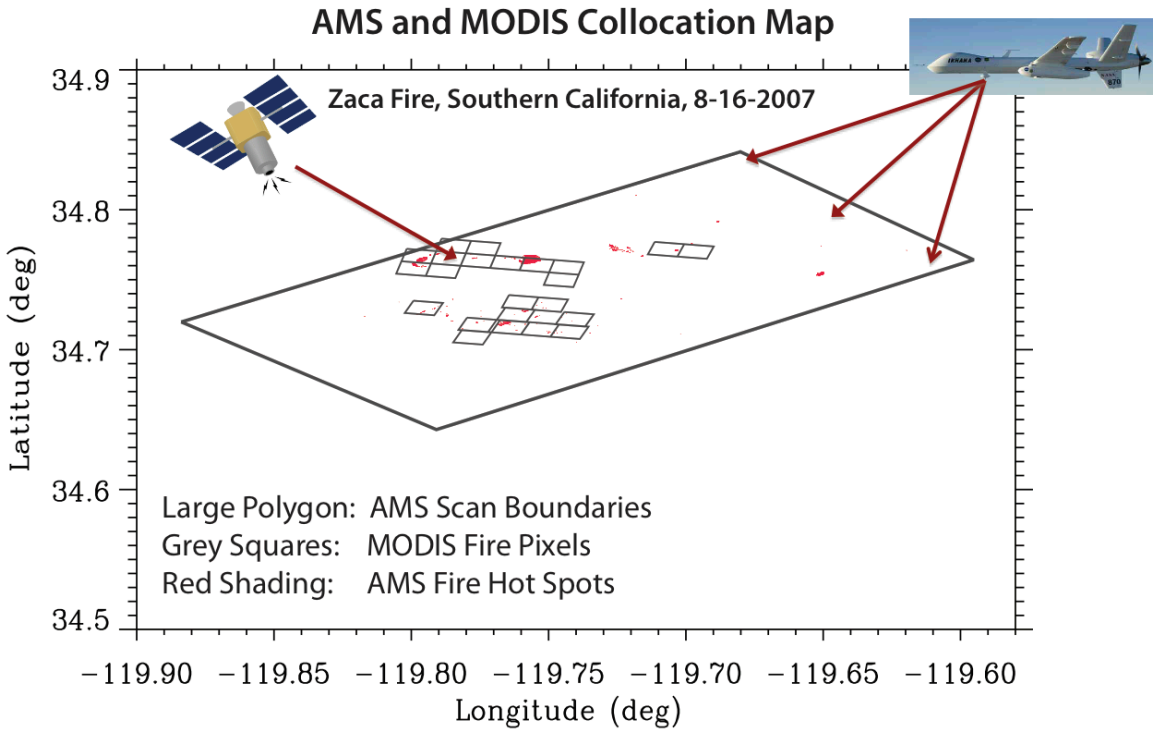

Figure 3.2: Example AMS and MODIS collocation map for the large Zaca Fire in August 2007. There is approximately an hour time lag between the MODIS overpass and the AMS flight.

3.3 Calculating Pixel Area and MODIS Pixel Overlap Correction

Another MODIS characteristic affecting sub-pixel retrieval is the potential for off-nadir fire detection errors (e.g. Giglio and Kendall, 2001). The "bowtie" scanning

method of MODIS results in pixel overlap near the edge of the granule (e.g. Masuoka et al., 1998; Gomez-Landesa et al., 2004), which can result in the same fire being counted in more than one scan, effectively producing duplicated - though not identical - fire pixels. Therefore, to retrieve accurate fire size, any pixel overlap must first be removed (shown in Figure 2.2), especially for the clustering analysis step. To begin, the pixel corners are calculated by averaging the four pixel centroid points (provided by MODIS) surrounding each corner. The pixel corners at the scan edges are then approximated using the dimensions of neighboring pixels. This methodology is different than the MODIS pixel size approximation provided by Giglio (2010), which provides a standardized calculation for every MODIS scene based on the pixel's VZA and recognizes that MODIS pixels realistically have soft, non-rectangular edges. However, this study requires an approximation of the specific boundaries of each pixel to account for any potential variations in pixel size caused by variations in local topography and to facilitate the collocation of the AMS data. As a result, the dimensions of each MODIS pixel are calculated on a scan-by-scan basis. With this information, the area of each MODIS pixel is subsequently calculated, allowing the true area of a fire (in km^2) to be calculated from each retrieved fire fraction (Section 2.3.2). In general, the calculated pixel areas fall within 5-12% of the values obtained via the Giglio (2010) approximation.

The actual overlap correction takes advantage of the similarities within every MODIS granule. For example, every granule contains 204 scans comprised of 10 scan lines along-track (Wolfe et al., 2002), each with an along-scan width of 1354 pixels (one scan = 10 x 1354 pixels or about 10 x 2300 km). While the average pixel size near-nadir is 1 km^2, off-nadir pixel growth causes the total scan width to grow to 2300 km rather

than 1354 km. Based on these similarities, any pixel that overlaps another pixel in one granule will overlap that same pixel in every granule. Therefore, by assuming the Earth is a perfect sphere and topographic influences are minimal, a general overlap correction can be developed and applied to all MODIS granules. For this study, a pixel is defined as an overlapping pixel if it overlaps a pixel in the previous scan by 50% of its total area. This overlap definition is then tested on every pixel on a scan-by-scan basis. For example, the locations and dimensions of each individual pixel within the second scan are compared to the first scan's pixel locations and dimensions. The algorithm keeps track of the locations (index) of any pixels that overlap the first scan and the process repeats for each subsequent scan in the granule. The end result is an index of pixel locations that must be removed from each scan in any MODIS granule.

While pixel overlap may allow for multiple vantage points of the same fire at the individual pixel level, future applications will not necessarily have high resolution data available to discern which of these vantage points is the best, and any overlap will also influence the cluster-level results. Therefore, an overlap correction is used in each collocation case to reduce the chance of artificially large fire clusters, which is especially critical for the general summation clustering method (described in Chapter 2). Even with the overlap correction, small instances of overlap and small gaps may still exist, but the pixel grid will become much more realistic, especially at larger VZAs. As an example, the overlap correction was tested on one of the six collocation cases (case #4) with a mean VZA of 50^{o} (Figure 3.3). Without a correction, this case had a total of 17 MODIS fire pixels and displayed considerable pixel overlap. However, when applying the correction to select only the non-overlapping pixels, the pixel grid clears up and the total

number of fire pixels is reduced to 11, which is a much more realistic value. The specific details for each collocation case are presented in Table 3.1 and show that the overlap correction does little to alter the pixel grid when the VZA is less than ~35^{o} (near-nadir), but the number of fire pixels can decrease by more than 50% at large VZAs after the correction is applied.

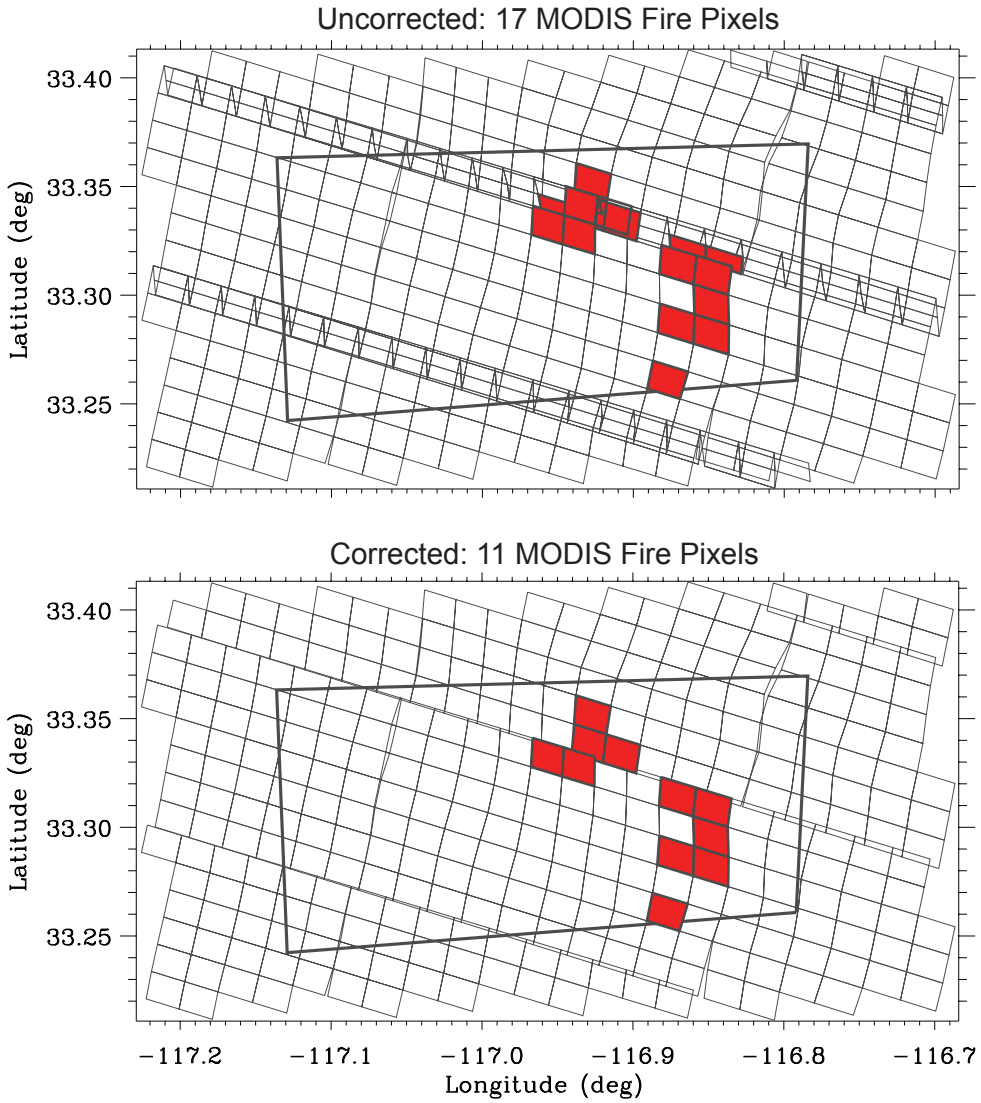

Figure 3.3: An example MODIS and AMS collocation case (case #4) at a MODIS viewing zenith angle of 50.3^{o}. (Top) Without a pixel overlap correction and (Bottom) with a pixel overlap correction. Black polygons denote the boundaries of the AMS scan and the pixels shaded in red are the MODIS fire pixels contained within the AMS scan.

Table 3.1: Specifics of the case studies and results of the pixel overlap correction.

Collocation Case #	Date	Overpass Day/Night	Mean Viewing Zenith Angle	# Fire Pixels Uncorrected	# Fire Pixels Corrected
1	10-28-2007	Day	13	7	7
2	10-26-2007	Day	32	5	5
3	10-24-2007	Day	50	10	9
4	10-24-2007	Day	50	17	11
5	09-08-2007	Night	64	7	3
6	09-08-2007	Night	64	4	2

3.4 AMS Fire Detection Algorithm and Background Temperature

Similar to MODIS, AMS fire detection requires the use of thresholds, which can be somewhat subjective (Kaufman et al., 1998a; Justice et al., 2002; Giglio et al., 2003). Due to the shift in the peak of the Planck Function toward shorter wavelengths at high temperatures, fire detection thresholds are typically based on the 4 μm channel. However, detection algorithms for different sensors, such as MODIS and GOES, utilize the 11 μm channel to varying degrees (Giglio et al., 2003; Prins and Menzel, 1994). For example, MODIS incorporates the temperature difference between 4 and 11 μm and the early GOES algorithm set a specific fire detection threshold for the 11 μm channel. In the case of AMS, an 11 μm fire threshold is used as a secondary check when saturation is reached at 4 μm. Through an automated process, the AMS fire detection thresholds are allowed to vary for each MODIS pixel and adapt to the unique characteristics of the AMS instrument. The AMS algorithm is not meant for operational purposes and is specifically designed to process the AMS data points contained within a single MODIS pixel.

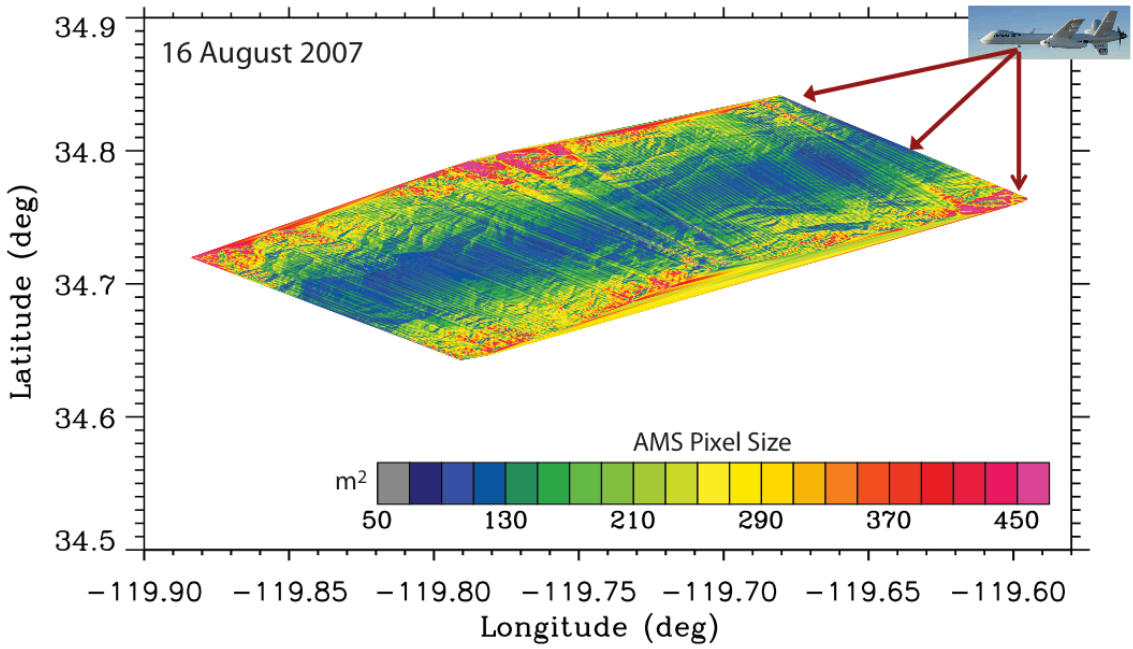

Figure 3.4: Visualization of the variation in AMS pixel size (resolution in m^2) based on the location within the scan and elevation. Cool colors indicate regions of higher resolution and warm colors indicate the coarsest resolution.

Within any MODIS pixel, there are between 4000 and 9000 AMS data points depending on the location relative to the AMS nadir and the flight altitude (Figure 3.4). These data points allow for a detailed investigation of the 'mixed' MODIS fire pixels, which commonly contain a background, smoldering, and actively burning region (e.g. Kaufman et al., 1998a; Eckmann et al., 2008). However, it is assumed that the temperature difference between actively burning and smoldering regions is larger than the difference between background and smoldering. Hence, AMS fire detection is currently aimed at obtaining the mean state of temperature and fire size of two groups: (1) the data points of actively burning fires, and (2) the data points of the remaining region (including smoldering and cooling). The smoldering region is largely neglected because the collocated cases (#1-6) are very intense fire events and the sub-pixel

calculation is likely weighted toward retrieving the flaming region (largest contribution to pixel MIR radiance). Fire modeling studies have shown that the depth of a fire front commonly ranges from a few meters to ~30 meters for grassland fires (Mell et al., 2007) and can reach 400 meters in dense vegetation (Filippi et al., 2009). Based on the potential fire front size, it is expected that the fire area fractions, obtained with the AMS algorithm, will typically fall below ~0.2 for any given MODIS pixel.

3.4.1 Background Temperature and Minimum Thresholds

The AMS fire detection process is based on the histogram at 4 and 11 μm and begins with background temperature selection. In contrast to the neighboring pixel method for MODIS background temperature (Kaufman et al., 1998a), the histogram method for background temperature considers the temperature of the unburned AMS data points within the MODIS fire pixel (in-pixel background temperature). This method is necessary because the AMS flying altitudes vary case by case, and hence any thresholds on temperature should be image based. Due to the scanning method of AMS, topographic effects, and aspect, the cool region of the pixel can vary 5-10 K (Figure 3.5). However, this variation is not likely over a 1 km distance unless there is a rapid change in elevation. Therefore, to account for any of these observational differences, the AMS background temperature calculation at 4 and 11 μm (dash-dotted blue lines in Figure 3.5c,d) is a weighted average of all temperature bins (in the histogram) less than the median. A visual inspection of each histogram is also undertaken to be certain that the calculated AMS background temperatures are representative of only the non-burning portion of the pixel. The AMS background temperature can then be compared to the MODIS background temperature (green dashed lines in Figure 3.5c,d).

Following the background calculations, any AMS data points that are obviously not fire hot spots (blue dots in Figure 3.5b) are removed using an interchannel comparison test (ICT), which searches for any AMS data points that are cooler than the background temperature or display cold 11 μm temperatures at high 4 μm temperatures. The ICT is necessary because of variability in the AMS data from scan to scan that results from varying saturation levels, flight altitudes, and scan widths. Specifically, the ICT calculation divides the range of the 4 μm temperature (~290-525 K) into ~10 bins and computes the 25% quartile of the 11μm temperature within each 4 μm bin. Any temperatures that are less than the 11 μm 25% quartile are disregarded as potential fires (pink line in Figure 3.5b). However, if the 25% quartile is above 350 K, then the ICT threshold is set to 350 K. Any AMS data points above the resulting ICT minimum threshold line move on to be considered as fire hot spots (green triangles in Figure 3.5b).

3.4.2 Daytime and Nighttime Fire Detection Thresholds

The actual AMS fire detection thresholds (day and night) are calculated for both the 4 and 11 μm channels (orange lines in Figure 3.5) using the temperature histograms of each channel. During the day, considerable variability is added to the histograms from uneven surface heating and solar effects, making it difficult to separate the data points of the actively burning region. Even with this daytime noise, it is assumed that actively burning portions of a MODIS pixel will show some separation from the cooler portions in the histogram. Therefore, several bins with a low density in the 4 or 11 μm histograms are the starting point for the fire detection thresholds. At 11 μm, the histogram is searched, starting from the minimum threshold, for the first region with at least 5 bins

displaying a density less than two. The fire threshold is then set to the lowest value within the region of low density.

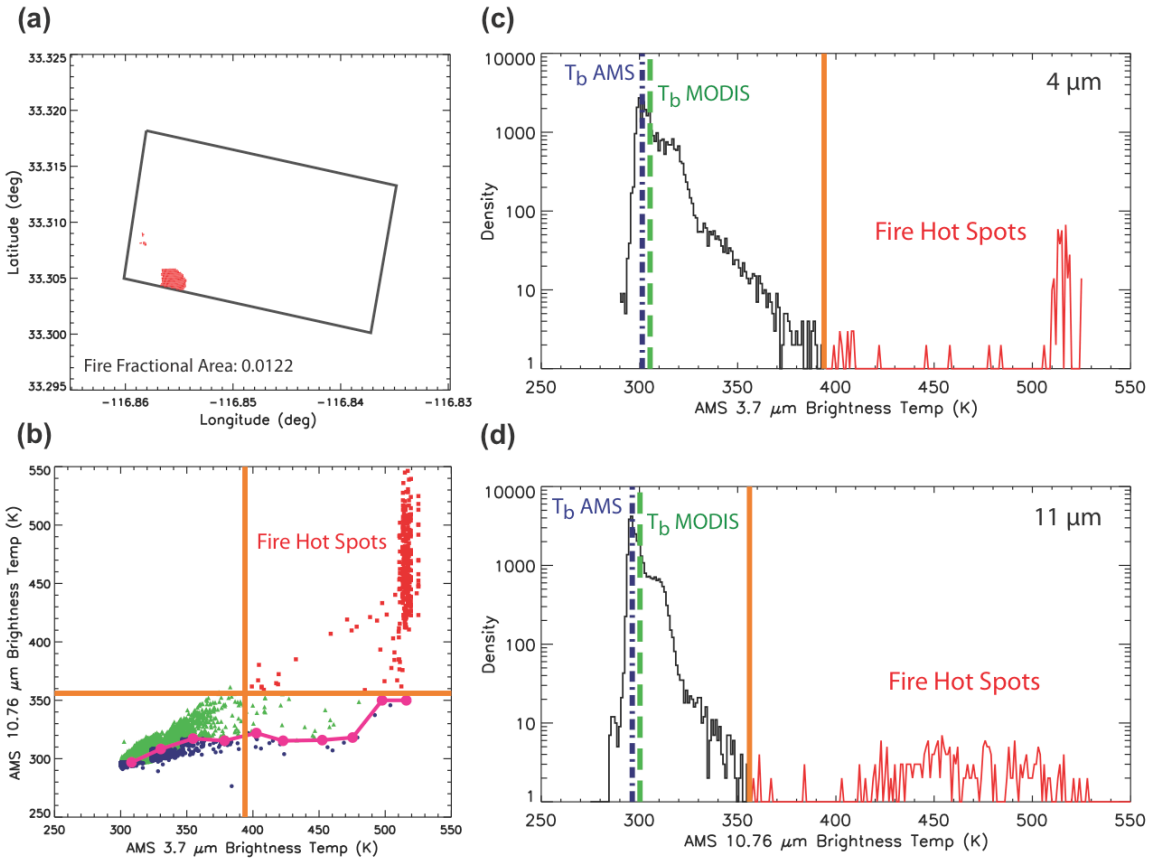

Figure 3.5: Example of AMS daytime fire detection within a MODIS pixel. (a) Map containing the AMS hot spot detections within a MODIS pixel. (b) Scatterplot of AMS 4 and 11 μm brightness temperatures. Blue dots indicate AMS data points disregarded as fires, green triangles indicate the region to be examined as potential fires, and red squares indicate the final AMS fire detection. Fire detection thresholds are displayed as solid orange lines and the minimum threshold is displayed as a solid pink line, with each dot corresponding to the center of an ICT test bin. (c) and (d) Histograms used in AMS fire detection at 4 μm and 11 μm, respectively. Fire detection thresholds are displayed as solid orange lines, and the MODIS and AMS background temperatures are respectively displayed as dashed green and dash-dotted blue lines.

The fire threshold method at 4 μm is slightly different due to saturation occurring between 510 and 530 K. It is assumed that any AMS pixel at the saturation level is hot enough to be considered. However, the remaining data between the ICT minimum threshold and the saturation level must also be investigated. The procedure begins by calculating the high temperature median (HTM), defined as the median of all AMS data points above the ICT minimum threshold. All AMS data points below the HTM are subsequently searched for a region of low density as in the 11 μm procedure. However, in this case, the region of low density is defined as a region with at least 4 bins displaying a density less than one. The limits are stricter than for 11 μm because the region under consideration is at relatively low temperatures and in many cases, the fire threshold will not exist below the HTM. In addition, the 4 μm data displays more variability at higher temperatures than 11 μm, which requires stricter limitations. As with 11 μm, the fire threshold is then set at the bin with the lowest value within the region of low density. If a region of low density is not found below the HTM, then the HTM itself is used as the 4 μm fire threshold.

The region of low density definition is very strict because the emphasis is on retrieving the actively burning region. If the density thresholds are increased, the retrieved fire area will be larger. However, increasing the density threshold by one at 4 and 11 μm will only produce a relative increase in fire area of approximately 10%. In contrast, increasing the density thresholds by three will increase the retrieved fire area by 40%. In this case, the 11 μm (4 μm) region of low density would be defined as the first region with at least 5 bins displaying a density less than five (four). Obviously, a much

larger region of the histogram would then be considered as fire. Therefore, the region of low density is based on the area of minimum sensitivity.

The nighttime fire thresholds are more straightforward than the daytime thresholds. Reduced background noise allows for a detection approach similar to MODIS, where separation is obtained by selecting pixels with temperatures that are a few standard deviations from the mean (Justice et al., 2002; Giglio et al., 2003). Specifically for AMS, the fire thresholds at 4 and 11 μm are set at two standard deviations from the mean (Figure 3.6). Regardless of daytime or nighttime, the 4 and 11 μm fire thresholds are not allowed to fall below 380 K and 340 K, respectively. These minimum values are rarely reached, but are necessary for MODIS pixels containing only a few hot AMS data points (very small fire fractions). Any AMS data points with a temperature greater than the 4 and 11 μm fire thresholds are flagged as fire hot spots (red squares in Figures 3.5b and 3.6b). The area of these AMS pixels is then summed to calculate the fire hot spot area within the MODIS pixel under consideration (assessment data, displayed in Figures 3.5a and 3.6a). In some cases, negative radiance values will occur adjacent to a region of hot, saturated AMS pixels. However, negative AMS radiance values usually comprise a very small faction of the total number of AMS pixels within a MODIS fire pixel footprint, and are currently disregarded.

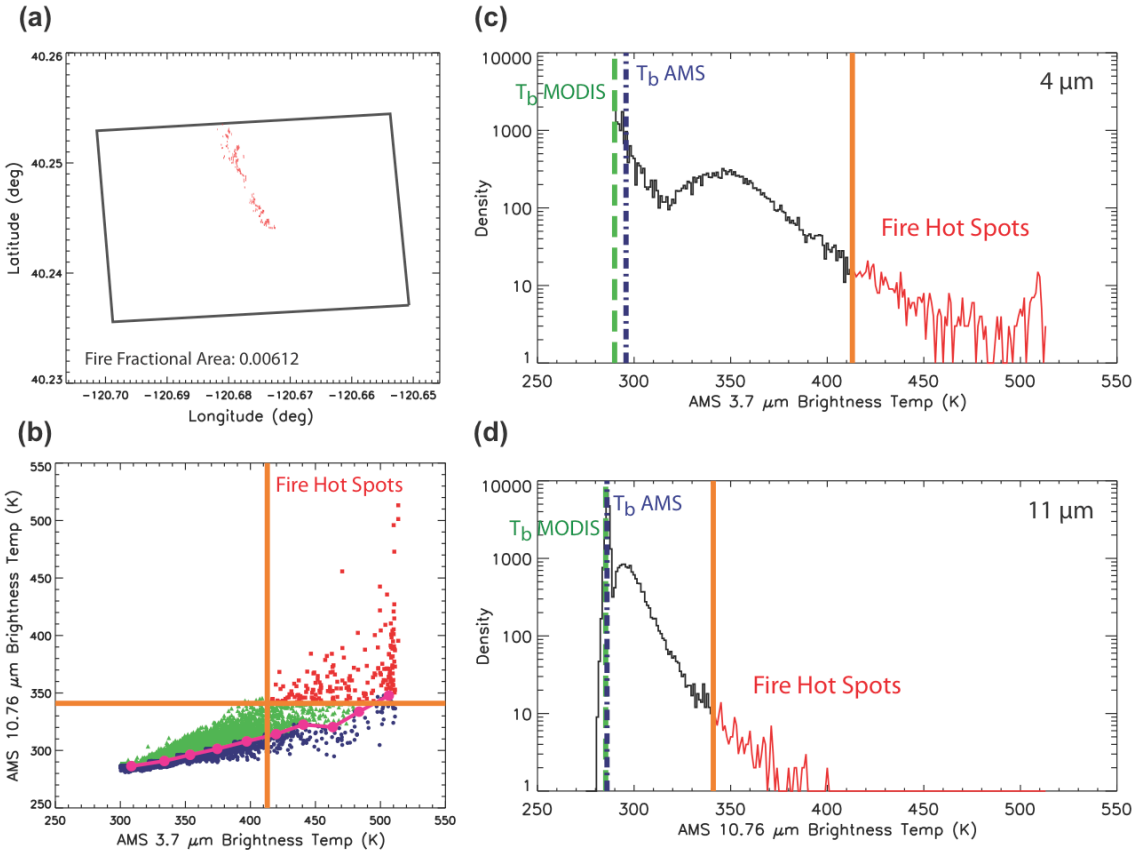

Figure 3.6: Same as Figure 3.5, but for AMS nighttime fire detection within a MODIS pixel.

3.5 Comparing the MODIS Retrieved Fire Area with AMS Observations

The ~15 meter resolution AMS fire data provide a direct ground assessment (in km^2) for the retrieved fire areas within each MODIS fire pixel. From a spatial perspective, Figure 3.7 shows that 12 of the 37 MODIS fire pixels have retrieved fire areas within 50% of the AMS value, while the fire area for 3 of the MODIS pixels cannot be retrieved due to background temperature mischaracterization. These 3 pixels have an 11 μm background temperature that is warmer than the fire pixel temperature, which

stems from the current MODIS fire detection algorithm and may be caused by heterogeneities (noise) in the region of background pixels (e.g. Kaufman et al., 1998a; Zhukov et al., 2006). Interestingly, there is a MODIS fire pixel in case #1 that does not contain any AMS fire hot spot detections, and is therefore the largest error displayed in Figure 3.7. This pixel was not flagged as high confidence by the MODIS fire detection algorithm and may be a MODIS false detection (described in the following section). The remaining 21 valid fire pixels display significant deviations in retrieved fire areas from the counterparts of the AMS observations, which is expected based on the large potential for pixel-level errors highlighted in earlier studies (e.g. Giglio and Kendall, 2001). Therefore, the following sections focus on the analysis of several indirect, random processes than can partially explain the large differences between the MODIS and AMS pixel-level fire areas.

3.5.1 Specifics of Pixel-Level Comparisons

For all MODIS fire pixels, AMS and MODIS fire area comparisons (Figure 3.8a-d) have shown promise for a fire area greater than ~0.001 km^2 (1000 m^2), which corresponds to a fire area fraction of 0.001 in a 1 km^2 MODIS pixel. While the overall bias is low, pixel-by-pixel differences in AMS-MODIS fire areas are significant, producing a modest correlation (R = 0.59). It is also interesting that all 33 fire pixels displayed in Figure 3.8a-d have an AMS observed fire area greater than 0.001 km^2 (1000 m^2), which is above the lower limit of MODIS fire detection for a reasonable retrieval accuracy (Giglio et al., 2003). Even though few fire pixels have an AMS fire area between 0.0001 km^2 and 0.003 km^2, a range that is expected to have the greatest potential for error in the retrieval, it is still generally observed that the relative variation in

retrieved fire area is smaller for larger fires (> 0.015 km^2) and larger for AMS fire areas below 0.01 km^2.

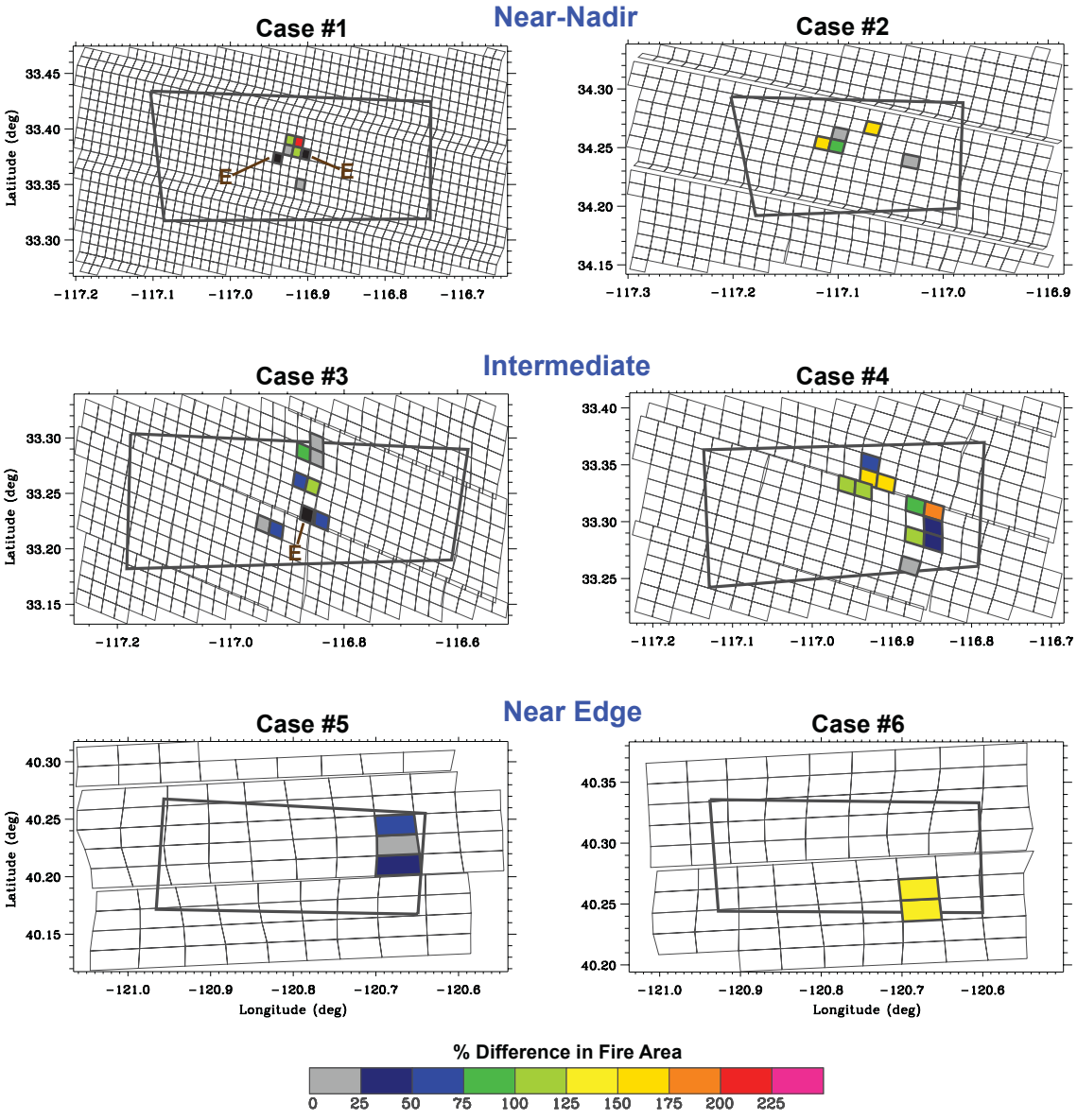

Figure 3.7: Spatial representation of all six case studies in California. The large black polygons denote the boundaries of the AMS scan and smaller grey polygons represent the MODIS pixel mesh (corrected for overlap). The MODIS fire pixels are shaded in color based on the percent difference between the AMS observed and the MODIS retrieved fire area. The three pixels shaded in black and corresponding to a brown "E" indicate where the MODIS background temperature was higher than the fire pixel temperature (retrieval error). The viewing zenith angle increases from case #1 (13^o) to case #5 and #6 (64^o).

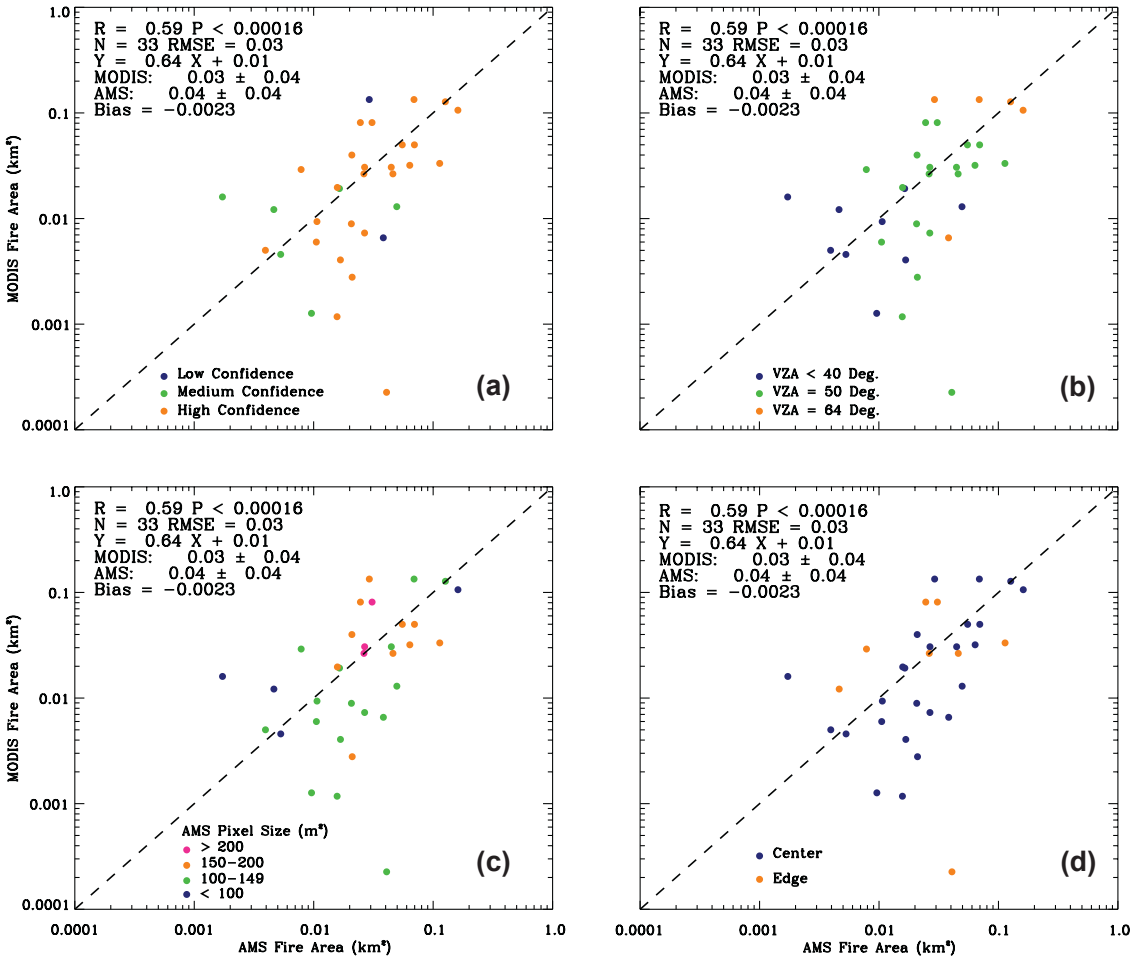

Figure 3.8: Pixel-level comparisons between retrieved MODIS fire area and AMS observed fire area from all six collocated cases. (a) Color scheme indicates the fire detection confidence level provided by the MODIS fire product. (b) Color scheme indicates the viewing zenith angle (distance from nadir). (c) Color scheme indicates the variation in AMS pixel size (based on Figure 3.4). (d) Color scheme separates the pixels with distinct sub-pixel hot spots located on the pixel edge from the remaining pixels. The statistics corresponding to the color schemes in (a-d) are presented in Table 3.2. For display purposes, (a-d) use a log vs. log scale. However, the statistics reflect the linear regression.

The MODIS fire product provides detection confidence levels for each fire pixel (Giglio, 2010), which can be investigated in the context of the sub-pixel results (Figure 3.8a, Table 3.2). For example, the majority of fire pixels in the six case studies are

flagged as high confidence with only eight pixels flagged as medium or low confidence. AMS observations show that the high confidence pixels contain the largest mean fire area (0.043 km^2). In contrast, the medium confidence pixels have a much smaller mean fire area (0.015 km^2), which is expected because the smaller sub-pixel fire area likely produces a fairly small increase in mean pixel brightness temperature. Therefore, the current MODIS algorithm may reduce the confidence level for these pixels. The two low confidence pixels actually have rather large fire areas, but also have a very large bias in retrieved fire area. In contrast, the bias is greatly reduced with the high confidence pixels (-11.62%), suggesting that the results from higher confidence pixels show stronger agreement with the AMS observations (Table 3.2). This observation suggests that the MODIS low and medium confidence levels generally represent the small fires or the outliers in the retrieved sub-pixel areas, at least for the pixels used in this study.

Surprisingly, the location relative to nadir has a minimal effect on the retrieved fire area bias (Table 3.2), but pixels with larger VZAs have a large mean retrieved fire area of 0.102 km^2, while the pixels with small VZAs have a lower mean retrieved fire area of 0.009 km^2. This observation is expected because the MODIS pixel size increases dramatically with large VZAs, resulting in an increase in the smallest detectable (and retrievable) fire area (Giglio, 2010). However, all cases, regardless of pixel location, display considerable variability at the pixel-level with some retrieved fire areas matching the AMS observations and other pixels deviating from AMS by an order of magnitude or more (Figure 3.8b). Therefore, it is likely, and will be shown below, that other indirect factors, such as the size and location of the fire within the pixel, have the greatest impact

on the retrieval results. The potential impacts from variations in AMS pixel geometry (as displayed in Figure 3.4) are considered in Figure 3.8c, but this does not seem to have a major impact on the assessment results.

Table 3.2: Statistics corresponding to the color scheme used in Figure 3.8a-d[1]

Variable (Indirect Effect)	# Pixels Out of 33	Mean AMS Fire Area km^2	Mean MODIS Fire Area km^2	Bias km^2	Bias %
MODIS Confidence Level (Figure 3.8a)					
Low	2	0.034	0.070	0.036	105.88
Medium	6	0.015	0.011	-0.004	-26.67
High	25	0.043	0.038	-0.005	-11.62
Viewing Zenith Angle (Figure 3.8b)					
VZA < 40 Deg.	9	0.013	0.009	-0.004	-30.77
VZA = 50 Deg.	19	0.035	0.029	-0.007	-20.00
VZA = 64 Deg.	5	0.085	0.102	0.017	20.00
AMS Pixel Size (Figure 3.8c)					
> 200 m^2	3	0.028	0.046	0.018	64.29
150 - 200 m^2	10	0.046	0.047	0.001	2.17
100 - 149 m^2	16	0.032	0.025	-0.007	-21.88
< 100 m^2	4	0.043	0.035	-0.009	-20.93
Location of Sub-Pixel Hot Spots (Figure 3.8d)					
Center	25	0.037	0.034	-0.003	-8.11
Edge	8	0.037	0.036	-0.001	-2.70

1. Negative bias indicates the mean AMS fire area is greater than the mean MODIS retrieved fire area.

Drawing from earlier studies (e.g. Calle et al., 2009), the impacts from the 4 and 11 μm PSFs (e.g. Figure 2.1) must be investigated by examining the sub-pixel physical disposition of fire. For example, sub-pixel fire hot spots near the edge of a pixel will likely result in an underestimated fire pixel brightness temperature, while fires near center of a pixel may overestimate the pixel's brightness temperature. Similarly, a fire located on the boundary between pixels, will likely increase the brightness temperature of both pixels. This may help to explain the probable MODIS false detection in case #1

because the pixel boundaries (on two sides) are located near the sub-pixel fire hot spots contained within the adjacent pixels.

A closer examination of the AMS fire data, displayed in Figure 3.9, indicates that there are three major distributions of fire hot spots within the MODIS fire pixels used in this study: (1) center hot spot pixels, (2) edge hot spot pixels, and (3) a long fire front, which bisects the pixel. By using similar visualization methods, it was discovered that 8 of the 33 MODIS fire pixels contain pixel-edge fire hot spots (Figure 3.8d). The center and edge hot spot pixel samples have nearly identical mean observed and retrieved fire areas with a very low bias (Table 3.2), but 6 of the 8 edge cases show significant deviations in retrieved fire area from the AMS observations and the pixel with the largest error in retrieved fire area is an edge case. The low bias in Table 3.2 results from similar magnitudes of overestimated and underestimated retrieved fire areas for the 8 pixels containing edge hot spots. In the non-edge hot spot cases, especially those with distinct center hot spots (e.g. Figure 3.9a), it is possible that error may be introduced from a pixel brightness temperature that is overestimated (a potential bias). However, the edge cases are more likely to suffer from inter-channel, PSF coregistration errors (Shephard and Kennelly, 2003; Calle et al., 2009), and are therefore more likely to increase the potential for error in the sub-pixel retrieval output.

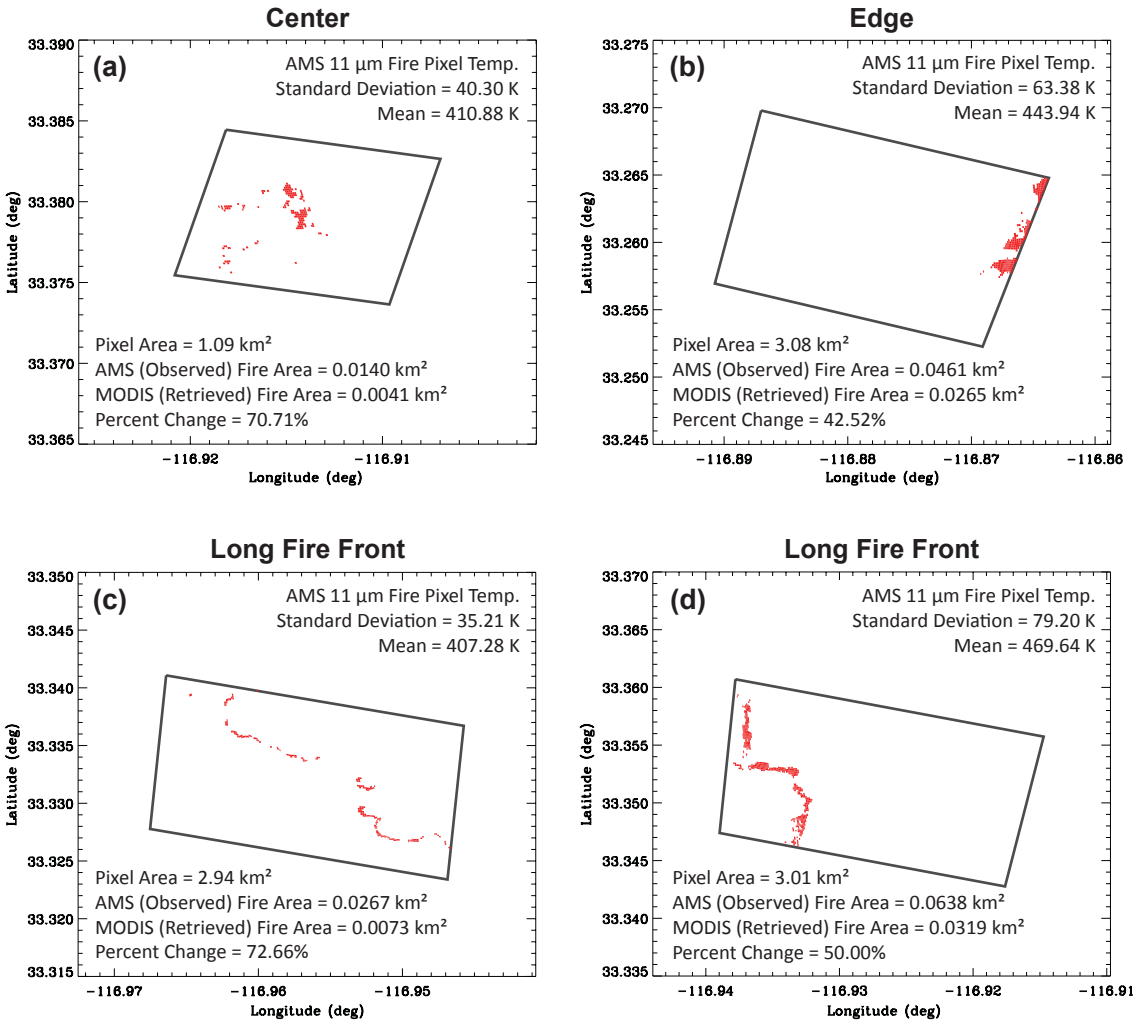

Figure 3.9: Spatial display of the sub-pixel fire region within four MODIS fire pixels showing (a) center hot spots, (b) edge hot spots, and (c), (d) long fire front situations. Black polygons indicate the boundaries of the MODIS fire pixels and red shading indicates the locations of fire hot spots as observed by the AMS.

Along with PSF effects, the combination of sub-pixel fire size, temperature, and the overall distribution of sub-pixel hot spots can affect the retrieved fire area. For example, Figure 3.9a,b shows a somewhat counterintuitive result where the center hot spot case has a larger error in retrieved fire area (70.71%) than the edge hot spot case (42.52%). The 11 µm AMS channel, though limited by reduced sensitivity at high

temperatures, shows that the edge case has a much higher mean fire temperature (443.94 K) than the center case (410.88 K) and both cases are very heterogeneous (large standard deviation). Hot spots occupy about the same fractional area of each pixel (~0.01 for the 1 and 3 km^2 pixels), but the edge hot spot case contains an organized, large cluster of hot spots and the center hot spot case contains a more diffuse hot spot cluster spread over a large portion of the pixel. Therefore, it is possible that the pixel brightness temperature of the edge hot spot case is more representative of the observed sub-pixel fire properties than the center hot spot case, even when considering PSF effects. Similarly, the fire front case in Figure 3.9c has a larger error in retrieved fire area (72.66%) than Figure 3.9d (50.00%), but, unlike Figure 3.9a,b, the fire fronts in Figure 3.9c,d do not occupy the same area fraction of the ~3 km^2 pixels. Figure 3.9c contains a small and very narrow fire front with a low 11 μm mean fire temperature (407.28 K), while the fire front in Figure 3.9d is much larger and highly concentrated, with a higher 11 μm mean fire temperature (469.64 K). Therefore, this analysis confirms that fire pixels containing high temperature, large, and highly concentrated regions of sub-pixel fire hot spots are likely to produce the most accurate retrieved fire areas, especially when located near the center of the pixel.

The comparisons in Figures 3.8a-d and 3.9a-d show the individual indirect effects (not originating from input variables) on the sub-pixel retrieval. These results suggest that multiple factors, such as a lower confidence fire pixel with pixel-edge hot spots, contribute to the large variability observed in the retrieved pixel-level fire area. Therefore, to visualize an ideal situation for the sub-pixel retrieval, the low and medium confidence fire pixels are removed (Figure 3.10a) and the resulting correlation between

MODIS and AMS shows a slight increase (R = 0.67). When the fire pixels with pixel-edge hot spots are also removed (Figure 3.10b), the correlation becomes much stronger (R = 0.84) and the variability between MODIS and AMS is reduced. This suggests that the combination of lower confidence fire pixels, typically from small sub-pixel fires (Figure 3.8a) and PSF effects (Figure 3.8d), including the distribution of sub-pixel hot spots (Figure 3.9a-d), have the largest indirect impact on the accuracy of the retrieval. Similar to Figure 3,8a-d, the results in Figure 3.10b show a relatively low bias, but this accuracy is obtained by excluding 45% of the available fire pixels. When considering global fire observations, many cases of low confidence pixels are likely to exist, especially in regions with agricultural burning, and real-world applications would not be able to separate pixel-center from pixel-edge sub-pixel fires.

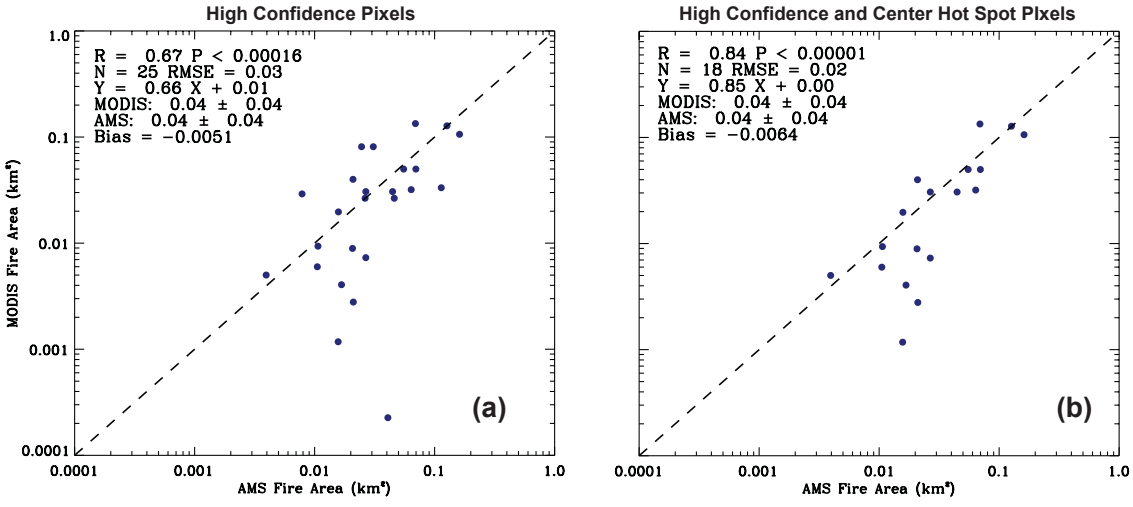

Figure 3.10: Idealized pixel-level comparisons between retrieved MODIS fire area and AMS observed fire area using all six collocated cases, but showing only (a) the high confidence fire pixels and (b) the combination of high confidence and center hot spot fire pixels. For display purposes, (a) and (b) use a log vs. log scale. However, the statistics reflect the linear regression.

3.5.2 Clustering-Level Comparisons

While the AMS initial assessment algorithm enables the identification of fire pixels that have the greatest uncertainty in the retrieval, the majority of the future applications of the sub-pixel algorithm will not have these data available. Therefore, the sub-pixel retrieval will have to rely on a clustering methodology to increase the accuracy of the retrieved fire area. The results from the two clustering methods (Figure 3.11) show stronger agreement than the pixel-level results. The clustering sum method of pixel-level retrievals produces the highest correlation (R = 0.91) suggesting that the random variation can be reduced by averaging, when looking at a fire event as a whole. The single retrieval method from averages also produces a high correlation (R = 0.84), but may be limited by the larger surface area used in the retrieval, where the contrast between fire and background may be reduced. Regardless, comparisons between the clustering and pixel-level results highlight the importance of averaging to reduce errors that are difficult to characterize on a per-pixel basis, such as the distribution of sub-pixel fires (Figure 3.9a-d), general PSF effects (Figure 3.8d), and PSF coregistration errors.

The fire clusters in Figure 3.11 are currently defined as all MODIS pixels within an AMS scan, allowing for only six fire clusters and creating difficulty when discerning any impact from VZA and day/night cases. However, as with the pixel-level results, the larger VZA clusters generally display larger retrieved fire areas than the small VZA cases with a small bias toward larger AMS fire areas. Both clustering methodologies will likely improve estimates of retrieved fire area for large fire events, but future implementation of the single retrieval from averages method will require a strict definition of what constitutes a cluster in any given MODIS granule. Therefore, the sum

of pixel-level retrievals method may be more advantageous because the definition of a cluster can be changed as needed. Unfortunately, isolated, small fires may only include one or two fire pixels and will not benefit from either clustering methodology.

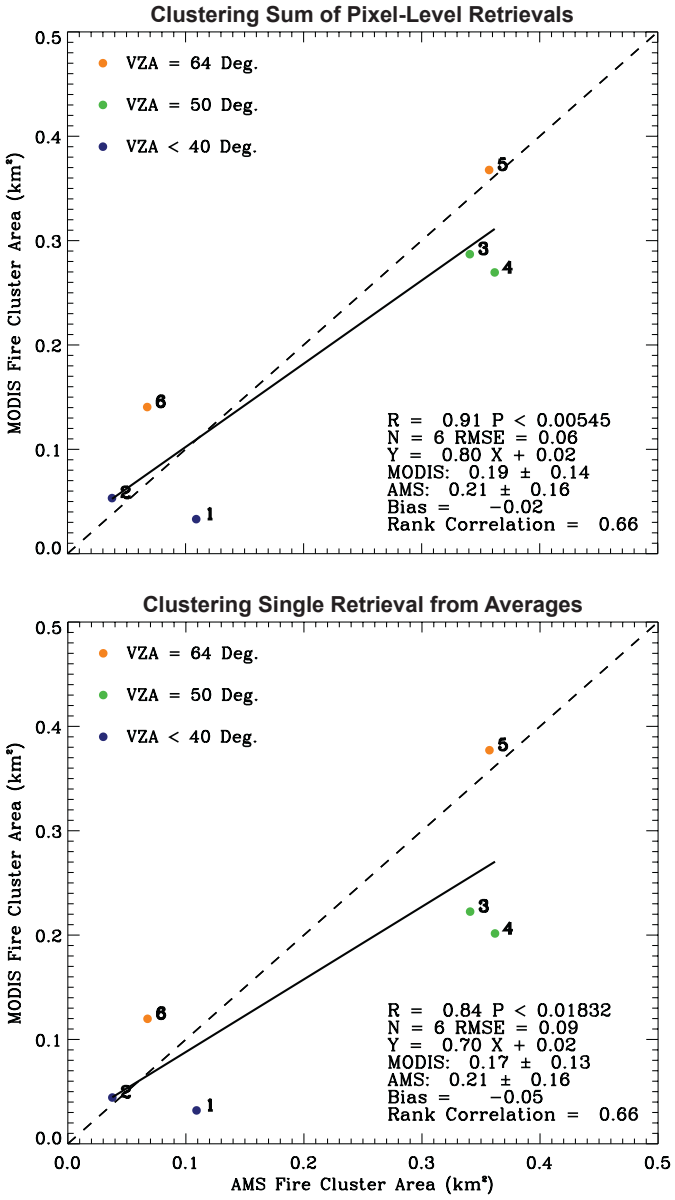

Figure 3.11: Cluster-level comparisons between retrieved MODIS fire area and AMS observed fire area for all six collocated cases. (Top) Clustering using the sum of pixel-level retrievals method. (Bottom) Clustering using the single retrieval from averages method. Solid line corresponds to the linear fit equation and collocation case labels correspond to the first column of Table. 3.1. The color scheme is based on the viewing zenith angle (distance from nadir).

3.6 Comparing the Sub-Pixel-Based FRP_f with the Current MODIS FRP_p

With saturation occurring at higher temperatures in the AMS 4 μm channel, and thus providing very little data to validate retrieved fire temperatures, the comparison between the current MODIS FRP_p and FRP_f is the only available method to assess the overall consistency of MODIS sub-pixel fire retrievals. The pixel-level comparisons from all 6 collocation cases (Figure 3.12a) produce a strong correlation (R = 0.93), which suggests that the sub-pixel retrieval can generate acceptable fire temperatures, even at the pixel level. However, the sensitivity analysis for the BIRD satellite (e.g. Zhukov et al., 2006) showed that the errors in retrieved fire area and temperature may counteract each other in a sub-pixel-based FRP calculation (equation 1.2). As a result, fire temperature errors may be present regardless of the accuracy in the retrieved fire area. When considering this dilemma and the lack of accurate 4 μm temperature validation data, the retrieved fire temperature should be used with caution, and only when FRP_f is not sufficient to examine the problem of interest.

In contrast to the fire area results in the previous sections, Figure 3.12b shows that the off-nadir pixels (large VZAs) commonly have a much larger difference between FRP_p and FRP_f than cases close to nadir (small VZAs). The reason stems from the best-fit methodology of the MODIS FRP_p in combination with off-nadir pixel growth. For example, the size of the MODIS pixels displayed in Figure 3.7 can grow to over 8 km^2 near the edge of the satellite ground swath (cases #5 and #6). In these cases, the background region of the pixel becomes very large, suggesting that the flaming region will contribute less to the observed pixel radiance. The FRP_p is also based on a top-of-

atmosphere observation and the longer path lengths at large VZAs may mask the signal of fires. As a result, FRP_p will likely be much lower than FRP_f, which is indeed observed in most off-nadir pixels in Figure 3.12a,b. Similarly, when FRP_p is divided by the pixel area, lower values (large-area pixels) will result in a greater potential for error in the MODIS FRP_p estimate. Therefore, with atmospheric effects taken into consideration, FRP_f is likely an improved methodology for off-nadir fire pixels, but produces results similar to FRP_p for the remaining pixels.

The real motivation for choosing FRP_f over FRP_p becomes obvious when FRP_f is used in combination with the retrieved fire cluster area. This can be illustrated by comparing the cluster-level FRP_p flux to the FRP_f flux, given by

$$FRP_p Flux = \frac{\sum_{i=1}^{n} FRP_{p_i}}{\sum_{i=1}^{n} A_{p_i}} \tag{3.1}$$

$$FRP_f Flux = \frac{\sum_{i=1}^{n} FRP_{f_i}}{\sum_{i=1}^{n} A_{f_i}} \tag{3.2}$$

where the output is provided in units of Wm^{-2} per fire pixel cluster (Figure 3.12c,d). The FRP_f flux and FRP_p flux are strongly correlated for both the sum method ($R = 0.83$) and the single retrieval method ($R = 0.89$). Furthermore, a strong rank correlation ($R_{rank\ sum} = 0.89$ and $R_{rank\ single} = 0.66$) suggests there is a strong monotonically increasing relationship between the FRP_f and FRP_p fluxes. While limited by a small sample size, Figure 3.12c,d shows that the magnitude of FRP_f flux ranges from ~3000 to 10000 Wm^{-2},

and the FRP_P flux ranges from ~20 to 80 Wm^{-2}. Obviously, the magnitude of the FRP_f flux (based on retrieved fire area) is more realistic for the large fire clusters used in this study.

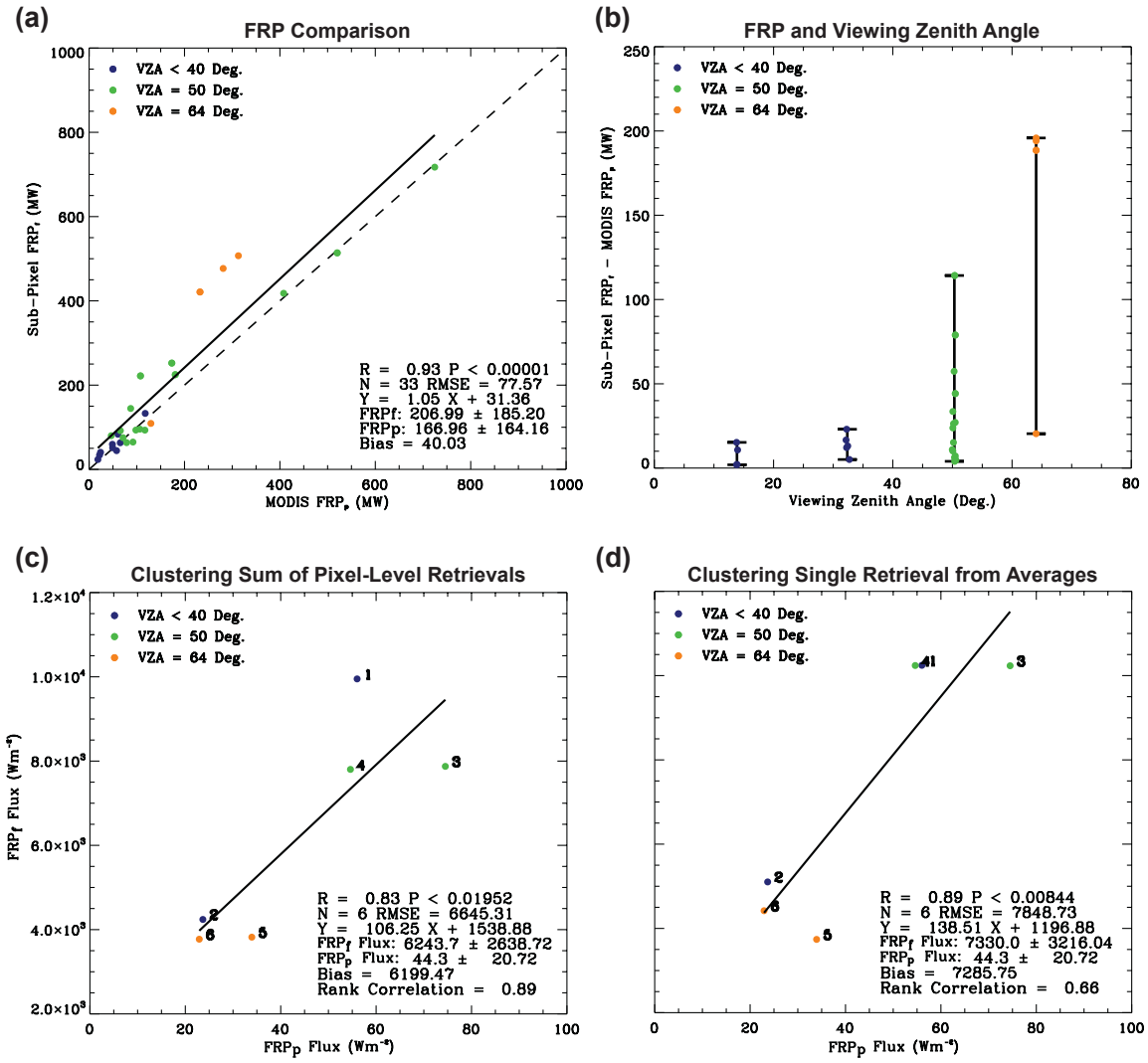

Figure 3.12: (a) Pixel-level comparison between FRP_p (current MODIS pixel-based FRP) and FRP_f (sub-pixel-based FRP) for all six cases. Solid line corresponds to the linear fit equation. (b) $FRP_f - FRP_p$ as a function of viewing zenith angle. (c) Cluster-level comparison between FRP_p per cluster area (FRP_p flux) and FRP_f per fire area (FRP_f flux) for all six cases using the sum of pixel-level retrievals method. (d) Same as (c) but for the single retrieval from averages method. Solid line corresponds to the linear fit equation and collocation case labels correspond to the first column of Table. 3.1. The color scheme is based on the viewing zenith angle (distance from nadir).

Along with an improved quantification of fire intensity, FRP_f flux can be used to examine the basic properties of a fire event by differentiating large fires burning at a low FRP_f from small fires burning at a high FRP_f. For example, the cluster fire area in case #5 is one of the largest (~0.38 km^2), while the FRP_f flux is one of the smallest (~3900 Wm^{-2}). In fact, both large VZA cases (#5 and #6) have the smallest FRP_f fluxes, which are expected because they are nighttime cases. Therefore, the general fire evolution and smoke plume characteristics in case #5 may be considerably different than case #1, which contains a relatively small fire cluster area (~0.01 km^2) with a much larger FRP_f flux (~10000 Wm^{-2}). These types of comparisons demonstrate the potential utility of the sub-pixel retrieval for providing a detailed characterization of any given fire event, and show that FRP_f flux may be useful for providing improved estimates of initial smoke plume buoyancy and injection heights. However, more observational analysis is needed to support this hypothesis (see Chapter 6).

3.7 Summary

For the first time, the near-coincident observations obtained from the AMS, flown aboard the NASA Ikhana UAS, allowed the retrieved MODIS sub-pixel fire area results to be assessed with unprecedented accuracy (3-50 meter resolution). This initial assessment showed that pixel clustering should be implemented to reduce errors that are difficult to characterize on a per-pixel basis, such as those from PSF differences, and the clustering sum of individual retrievals method may have the greatest relevance to future

operational algorithms. Comparisons between the AMS and MODIS fire areas revealed the impacts from several indirect effects on the retrieval that are difficult to characterize, such as PSF effects, location relative to nadir (viewing zenith angle), and the overall distribution of sub-pixel hot spots within the fire pixel. In addition, a strong correlation ($R = 0.93$) was found between the fire area/temperature-based FRP_f and the current pixel-based MODIS FRP_p. This suggests that the sub-pixel-based calculation of FRP_f has the same merit as the current FRP_p, but contributes information that the current MODIS product is lacking. For example, retrieved cluster fire area, along with the sub-pixel-based FRP_f, allowed a large fire burning at a low intensity to be separated from a small fire burning at a high intensity, and also facilitated calculations of FRP_f flux over the retrieved fire area.

Chapter 4. Sensitivity Analysis

4.1 Introduction

In Chapters 2 and 3, a modified sub-pixel retrieval was developed to account for atmospheric effects and variations in Earth-satellite geometry for MODIS fire pixels, with the goal of application to future satellite sensors (e.g. NPP VIIRS and GOES-R). Since the algorithm development and initial assessment have been accomplished, this chapter focuses on the uncertainty introduced to the sub-pixel retrieval algorithm from errors in the estimated or assumed values of three primary direct input variables: (1) background brightness temperature, (2) background emissivity, and (3) the atmospheric column water vapor amount.

These variables may introduce uncertainty into the retrieval outputs because they are required for the creation of the lookup tables (equations 2.3 - 2.6). In addition, the sub-pixel retrieval is only applied to the pixels that are flagged as fire pixels by the standard MODIS fire product, and is therefore subject to any limitations from the MODIS fire detection algorithm. Several earlier studies (e.g. Giglio and Kendall, 2001; Zhukov et al., 2006) have shown that temperature variations (noise) within the background region, especially at 11 μm, have the potential to dramatically affect the output of a sub-pixel retrieval. However, the potential impacts resulting from an improper assumption of background emissivity or the atmospheric column water vapor amount (used for atmospheric correction) have not been quantitatively analyzed, and are paramount to understanding the overall sensitivity of this sub-pixel retrieval.

With the recent aid of high-resolution AMS observations, deviations in retrieved fire area resulting from errors in these direct input variables and the subsequent effects on FRP_f can be assessed in great detail. Therefore, this chapter builds upon earlier sub-pixel sensitivity studies by providing a detailed quantitative assessment of the current retrieval's sensitivity to variables (1) - (3), which are described in Sections 4.2, 4.3, and 4.4, respectively. As displayed in Figure 4.1, this chapter incorporates the same California test cases and AMS data used to assess the sub-pixel algorithm in Chapter 3, but also requires information on local vegetation type and topography.

4.2 Atmospheric Profile

Considering that the AMS fire data used in this study are for California fire events occurring in the late summer or early fall (Figure 4.1), the atmospheric profile in SBDART is assumed to be a representative, climatologically based mid-latitude summer profile (default profile) for the Continental United States, which includes 2.92 g/cm^2 of water vapor in the atmospheric column (McClatchey et al. 1972; Ricchiazzi et al., 1998). However, the day-to-day relative change of water vapor will likely have an effect on the retrieval, and therefore the sensitivity of the 4 and 11 μm channels to water vapor amount must be examined.

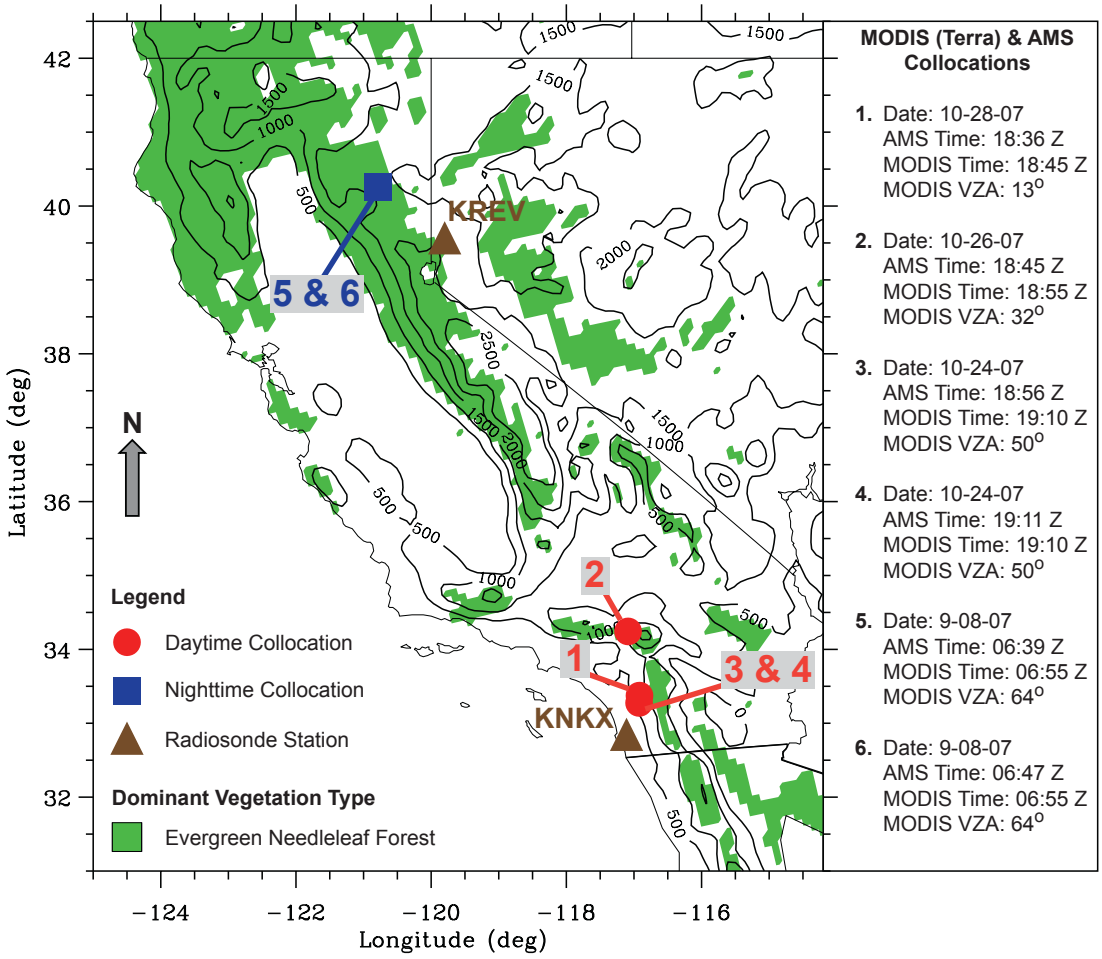

Figure 4.1: Map showing the locations of the six California test cases as red circles (daytime) or a blue box (nighttime). The specifics of each MODIS and AMS collocation are provided in the side panel, with the viewing zenith angle (VZA) corresponding to the mean VZA for all MODIS fire pixels in each test case. Green shading indicates regions where evergreen, needle-leaf forest is the dominant vegetation type and black contours indicate variations in topography, with a contour interval of 500 meters. In addition, the locations of the two relevant radiosonde stations are displayed as brown triangles (see Section 4.2.1 for details).

4.2.1 Variations in Water Vapor Amount and Temperature

As shown by Kaufman et al. (1998a), water vapor absorption is minimal in the primary (3.96 μm) MODIS fire detection channel, but the impact at 11 μm is less certain. Figure 4.2a,b is based on the column water vapor amount, and shows comparisons between the surface kinetic temperature (T_{sfc}) and the TOA brightness temperature (BT_{TOA}) for a test case near nadir (case #1, mean VZA = 13^o) and a test case at the edge of a given scene (cases #5 and #6, mean VZA = 64^o). From this display, it is immediately evident that an atmospheric correction is required for the 11 μm channel, evidenced by 11 μm BT_{TOA} values that are at least 100 K cooler than T_{sfc} (when T_{sfc} > ~700 K), especially when the VZA is 64^o (longer path length). At the 4 μm background BT_{TOA} range, commonly 290 - 315 K, the difference between T_{sfc} and BT_{TOA} is very small (< 10 K), and is the primary reason for not correcting the MODIS 4 μm background temperature (T_{4b}) in the FRP_f equation (1.2). However, an atmospheric correction does become necessary as the 4 μm surface temperature increases (presumably from fire) because the relative change between T_{sfc} and BT_{TOA} remains approximately the same. For example, a T_{sfc} of 400 K will produce a 4 μm BT_{TOA} that is ~8 K (16 K) cooler when the VZA is 13^o (64^o), but this change grows to ~80 K (160 K) when the surface temperature warms to 1400 K.

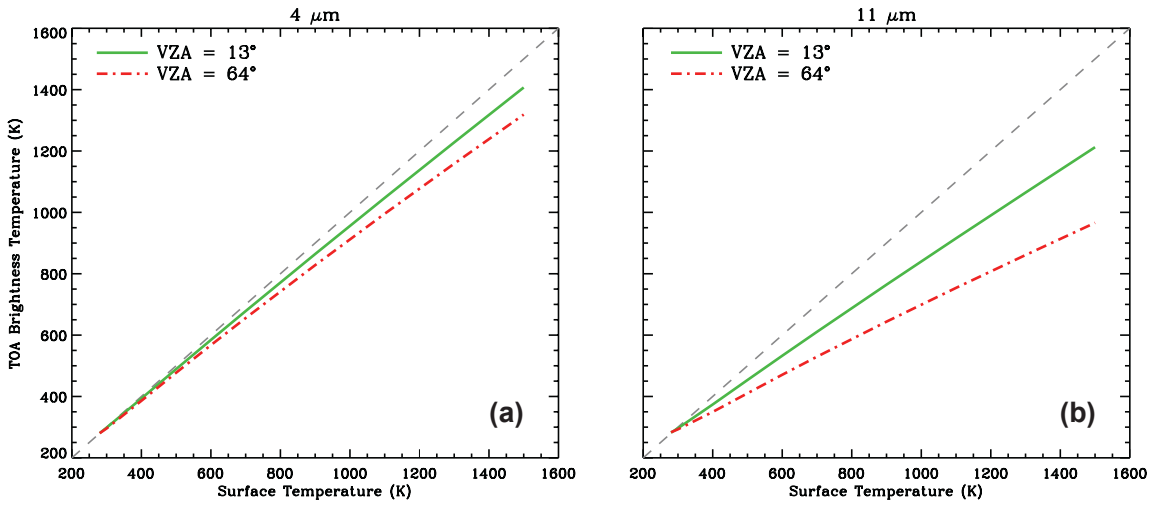

Figure 4.2: Comparisons between T_{sfc} and BT_{TOA} using the mid-latitude summer column water vapor amount (2.92 g/cm^2) for the 4 μm channel (a) and the 11 μm channel (b). This case corresponds to a fixed SZA of 48^o and RAZ of 165^o. VZAs of 13^o and 64^o are respectively denoted by the solid green and dashed red lines.

The deviations in BT_{TOA} relative to the values obtained in Figure 4.2a,b are displayed in Figure 4.3a-d as a function of T_{sfc} and several potential column water vapor amounts. At 4 μm (Figure 4.3a,c), a large increase or decrease in column water vapor (from the mid-latitude summer value) will produce small changes in BT_{TOA}, falling within the ranges of ±14 K and ±26 K when the VZA is respectively 13^o and 64^o, for any given T_{sfc} value. In contrast, the steep slope and tight gradient of the contours in Figure 4.3b,d shows that the 11 μm BT_{TOA} is much more sensitive to small changes in column water vapor than 4 μm, especially when T_{sfc} is high (e.g. > 1000 K). In these cases, the 11 μm BT_{TOA} can change by more than ±100 K. The impact of water vapor absorption is even more significant at the VZA of 64^o (Figure 4.3d), where deviations in BT_{TOA} of more than ±200 K can occur for relatively small changes in column water vapor amount, especially for high values of T_{sfc}.

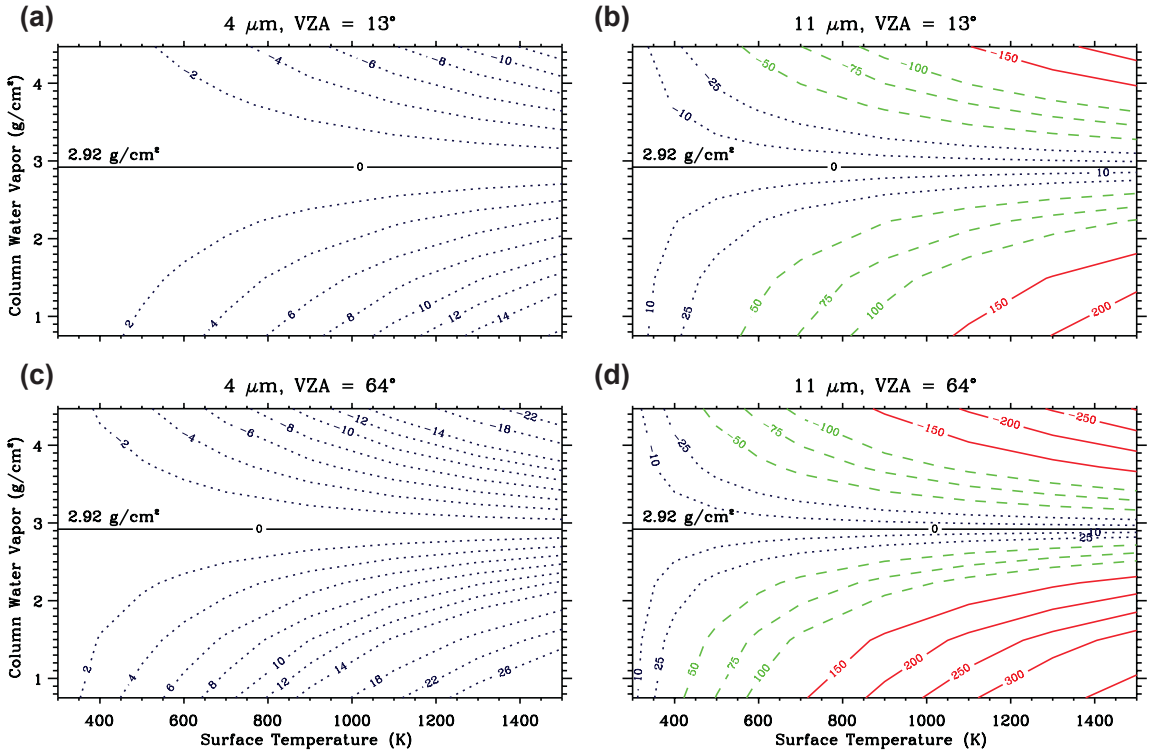

Figure 4.3: Sensitivity to variations in atmospheric column water vapor amount displayed as the change in BT_{TOA} relative to the values obtained using the mid-latitude summer column water vapor amount (Figure 4.2) as a function of T_{sfc} and column water vapor amount. The 4 and 11 μm channels are respectively displayed in (a) and (b) for the viewing zenith angle of 13°. Similarly, (c) and (d) correspond to the viewing zenith angle of 64°. The solid, black contour indicates the mid-latitude summer column water vapor amount and dotted blue, dashed green, and solid red contours indicate a positive (or negative) change in BT_{TOA} of < 50 K (> -50 K), 50 to 149 K (-50 to -149 K), and ≥ 150 K (≤ -150 K), respectively. This case corresponds to a fixed SZA of 48° and RAZ of 165°.

The larger impact of column water vapor amount on the 11 μm BT_{TOA} partially results from a relatively large reduction in atmospheric transmission (as compared to the counterparts at 4 μm). For example, the mid-latitude summer water vapor profile (2.92 g/cm^2) produces a transmissivity of about 0.96 and 0.87 at 4 and 11 μm, respectively. However, a modified profile, containing 1.1 g/cm^2 of column water vapor, produces 4

and 11 μm transmissivities of 0.98 (2% change) and 0.93 (7% change), respectively. In addition, the BT_{TOA} of a fire pixel may increase relatively less at 11 μm when compared to 4 μm because the wavelength of peak emission shifts toward shorter wavelengths as the temperature increases (e.g. Wein's Law). Therefore, the combination of increased water vapor absorption and lower sensitivity to warm temperatures likely explains the large surface to TOA temperature differences observed at 11 μm in Figure 4.3b,d, which may ultimately affect the accuracy of the bi-spectral, sub-pixel retrieval.

In many California fire events, the atmospheric water vapor amount will be low, especially near the surface, ultimately resulting in a lower column water vapor amount than the mid-latitude summer profile. In fact, most of the test cases are associated with a Santa Ana synoptic pattern and cloud cover effects are minor, even in the northern California test cases (#5 and #6). MODIS level-2, Collection 5 water vapor data (MOD05_L2/MYD05_L2, http://ladsweb.nascom.nasa.gov/data/search.html, King et al., 2003) show that the column water vapor in the vicinity of the six test cases ranges from about 0.75 to 1.70 g/cm^2, which is a considerable deviation from the mid-latitude summer value of 2.92 g/cm^2 and falls near the minimum value considered in Figure 4.3a-d. Any impacts from variations in the temperature profile are also uncertain.

Based on the potential for large, regional deviations in the atmospheric profiles, a mean observed sounding from all six test cases was derived and compared to the mid-latitude summer SBDART profile. For the southern California test cases (#1-4 in Figure 4.1), observed soundings were obtained from San Diego, California (station KNKX, #72293), while Reno, Nevada (station KREV, #72489) was used for the Northern California test cases (#5-6 in Figure 4.1). With the MODIS overpass occurring near the

midpoint between the 12:00 Z (day 1) and 00:00 Z (day 2) sounding times for test cases #1-4 (between 00:00 Z and 12:00 Z on day1 for test cases #5-6), the sounding at the time of the MODIS overpass is simply the mean of the a priori and a posteriori soundings. The observed atmospheric profile (to be compared with the mid-latitude summer profile) can then be produced by calculating median of the four mean water vapor and temperature profiles coincident with the four MODIS overpasses. Figure 4.4a,b shows that the mid-latitude summer temperature profile falls within the observed range of temperature at many levels, but there are differences of 2-5 K near the surface (inversion effects) and differences approaching -10 K near the tropopause.

The observed profile is computed using only the mandatory pressure levels, which are subsequently interpolated to the levels of the SBDART input sounding. As a result, the column water vapor amount may have a dry bias, but the impact could be mitigated if more levels were considered or if the local sounding observation times were closer to the MODIS overpass times. For example, the total column water amount of the observed profile ranges from 0.59 to 1.35 g/cm^2, which is lower than the range of 0.75 to 1.70 g/cm^2 provided by MODIS water vapor data. However, both techniques show there is a considerable deviation from the mid-latitude summer value, resulting from reduced mixing ratios in the lowest 75% of the sounding (Figure 4.4c,d). A large range in mixing ratio values also exists below 5 km due to the potential for marine influences (e.g. afternoon sea breeze), primarily from test cases #1-4, impinging on these otherwise dry regions of the western United States. However, the observed range commonly falls below the mid-latitude summer values and suggests that uncertainty may be introduced in the sub-pixel retrieval, primarily from the increased 11 μm transmissivity.

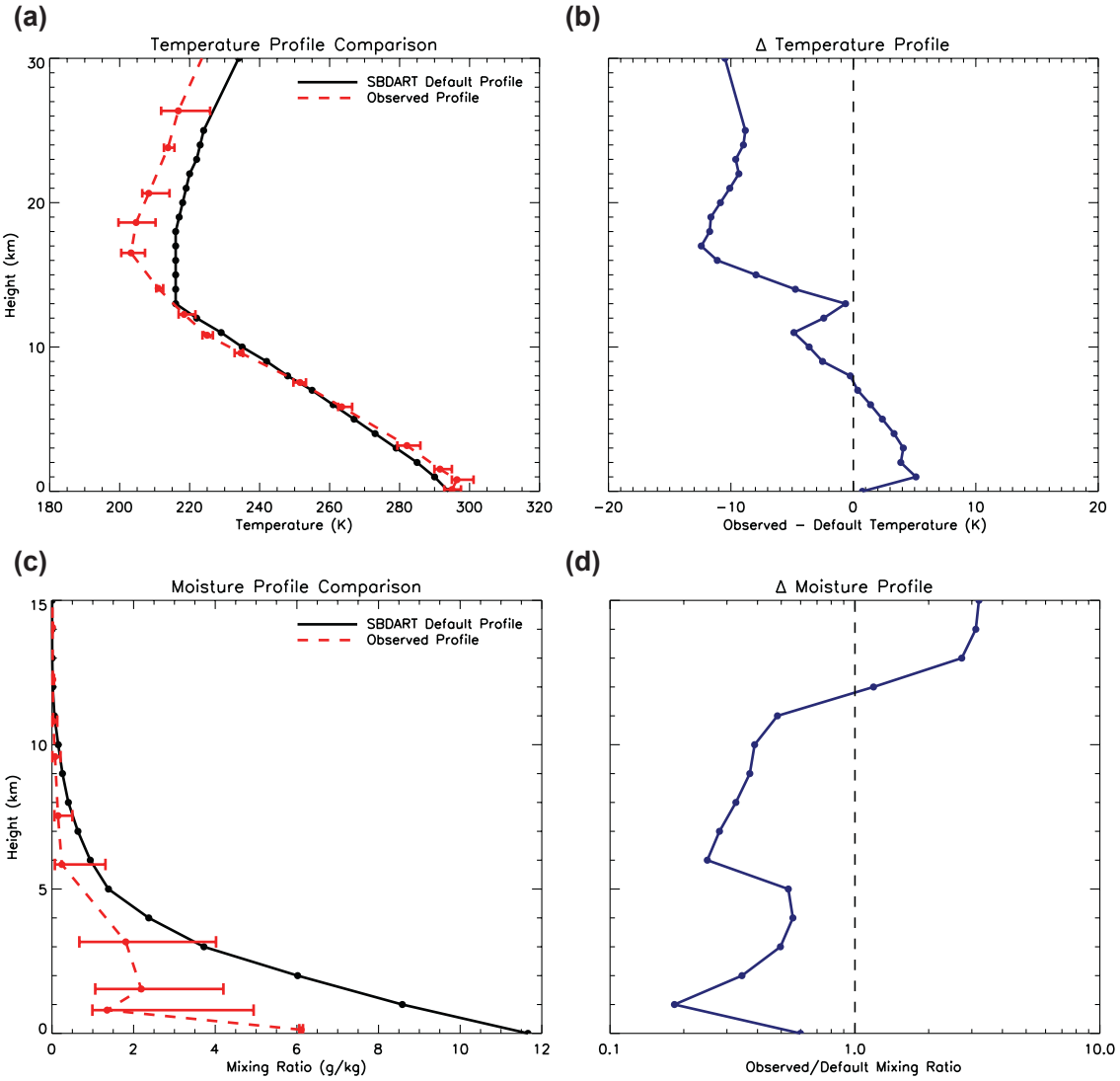

Figure 4.4: Atmospheric profile comparisons. (a) Comparison between the observed (dashed red) and the default mid-latitude summer (solid black) temperature profiles. Red error bars indicate the range of observed temperatures at each height AGL, with each red data point corresponding to the median. (b) The observed temperature profile (interpolated to match the height levels of the default mid-latitude summer profile) subtracted from the default profile (absolute change). (c) and (d) Same as (a) and (b), respectively, but for the moisture profiles (mixing ratio), with the relative change (observed/default) in mixing ratio used in (d).

4.2.2 Retrieval Uncertainty Associated with the Atmospheric Profile

While earlier studies on sub-pixel retrievals did incorporate an atmospheric correction (e.g. Giglio and Kendall, 2001; Zhukov et al., 2005, 2006), few, if any, of these studies show the effects originating from an improper assumption of the atmospheric profile. In this study, modified 4 and 11 μm lookup tables were produced using the observed temperature and water vapor profiles described in the previous section, allowing the theoretical relationships between the 4 and 11 μm pixel temperature to be examined for each atmospheric profile. Specific examples are presented in Figure 4.5a-d, corresponding to the sub-pixel retrieval's lookup table for a single fire pixel in test case #1 when the VZA = 14^o, SZA = 48^o, and RAZ = 165^o (same as Figure 2.2). As described in Chapter 2, each dashed curve represents the pixel temperatures at 4 and 11 μm that result from specified values of fire area fraction for varying fire temperatures. Each solid curve, on the other hand, represents the pixel temperatures that result from specified values of fire temperature for varying fire area fractions. From this display, it is immediately evident that the 4 μm channel is more sensitive to changes in fire temperature and the 11 μm channel is more sensitive to changes in fire area fraction. Therefore, drawing from the water vapor effects at 11 μm (Figure 4.3b,d), changes in the atmospheric profile are likely to have the largest impact on retrieved fire area because for the same fire area fraction and fire temperature, less water vapor will greatly increase the brightness temperature at 11 μm.

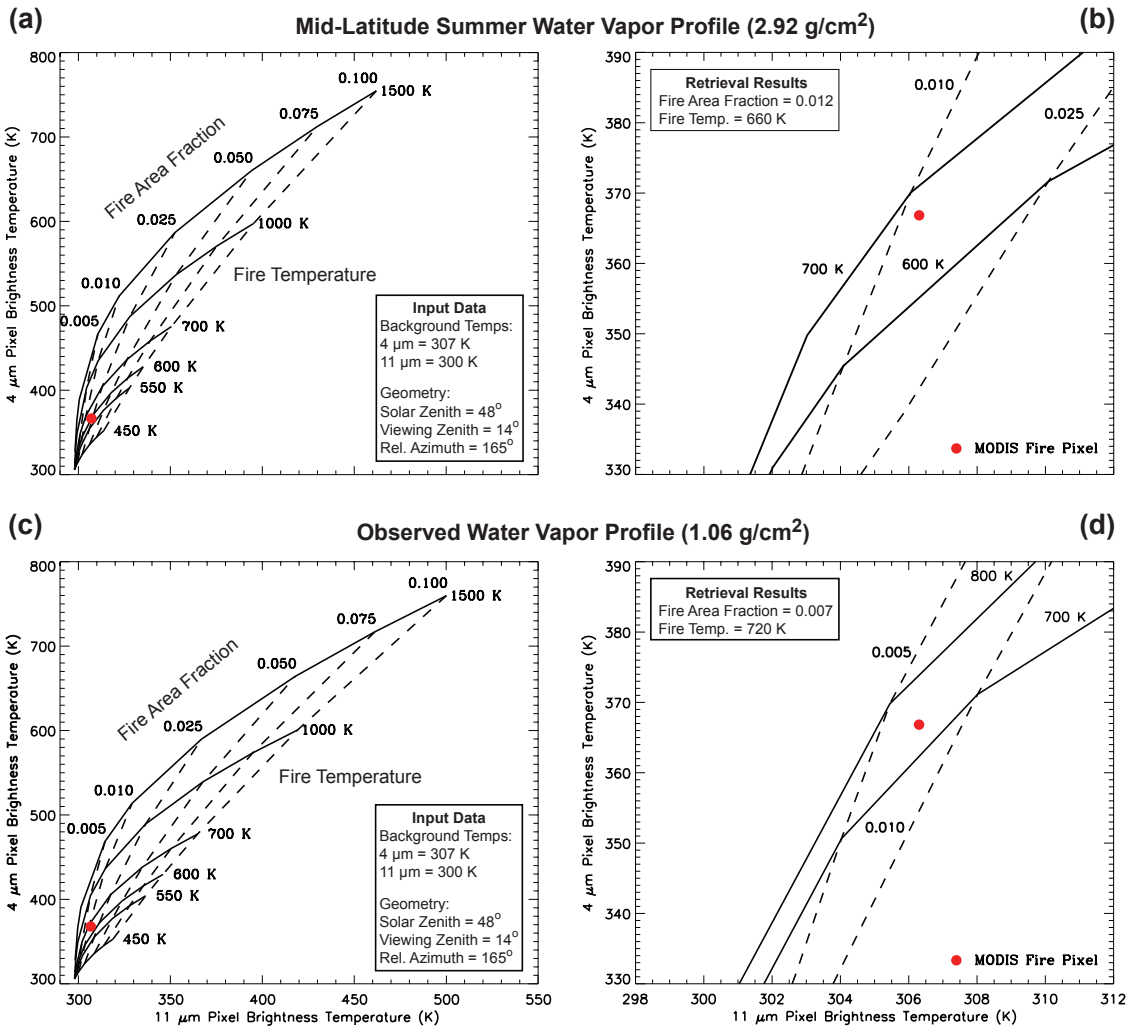

Figure 4.5: Theoretical relationships between the 4 and 11 μm pixel temperature for various values of fire temperature and fire area fraction when using the input data for California test case #1 (displayed in Figure 4.1). (a) and (c) respectively show the lookup tables needed for the sub-pixel retrieval using the climatologically based mid-latitude summer water vapor profile (2.92 g/cm^2) and the observed water vapor profile (1.06 g/cm^2). Each dashed curve represents the relationship between the 4 and 11 μm pixel brightness temperatures at specified values of fire area fraction for varying fire temperatures. Each solid curve represents the relationship between the 4 and 11 μm pixel brightness temperatures at specified values of fire temperature for varying fire area fractions. Zoomed views of the lower-left portion of (a) and (c) are respectively displayed in (b) and (d), and correspond to the location of the superimposed red dot, which indicates a sample fire pixel from California test case #1. The specific retrieval inputs and results are provided in the black boxes.

When comparing the retrieval that uses the mid-latitude summer atmospheric profile (Figure 4.5a), with the retrieval that is modified for the observed atmospheric profile (Figure 4.5c), the reduced column water vapor in the latter case renders a shift of the entire lookup table towards higher 11 μm brightness temperatures, with little change based on the 4 μm channel. Consequently, the primary impact on the retrieval is a reduction in fire area fraction (between Figure 4.5a and Figure 4.5c) for any given set of pixel temperatures. However, the retrieved fire temperature concurrently increases (to a lesser extent) due to the minimal atmospheric effects at 4 μm. The superimposed red dot displayed in Figure 4.5b,d (corresponding to the location in Figure 4.5a,c) represents the actual retrieval result using the residual-based method (described in Chapter 2) and highlights the effect caused by a change in the atmospheric profile. This sample fire pixel has an observed 4 μm pixel temperature of 366.8 K and 11 μm pixel temperature of 306.3 K, which produces a retrieved fire area fraction of 0.012 and a fire temperature of 660 K using the mid-latitude summer lookup tables. In contrast, the fire area fraction decreases to 0.007 and the fire temperature increases to 720 K when using the modified lookup tables.

Similar to Figure 4.5, the retrieved fire area for all 33 valid fire pixels (from test cases #1 to #6) is overestimated when using the mid-latitude summer atmospheric profile (red data points in Figure 4.6a) compared to the observed profile (blue data points in Figure 4.6a), with a mean difference of 69.1%. Figure 4.6a also shows that this overestimation is slightly larger for the fire pixels with large VZAs, which can be explained by the effect of longer path lengths (displayed in Figure 4.3c,d). Interestingly, the modified retrieval for the observed atmospheric profile does not improve the

correlation between the retrieved fire area and the AMS observations (R = 0.57) when compared to the counterparts from using the mid-latitude summer profile (R = 0.59, Table 4.1). In fact, the observed profile seems to result in retrieved fire areas that may even be too low compared to AMS, which likely stems from the low column water vapor amount value of 1.06 g/cm^2. Figure 4.3a-d shows that a column water vapor observation of less than ~1.5 g/cm^2 falls in the region where the BT_{TOA} changes rapidly for small changes in water vapor amount. Therefore, relatively small errors in the water vapor profile will result in a relatively large change in retrieved fire area.

Table 4.1: Statistics for the atmospheric effect on retrieved fire area and FRP.

Column Water Vapor Amount (g/cm^2)	**RMSE**	**R**	**R^2**
MODIS (Retrieved) vs. AMS (Observed) Fire Area (km^2)			
2.92 (Mid-Latitude Summer)	0.03	0.59	0.35
1.06 (Observed)	0.04	0.57	0.32
Sub-Pixel FRP_f vs. Current MODIS FRP_p (MW)			
2.92 (Mid-Latitude Summer)	77.57	0.93	0.86
1.06 (Observed)	31.5	0.98	0.96

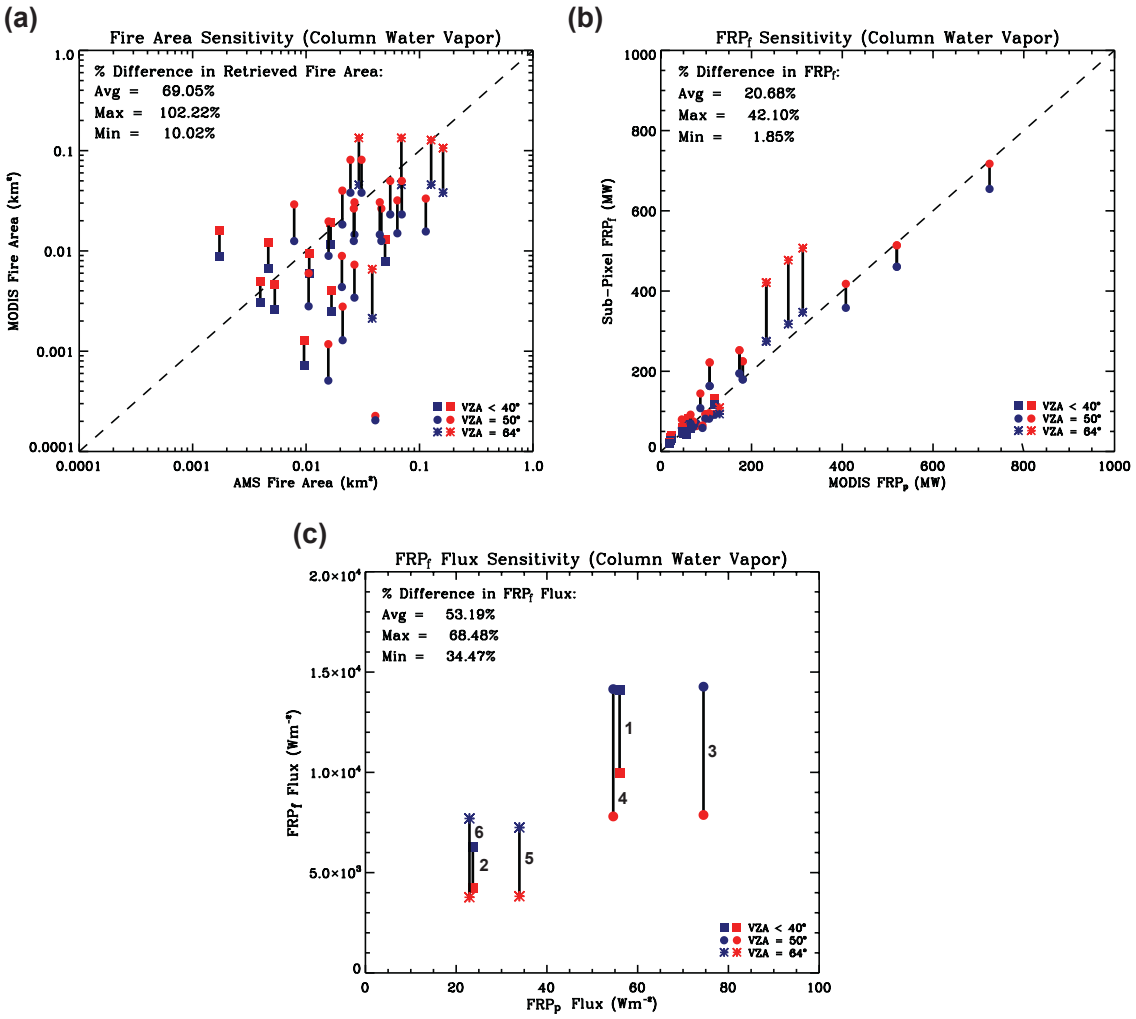

Figure 4.6: Retrieval sensitivity to atmospheric column water vapor amount. (a) Pixel-level comparisons between retrieved MODIS fire area and AMS observed fire area, with black error bars indicating the change in retrieved fire area using the mid-latitude summer (red symbols) and the observed (blue symbols) water vapor profiles. (b) and (c) Same as (a), but respectively for pixel-level comparisons between FRP_p and FRP_f, and cluster-level comparisons between FRP_p per cluster pixel area (FRP_p flux) and FRP_f per fire area (FRP_f flux) using the sum of pixel-level retrievals method. The California test case labels in (c) correspond to Figure 4.1. The plot symbol type in (a-c) indicates the viewing zenith angle of each pixel.

As a result of the offsetting changes in fire area fraction and temperature (Figure 4.5) from the observed profile, it can be expected that the effect on FRP_f (equation 1.2) will be relatively small in comparison to fire area. Figure 4.6b shows the current MODIS

FRP_p compared to the retrieved FRP_f when using the mid-latitude summer and observed atmospheric profiles, and the change in FRP_f is indeed small, with a mean of 20.7% and many pixels less than 10%. As with fire area, the largest differences occur with large VZAs, but also at high FRP values. In these cases, the surface fire temperature is likely larger, which would enhance the effect of an atmospheric correction based on Figures 4.2 and 4.3. The observed profile also increases the correlation between FRP_p and FRP_f ($R = 0.98$) and reduces the RMSE by 59.4% (Table 4.1). However, caution must be used when interpreting this result because FRP_p itself is based on a best-fit methodology with its own uncertainty (e.g. Kaufman et al., 1998a). Therefore, FRP_p should be considered as a base for comparison rather than a true, observed quantity (Chapter 3).

It is obvious that variations in the atmospheric profile have the largest impact on retrieved fire area (Figure 4.6), which is manifested in the calculation of FRP_f flux per total fire pixel cluster area (equation 3.2, using the sum of pixel-level retrievals method), where the mean difference is 53.2% (Figure 4.6c). Similar to Chapter 3, the cluster FRP_f flux, produced using both profiles, compares well to the FRP_p flux, but provides much more realistic values for the large fire events in the test cases. However, the results of this study show that the chosen atmospheric profile can have a noteworthy impact on the accuracy of the cluster FRP_f flux, especially when the atmospheric column water vapor amount is very low. This study only provides one such example and other locations with very low (or very high) column water vapor amounts, as well as regions with large seasonal temperature variations (e.g. winter fire events) may also require a modified

atmospheric profile. Therefore, if the retrieval is applied on a global-scale, a variety of atmospheric profiles will be included with the lookup table calculations.

4.3 Background Emissivity

Based on previous studies, the 4 and 11 μm background emissivities (e_{4b} and e_{11b} in equations 2.3 and 2.4) are assumed to be respectively equal to 0.95 and 0.97 (e.g. Giglio et al., 1999; Petitcolin and Vermote; 2002; Tang et al., 2009), which is true for relatively dense, green vegetation, such as the temperate evergreen forests used in this study. However, in broader spatial domains, it is very possible that the background emissivity in each fire detection channel (4 and 11 μm) may vary. Several studies (e.g. Giglio et al., 1999; Petitcolin and Vermote; 2002; Tang et al., 2009) show that the emissivities for dense, green vegetation, such as tropical rainforest, are commonly very close to 0.96 in both channels. In contrast, vegetated surfaces with a higher reflectivity, such as dry grassland, may result in a larger departure from 0.96 and may also result in a significant inter-channel difference. For example, Giglio et al. (1999) show that emissivities for dry savannah or dry temperate grasslands are about 0.86 and 0.92 at 4 and 11 μm, respectively.

In order to study how each region's background emissivity may affect the retrieval, the MODIS sub-pixel algorithm is run for each potential emissivity situation provided in the literature, ranging from 0.75 - 1.0 at 4 μm and 0.91 – 1.0 at 11 μm. For most pixels, the difference in retrieved fire area is between 6.2% and 25.3% with a mean of 11.3% (see Table 4.2 in Section 4.5), which corresponds to a change in fire area from

less than 100 m^2 to over 1000 m^2. In addition, the potential variability in retrieved fire area is independent of the size of the fire event (based on AMS observations, not shown). However, if the dry grass situations are removed, then the mean variability would decrease to 3.4% and most pixels would fall in the range of 1% to 7%.

The effect of background emissivity on FRP_f and FRP_f flux is also small, but in contrast to the atmospheric profile sensitivity, FRP_f is actually the most sensitive output variable (Figure 4.7) due to the larger range of potential emissivity values associated with the 4 μm channel. As shown in Figure 4.5, the 4 μm channel is highly sensitive to changes in retrieved fire temperature, hence this duel channel emissivity simulation affects FRP_f slightly more than retrieved fire area, with a mean variability of 19.2%. Figure 4.7 shows that this variability increases with increasing FRP_f, which is largely independent of the observed VZA. However, as with retrieved fire area, the sensitivity of FRP_f to background emissivity becomes almost negligible if the dry, brown vegetation scenarios are removed. Therefore, with the six test cases located in regions that are dominated by forest (Figure 4.1), it is very likely that the assumed emissivity values (0.95 at 4 μm and 0.97 at 11 μm) will not result in large retrieval errors. In fact, regions that are completely dominated by dry, brown vegetation are the only situation where the emissivity impact would become significant. In these cases, emissivity or normalized difference vegetation index (NDVI) data from MODIS (or other sources) could be incorporated as a direct input variable, which may prove valuable if the sub-pixel algorithm is implemented on a global-scale.

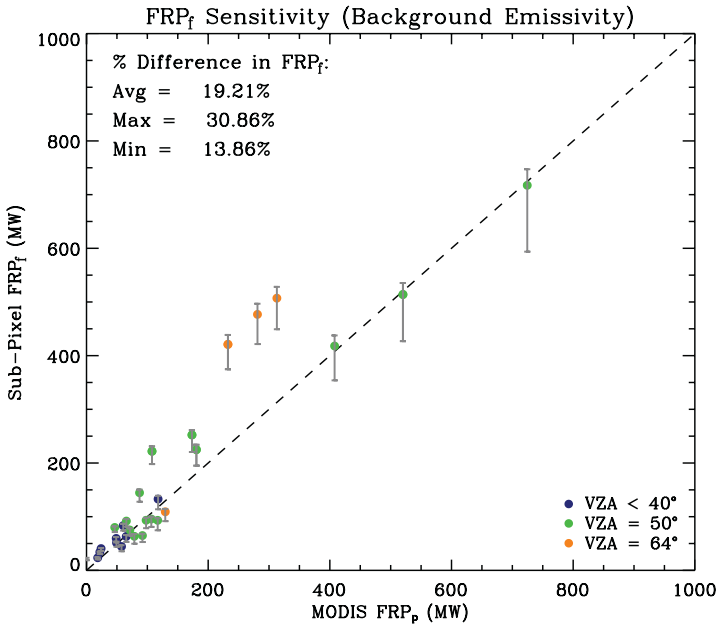

Figure 4.7: Pixel-level comparisons between FRP_p (MODIS pixel-based FRP) and FRP_f (sub-pixel-based FRP). Grey error bars are used to indicate sensitivity to background emissivity selection for several green and brown vegetation scenarios, with the color scheme indicating the viewing zenith angle.

4.4 Background Temperature

For any sub-pixel calculation, the background TOA brightness temperature (BT_b) is defined as the non-burning portion of the pixel (e.g. Dozier 1981), but this value is not currently obtainable using MODIS data for that pixel. Therefore, the MODIS fire detection algorithm approximates the BT_b via a neighborhood search within a square window that progressively widens as necessary around a potential fire pixel until at least 25% of the pixels in the square are valid background pixels (absence of fire) and the number of these valid pixels is at least eight (Kaufman et al., 1998a; Giglio et al., 2003). Not surprisingly, this method may result in a large difference between the in-pixel BT_b and the MODIS approximation (BT_{bm}), especially with large VZAs.

4.4.1 Mischaracterization of the MODIS 11 μm Background Temperature

The bi-spectral approach in the MODIS sub-pixel algorithm requires an accurate estimation of both the 4 and 11 μm BT_{bm} (Chapter 2). While the MODIS fire detection algorithm uses the same fire-free pixels to compute the BT_{bm} for the 4 and 11 μm channels (Justice et al., 2002; Giglio et al., 2003), few, if any, subsequent calculations (e.g. FRP_p) require the use of the 11 μm BT_{bm}, thus any errors at 11 μm may have gone unnoticed or have been disregarded. For example, 3 out of the 37 MODIS fire pixels used in the test cases have a pixel brightness temperature that is less than the BT_{bm} at 11 μm, while the 4 μm brightness temperatures display no such mischaracterization (Figure 4.8). The three pixels with an error also occur during the daytime, which may increase the background noise due to unequal heating of the surface. Regardless, any such error produces a major limiting factor on the retrieval because sub-pixel calculations are not possible for any of these pixels, unless an improved background characterization technique is developed. Zhukov et al. (2006) described a similar issue with the BIRD small satellite mission (operational from 2001-2004), but the spectral properties, pixel resolution, and background temperature methodology were significantly different from the MODIS sensor.

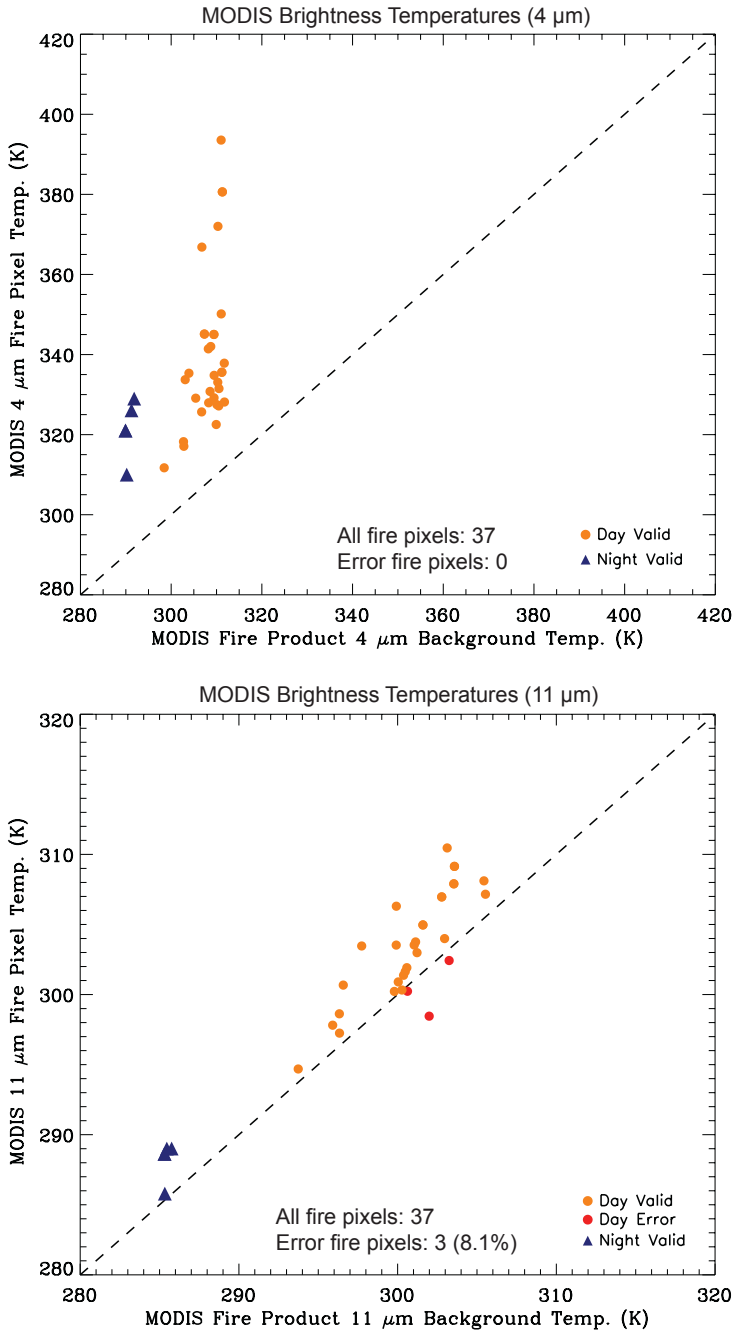

Figure 4.8: Scatterplots showing the pixel and background brightness temperatures at 4 µm (top) and 11 µm (bottom) for each MODIS fire pixel from the California test cases. Day and night observations are displayed as dots and triangles, respectively. The color scheme indicates whether each day or night pixel is valid or has a background temperature mischaracterization error.

As described in Section 4.2, the MODIS 11 μm channel is much more sensitive to the relative change of cooler temperatures than the 4 μm channel, suggesting that the BT_{bm} mischaracterization observed in the three MODIS fire pixels is most likely to occur when the sub-pixel fire area is very small (Zhukov et al., 2006). Therefore, to create a spatial perspective on the sub-pixel fire properties of these pixels, the AMS data are incorporated (Figure 4.9a-c) and show that all three fire pixels actually contain fairly large sub-pixel fire area fractions (~0.01). However, two of the pixels (Figure 4.9a,b) contain very diffuse fire hot spots and the remaining pixel (Figure 4.9c) contains pixel edge hot spots, which can greatly reduce the mean fire pixel temperature due to point spread function effects (described in Chapter 3; Calle et al., 2009). Furthermore, the 11 μm AMS data (free from saturation) can be averaged to provide a general representation of the sub-pixel fire brightness temperature (FT_{AMS}), which will be considerably lower than at 4 μm due to the reduced sensitivity to higher temperatures, but will still be the warmest portion of the pixel. This analysis shows that the three MODIS fire pixels displayed in Figure 4.9a-c have a mean 11 μm FT_{AMS} less than 430 K, which is low in comparison to highly concentrated sub-pixel fire fronts that can produce mean 11 μm FT_{AMS} greater than 460 K (described in Chapter 3). Therefore, the observed combination of diffuse or pixel edge hot spots, at relatively low FT_{AMS} values, likely reduces the mean MODIS 11 μm fire pixel brightness temperature to the point where it cannot be distinguished from general background noise.

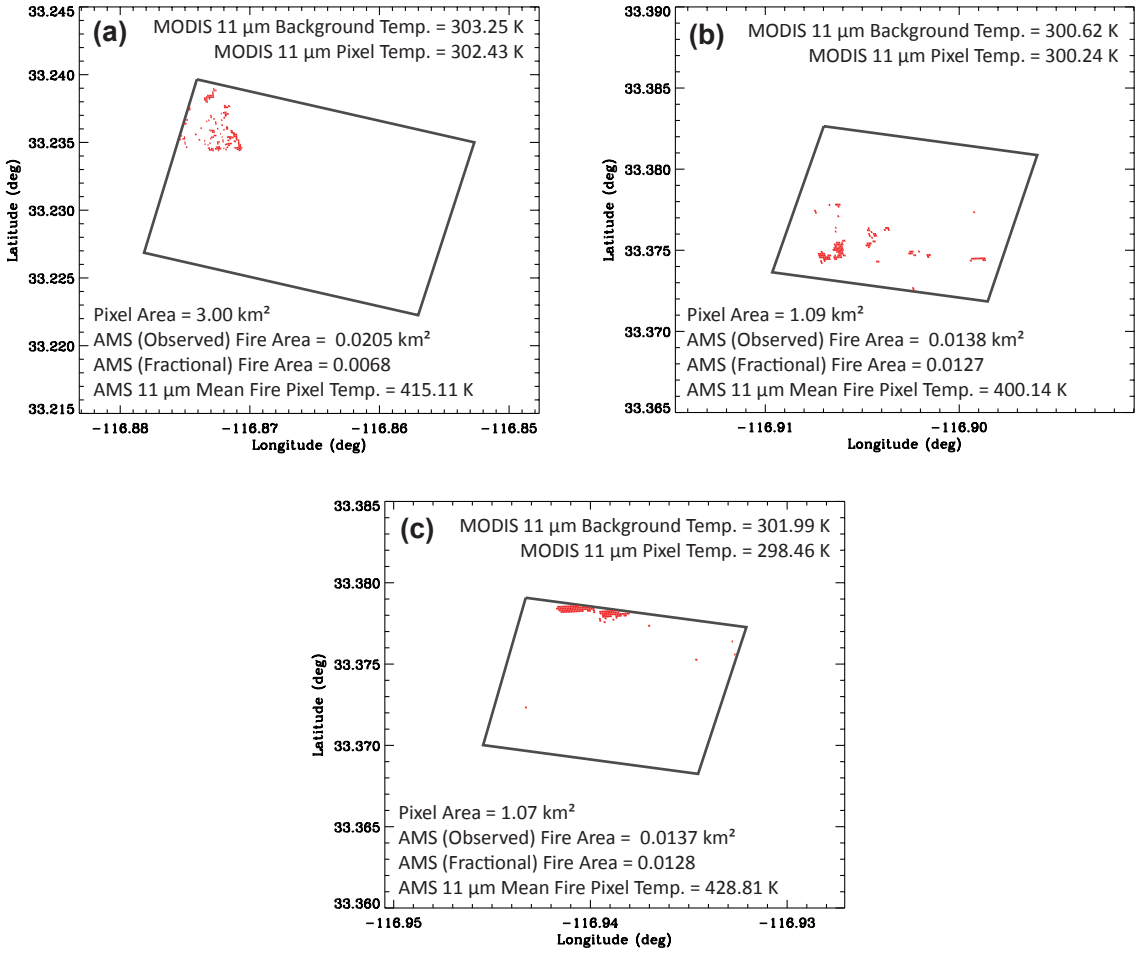

Figure 4.9: Spatial displays of the AMS-derived fire locations (red shading) within the three MODIS fire pixels (a-c) that have a brightness temperature less than the background. Black polygons indicate the boundaries of each MODIS fire pixel.

At 11 µm, background noise can result from large burn scars, smoldering regions, or a relatively warm, heterogeneous location (Schroeder et al., 2010). Additional variations in BT_{bm} may result from changes in land cover (e.g. forest to exposed rock), topography, and aspect. As shown in Figure 4.1, the test cases used in this analysis are in fairly mountainous terrain in California, a situation that may produce variations in BT_{bm}

from high to low elevations and from slopes that face the sun (south slopes) versus slopes that face away from the sun (north), as well as vegetated to non-vegetated regions. Figure 4.10a,b highlights the 11 μm background noise surrounding the three pixels with an 11 μm mischaracterization using the MODIS and high-resolution AMS data. While there is an offset of about 5 K between sensors (produced from differences in altitude and scan method), both scans (Figure 4.10a,b) show how complex topography and changes in aspect create variations in 11 μm temperature of more than 10 K over very short distances in these daytime scenes. It is also evident that all three non-valid fire pixels (white shading in Figure 4.10) are located in a relatively cool region of the scan with much warmer regions in the immediate vicinity. Therefore, depending on how wide the MODIS background pixel window becomes, the resulting mean 11 μm BT_{bm} has the potential to be warmer than the fire pixel temperature, especially since as many as 21 valid (non-fire) background pixels may be included (e.g. Kaufman et al., 1998a; Giglio et al., 2003). With the pixel-level retrieval rendered impossible, these background temperature errors will affect the FRP_f and effectively reduce the retrieved fire area in the corresponding fire pixel cluster, thus a quality control flag is currently being considered.

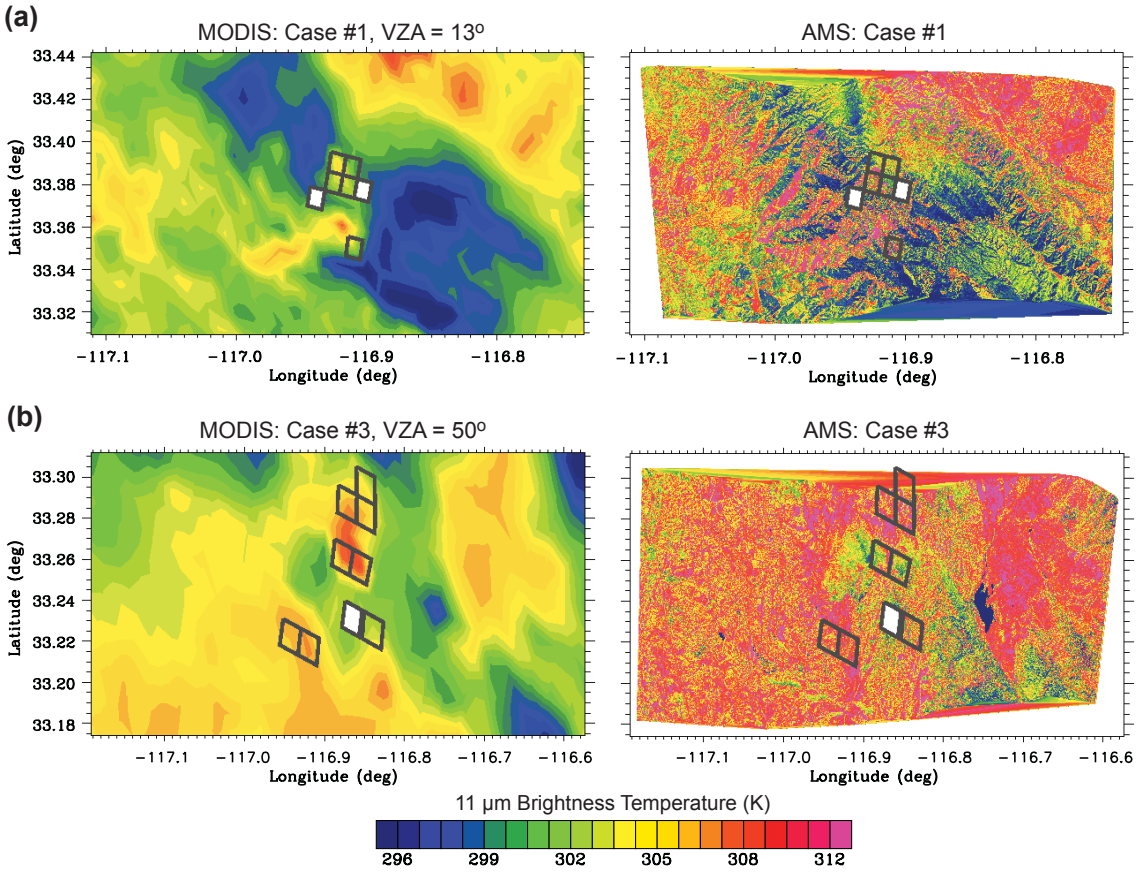

Figure 4.10: Maps showing the 11 µm brightness temperature for MODIS (left) and AMS (right) using California test case #1 (a) and case #3 (b). Black polygons indicate the boundaries of MODIS fire pixels and a white-filled polygon indicates a MODIS fire pixel with a brightness temperature that is less than the background.

4.4.2 Retrieval Uncertainty Associated with Background Temperature

While MODIS is limited to a background window approximation, the AMS data allow the true in-pixel background brightness temperature (BT_{bp}) to be calculated based on the distribution of AMS pixel temperatures at 4 and 11 µm within the MODIS pixel footprint (Chapter 3). Figure 4.11a,b shows that the BT_{bp} and BT_{bm} are strongly correlated ($R_{4\ \mu m} = 0.88$ and $R_{11\ \mu m} = 0.92$), but for many pixels, the BT_{bm} is cooler than the BT_{bp}, which may result from differences in sensor characteristics. For the daytime test cases, these deviations are reduced at the smallest VZAs (blue data points),

suggesting that off-nadir pixel growth may influence the background temperature noise. However, there is paucity of available data and the test cases with the largest VZAs (64^{o}) occur at night with no solar impact, which may explain the stronger agreement between BT_{bp} and BT_{bm} in the largest VZA cases (orange data points). Even still, Figure 4.11a,b shows that there can be a considerable difference between the MODIS fire product and the AMS-derived in-pixel background brightness temperatures.

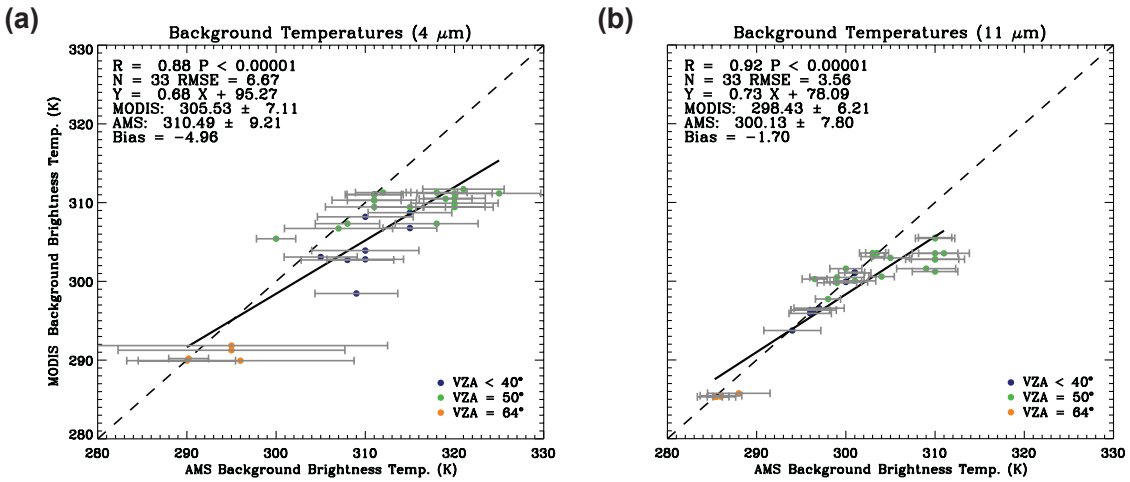

Figure 4.11: Comparisons between the MODIS fire product BT_{bm} and the AMS derived in-pixel BT_{bp} at 4 μm (a) and 11 μm (b). The color scheme indicates the MODIS viewing zenith angle (distance from nadir). Grey error bars indicate ±1.0 standard deviation of all AMS data points considered for the calculation of the BT_{bp}.

The incorporation of AMS data also allows the variability (±1.0 standard deviation) of the BT_{bp} region (e.g. not flaming or smoldering) to be visualized (grey error bars in Figure 4.11a,b). From this illustration, it is clear that the 4 μm BT_{bp} region contains a larger range in temperature (~10 K) than at 11 μm (~ 5 K), suggesting that solar reflectivity may play a role. In general, the variability of the BT_{bp} increases as the VZA (pixel size) increases. However, the MODIS fire pixels at the largest VZAs are

nighttime test cases where the temperature variability in the background region of the pixel should be reduced. At 4 μm (and to a lesser extent at 11 μm), many of these nighttime, large VZA pixels have the largest variability in the BT_{bp}. In these cases, the large size of the background region may outweigh the effect of nighttime observation by allowing a wider variety of surface features, such as valleys and ridges (complex topography), to be contained within the boundaries of the MODIS fire pixel, greatly affecting the sub-pixel temperature distribution, even at night. Therefore, Figure 4.11a,b also highlights the complexities in obtaining an accurate background temperature in a heterogeneous environment, where relatively large variations can occur even within the boundaries of an individual MODIS fire pixel.

The impacts from these background brightness temperature errors on the sub-pixel results are drastically different between the 4 and 11 μm channels. Based on Figure 4.11a, it is possible to observe a 4 μm BT_{bp} error of 5 to 10 K. However, an error of 5 K produces a relatively small change in retrieved fire area, averaging ~23.0% (Figure 4.12a). The effect on FRP_f and the cluster FRP_f flux is also small, with mean changes of 13.8% and 20.8%, respectively (see Table 4.2 in Section 4.5). The error bars in Figure 4.12a display the resulting fire area variability on a per pixel basis, produced by running the sub-pixel retrieval with deviations of ±1.0 K from the observed BT_{bm} up to a maximum deviation of ±5.0 K. A closer examination reveals that the resulting change in retrieved fire area is very small for large fires with a high FRP_f (~4 %) and larger for smaller fires with lower FRP_f values (40 - 50%). This discrepancy can be explained by fires with a high FRP_f coinciding with a much larger difference between the flaming and

the background regions than with low FRP_f fires. Therefore, high FRP_f fires are not as susceptible to BT_{bm} errors as low FRP_f fires.

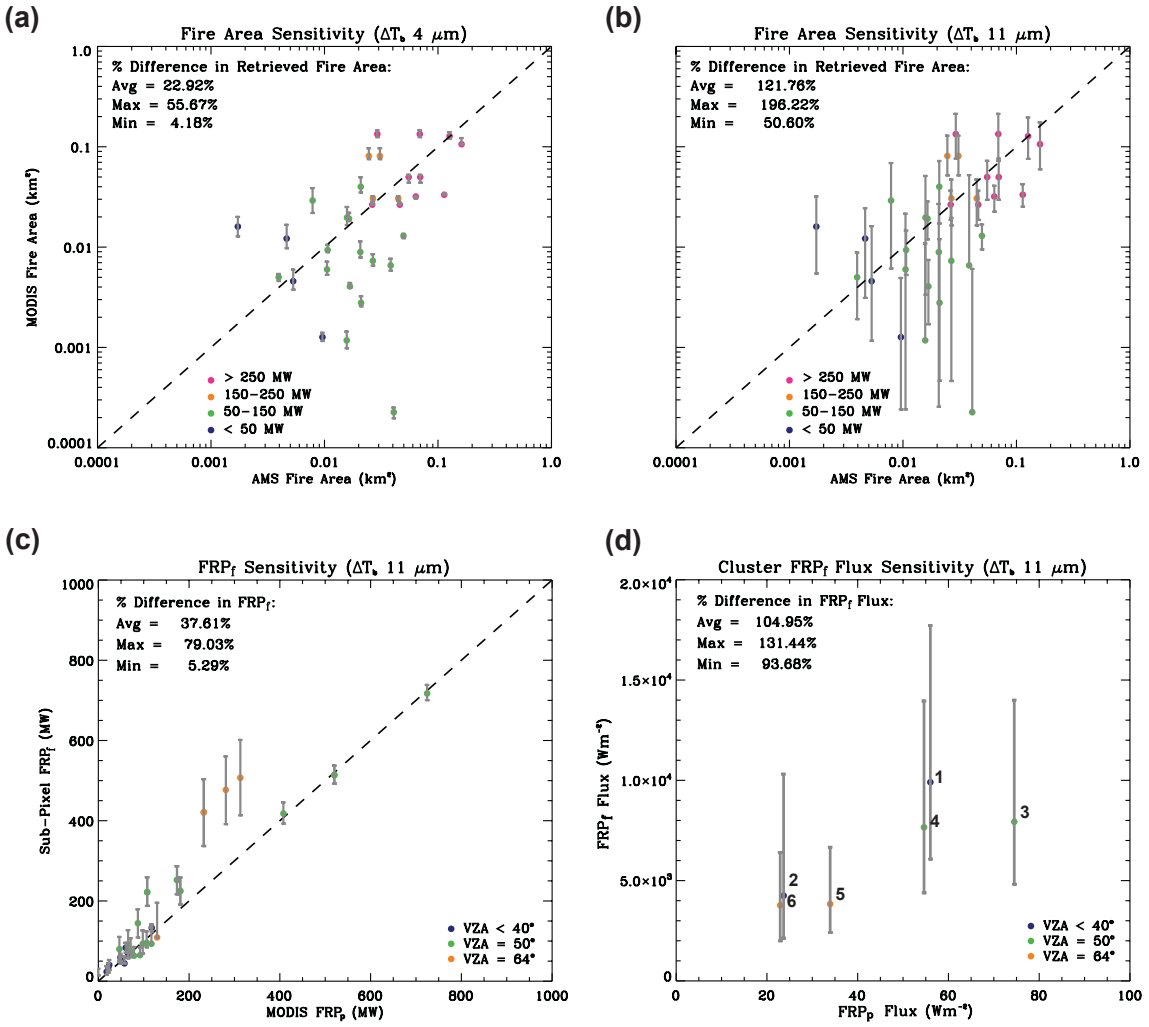

Figure 4.12: Retrieval sensitivity to background brightness temperature. (a) and (b) Pixel-level comparisons between retrieved MODIS fire area and AMS observed fire area from the six California test cases. Grey error bars indicate the sensitivity of the retrieval to a ±5.0 K error in the 4 μm BT_{bm} and a ±1.0 K error in the 11 μm BT_{bm}, respectively. The color scheme indicates the FRP_f value for each pixel. (c) Same as (a) and (b), but for pixel-level comparisons between MODIS FRP_p and the sub-pixel FRP_f. (d) cluster-level comparisons between FRP_p per cluster pixel area (FRP_p flux) and FRP_f per fire area (FRP_f flux) using the sum of pixel-level retrievals method. The test case labels correspond to Figure 4.1. The color scheme in (c) and (d) indicates the MODIS viewing zenith angle.

At 11 μm (Figure 4.12b), the error bars were produced by running the sub-pixel retrieval with deviations of ±0.5 K from the observed BT_{bm} up to a maximum deviation of ±1.0 K, provided that the BT_{bm} was cooler than the fire pixel brightness temperature. In this case, the small 1.0 K error in 11 μm BT_{bm} produces in an enormous change in retrieved fire area, occasionally reaching an order of magnitude or more. As with 4 μm, smaller fires with low FRP_f are affected more than larger fires with a high FRP_f, but the smallest change in retrieved fire area is still at least 50%. The incomplete error bars in Figure 4.12b show that this simulation of a small BT_{bm} error still resulted in several pixels that reached the mischaracterization threshold described in the previous section, where the retrieval was rendered impossible because the BT_{bm} became warmer than the pixel brightness temperature. Not surprisingly, the large errors observed in Figure 4.12b also produce large deviations in FRP_f, which increase with large VZAs (Figure 4.12c). Similarly, the variability in FRP_f, along with the large effect on retrieved fire area, greatly influences the cluster FRP_f flux values, which change by more than 90% for all six fire clusters (Figure 4.12d). However, this variability of FRP_f flux (at both 4 and 11 μm) is based solely on the highly sensitive fire area component. Therefore, Figure 4.12d represents a worst-case scenario for an error of ±1.0 K, and any variations in FRP_f (shown in Figure 4.12c) may mitigate the FRP_f flux sensitivity.

4.5 Summary

The previous three sections clearly show that several potential direct sources of error in the sub-pixel retrieval (summarized in Table 4.2), such as the atmospheric profile

and background emissivity assumptions, are contained within the large uncertainty range of small (±1.0 K) errors in the 11 μm BT_{bm}. Furthermore, the BT_{bp} displayed in Figure 4.11b shows that variations in the 11 μm BT_{bm} may occasionally reach up to 5 K, greatly increasing the uncertainty displayed in Figure 4.12b. The sensitivity analysis of Giglio and Kendall (2001) showed a similar results, where the retrieved fire area was roughly 10 times more sensitive to errors in the 11 μm background brightness temperature than at 4 μm. Therefore, this analysis confirms the results of previous studies (e.g. Giglio and Kendall, 2001; Zhukov et al., 2006), and suggests that the 11 μm BT_{bm} is the primary factor limiting the accuracy of sub-pixel calculations, especially for small fires with a low FRP_f.

The results from this study suggest that the atmospheric profile assumption is the second principle source of error (Table 4.2), and will overestimate retrieved fire area for fire pixels observed in regions of low column water vapor amount, when using the current methodology. However, incorporating multiple profiles into the retrieval process and matching the observed column water vapor amount to the closest atmospheric profile can easily alleviate this problem. Therefore, the BT_{bm} selection methodology is the primary focus for improvement, especially for future satellite missions, such as NPP VIIRS and GOES-R. Currently, BT_{bm} selection is heavily weighted on the 4 μm channel to ensure the region is free of smoldering or recently burned pixels (Giglio et al., 2003), but a correction for noise caused by variations in surface features is also required, especially at 11 μm. Any future 11 μm background brightness temperature selection methodology will likely require the incorporation of topography, land cover, and aspect

data sets. The background region could then be defined as nearby pixels that are not only free of fire, but also have similar characteristics as the fire pixel under scrutiny.

Table 4.2: Sensitivity summary for the MODIS sub-pixel retrieval.

Variable	% Change in Variable		
33 MODIS Fire Pixels	**Min.**	**Max.**	**Mean**
Atmospheric Profile (Mid-Latitude Summer vs. Observed)			
Retrieved Fire Area	10.02	102.22	69.05
FRP_f	1.85	42.1	20.68
Cluster FRP_f Flux	34.47	68.48	53.19
Background Emissivity (0.75 - 1.00)			
Retrieved Fire Area	6.22	25.27	11.29
FRP_f	13.86	30.86	19.21
Cluster FRP_f Flux[1]	10.9	16.43	9.06
4 μm Background Temperature (± 5.0 K from Observation)			
Retrieved Fire Area	4.18	55.67	22.92
FRP_f	2.92	43.03	13.71
Cluster FRP_f Flux[1]	14.09	36.56	20.78
11 μm Background Temperature (± 1.0 K from Observation)[2]			
Retrieved Fire Area	50.6	196.22	121.96
FRP_f	5.29	79.03	37.61
Cluster FRP_f Flux[1]	93.68	131.44	104.95

[1] FRP_f flux sensitivity is based on the sensitivity to retrieved fire area.
[2] Background temperatures are not allowed to increase above the pixel temperature.

The results in Table 4.2 show that fire area is typically the most sensitive retrieved parameter to errors in the direct input variables, while FRP_f is much less susceptible, due to offsetting effects from fire area fraction and temperature. Chapter 3 also showed that FRP_f is strongly correlated to FRP_p. The combination of this result, and the reduced sensitivity, suggests that FRP_f, by itself, can be used as an alternative

methodology to the current MODIS FRP_p. However, the primary reason for choosing the sub-pixel based method is that it also allows the radiant energy released over the area of the fire to be quantified via the FRP_f flux, which may be useful for future fire weather and smoke modeling studies. FRP_f flux is also the second most sensitive parameter in the retrieval; hence it is desirable to investigate its relationship to key meteorological variables affecting smoke production, such as wind speed, over a broad spatiotemporal domain with known variations in column water vapor amount and background emissivity. Similarly, the total number and spatial distribution of fire pixels with an 11 μm background temperature error (described in Section 4.4.1) must also be investigated in greater detail. To accomplish these goals, the sub-pixel retrieval is applied to a recent independent case study, explained in the following chapter.

Chapter 5. Case Study of Texas and Oklahoma Wildfires

5.1 Introduction

To complete algorithm development and sensitivity analysis described in Chapters 2, 3, and 4, this chapter applies an operational version of the MODIS sub-pixel algorithm to an independent, large wildfire event, occurring between 4 September 2011 (00:00 Z) and 8 September 2011 (23:59 Z). This case study allows the overall performance, limitations, and utility of the retrieval to be explored in great detail, and also allows the spatiotemporal distribution of background temperature errors to be easily explored. The overall study region, located within the United States and Mexico, is bounded by a range of 25 - 37 north latitude and 93 - 107 west longitude (Figure 5.1), but the primary focus is on the states of Texas and Oklahoma.

Several months of persistent upper-level ridging, with 500 hPa heights averaging 5 – 20 meters above the 1981-2010 climatology (contours in Figure 5.1), resulted in extreme drought conditions over the majority of the study region. The five days of this case study were also marked by low relative humidity values and stronger than average surface winds, following the passage of a surface cold front. Not surprisingly, 890 MODIS fire pixels were observed (via Aqua and Terra) within the study region during the temporal window of this study (red and greed dots in Figure 5.1), with the vast majority observed in northeastern Texas and southeastern Oklahoma. This region is an ideal location for testing the sub-pixel retrieval due to the combination of uniform, post-frontal weather conditions and relatively homogeneous biomass and terrain. Along with comparisons to the previously described California test cases, this Chapter will also

examine the potential utility of FRP_f flux for the characterization of fire weather, which is another method for assessing the retrieval's performance.

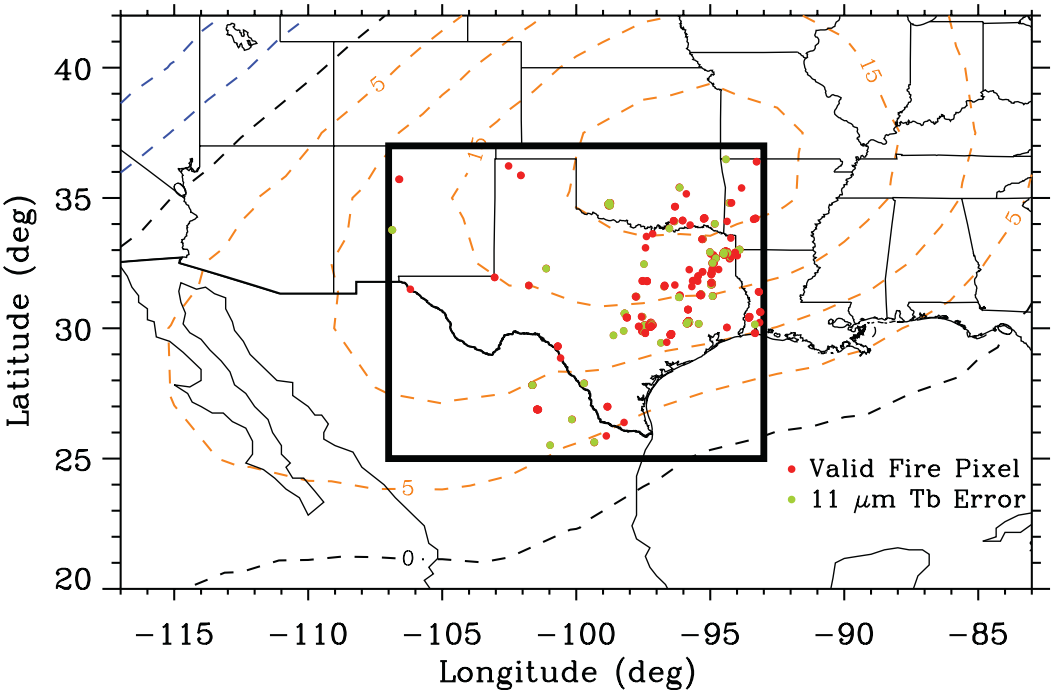

Figure 5.1: Map of the case study region, as denoted by the black box. The MODIS fire pixels observed between 4-8 September 2011 are displayed as dots, with red indicating valid pixels and green indicating an error in the 11 μm background temperature. Dashed contours indicate the mean 500 hPa height anomalies (based the 1981-2010 climatology) during the preceding three months (June, July, and August), with red and blue respectively indicating positive and negative anomalies.

5.2 Comparisons to the California Test Cases

For this application, level-2, Collection 5 MODIS column water vapor data (MOD05_L2/MYD05_L2, http://ladsweb.nascom.nasa.gov/data/search.html, King et al., 2003) were saved along with the retrieval output for each fire pixel, and show that the average atmospheric column water vapor amount (per pixel) over the five days was 2.09 g/cm^2. This value is closer to the mid-latitude summer column water vapor amount of 2.92 g/cm^2 than the California test cases (described in Chapters 3 and 4). However, a large range of 0.60 to 6.74 g/cm^2 was also observed, which is produced by the study domain stretching from desert regions to the Gulf of Mexico. The majority of the fire pixels are located in northeastern Texas, where the column water vapor amount likely falls much closer to the mean, suggesting that any resulting retrieval errors will be minor, especially compared to the test cases (e.g. Figure 4.7). The few fire pixels in the western portion of the study region have column water vapor contents that are much closer to the California test cases (e.g. < 1.0 g/cm^2), and thus will suffer from an overestimation in retrieved fire area. However, specific pixel-level validations of retrieved fire area, via AMS (or any other method), were not possible. A detailed examination of the background emissivity was also not considered due to the minimal sensitivity effect shown earlier (Table 4.2), but the extreme drought likely resulted in regions of brown vegetation that may produce a minor effect on the retrieval output.

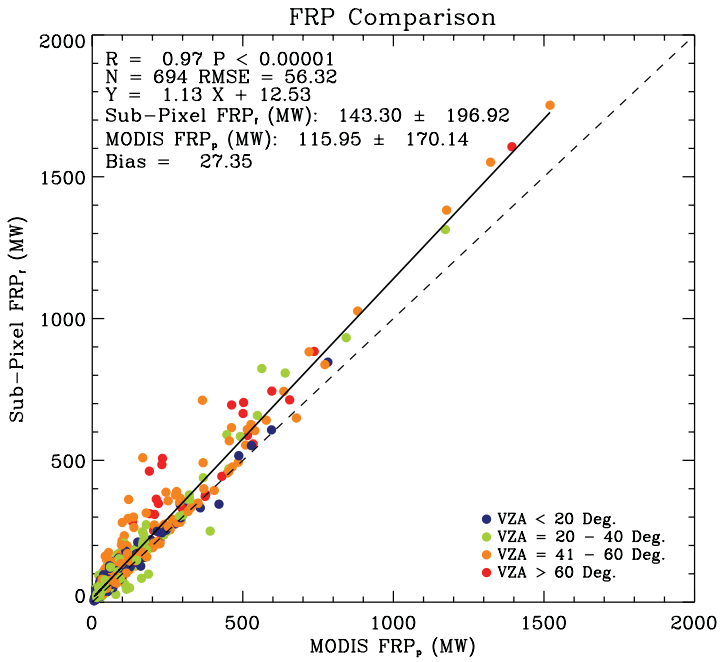

Figure 5.2: Pixel-level comparisons between FRP_p (current MODIS pixel-based FRP) and FRP_f (sub-pixel-based FRP) for the case study region displayed in Figure 5.1. The solid line corresponds to the linear fit equation and the color scheme is based on the viewing zenith angle (distance from nadir).

Similar to the results from the California test cases (Chapter 3), the retrieved FRP_f in the study region is strongly correlated (R = 0.97) to the current MODIS FRP_p for the valid individual fire pixels (Figure 5.2). However, this case study exposed a secondary limitation of the retrieval, where 39 fire pixels (not considered in Figure 5.2 or the statistics above) had retrieved fire temperatures of 1500 K - the maximum value currently considered in the sub-pixel retrieval based on earlier studies (Giglio and Kendall, 2001; Zhukov et al., 2006). Many of these pixels have an FRP_f that compares nicely to the FRP_p, but 11 pixels have an FRP_f that is unrealistically high. One explanation is that retrieval limit of 1500 K may be too low, which is evidenced by the questionable pixels corresponding to larger differences between the 11 μm pixel and background

temperatures (4-8 K) compared to the remainder of the 1500 K pixels (< 2 K). Similarly, Zhukov et al. (2006) allowed the retrieved fire temperature to increase above 1500 K if the 11 μm (TIR) pixel brightness temperature was greater than the background temperature plus four standard deviations of the surrounding background noise. However, for this case study, it is generally observed that many of the 1500 K fire temperatures correspond to very low FRP_p values (< 140 MW), reduced MODIS confidence levels, and small retrieved fire area fractions (< 0.001). Therefore, these are likely small fires, such as a fire front in a grassland or pasture (Figure 5.3, Smith et al., 2005; Mell et al., 2007; Stephens et al., 2008), which are also situations that greatly increase the uncertainty in the retrieval output (e.g. Giglio and Kendall, 2001; Peterson et al., 2012a). As a result, the retrieved fire temperature of 1500 K may simply be an artifact of an underestimated 11 μm background temperature that produces an improper fit (artificially large difference between fire and background) in the observed radiances during the retrieval calculations (described in Chapter 2). These pixels are currently flagged as invalid in the operational version of the algorithm.

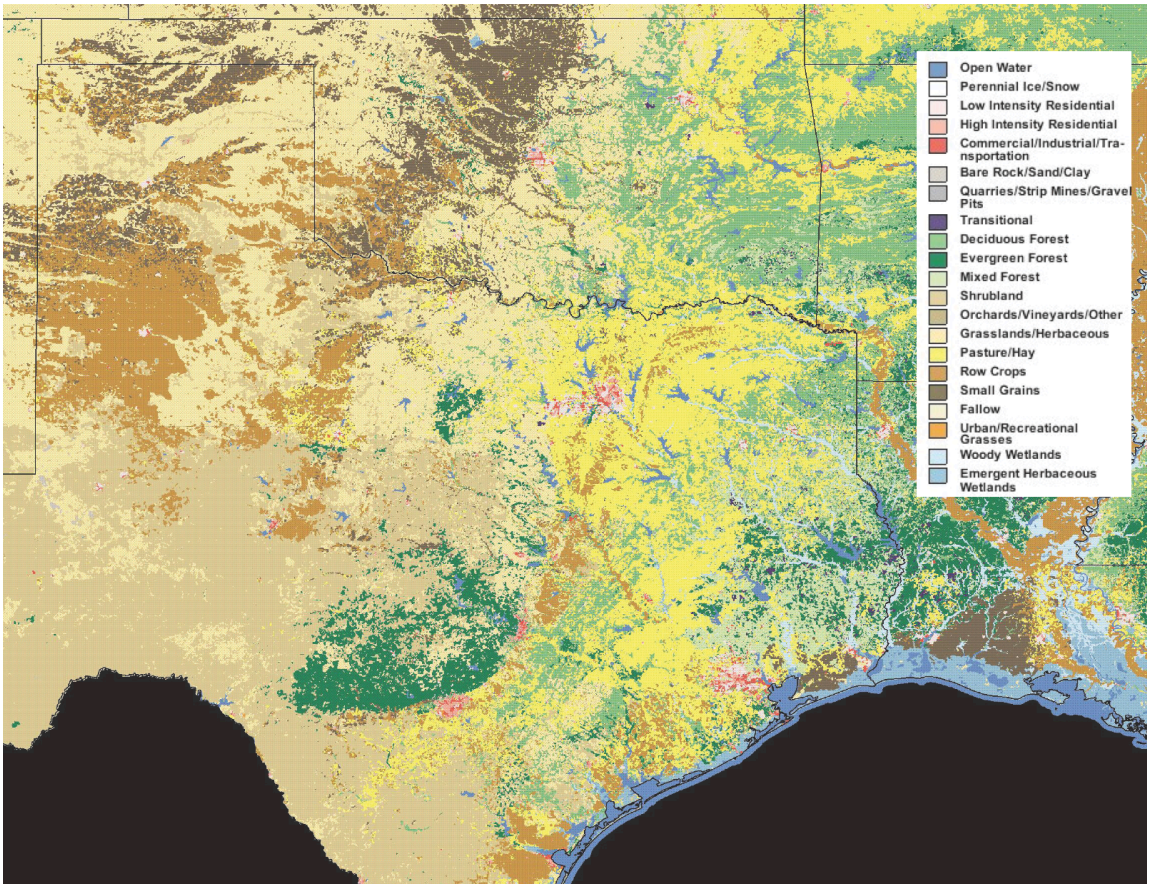

Figure 5.3: Landcover map for Texas and Oklahoma (http://gisdata.usgs.gov/).

The 11 µm BT_{bm} mischaracterization errors, highlighted in the California test cases (background warmer than the fire pixel), are also present in this case study, denoted by the green dots in Figure 5.1. Specifically, 157 (17.6%) of the 890 MODIS fire pixels have this BT_{bm} error, but seem to be randomly distributed within the study region, suggesting there is little spatial dependence on background noise. The vast majority of these errors, including the largest magnitudes, occur with daytime pixels (Figure 5.4, Table 5.1), where 26.4% of the pixels have an error. The case study domain has minimal topographic influences compared to the California test cases, suggesting that the 11 µm BT_{bm} errors in eastern Texas and Oklahoma likely stem from variations in local land

cover (Figure 5.3), which may include forest (deciduous/evergreen), cropland, pasture land, and urban or other non-vegetated regions. The major drought may also have created localized cases of brown or de-vegetated regions (presumably not irrigated) that are located nearby green, irrigated regions, which will have a considerably lower 11 μm BT_{bm} than the dry regions. Therefore, similar to the California test cases, daytime background noise at 11 μm is the key factor limiting the sub-pixel retrieval in this case study, further supporting the need for an improved BT_{bm} selection methodology. In stark contrast, the 4 μm background brightness temperatures displayed in Figure 5.4 are clearly free of any mischaracterization errors due to the channel's reduced sensitivity to cooler temperatures.

Table 5.1: Statistics for the MODIS 11 μm background brightness temperature[1].

Observation	Number of Pixels	Pixels with Error	% Error
California Test Cases (Development)			
All Pixels	37	3	8.1
Day Pixels	32	3	9.4
Night Pixels	5	0	0.0
Case Study (Application)			
All Pixels	890	157	17.6
Day Pixels	571	151	26.4
Night Pixels	319	6	1.90

[1] The California test cases are described in Chapters 3 and 4.

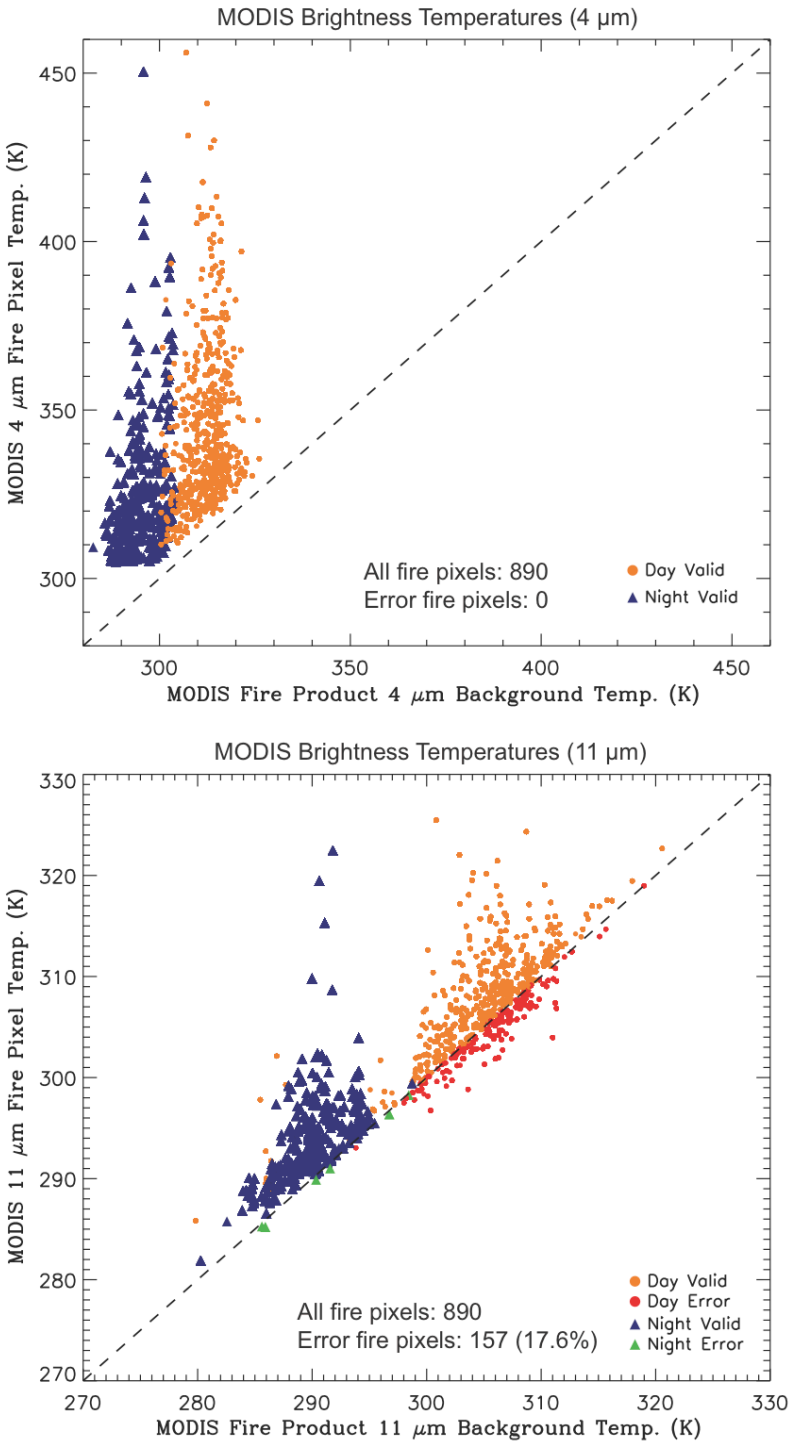

Figure 5.4: Scatterplots showing the pixel and background brightness temperatures at 4 µm (top) and 11 µm (bottom) for each MODIS fire pixel from the case study application. Day and night observations are respectively displayed as dots and triangles. The color scheme indicates whether each day or night pixel is valid or has a background temperature error. The corresponding statistical summary is provided in Table 5.1.

5.3 Using FRP_f Flux to Derive Fire Weather Relationships

When considering the very nature of fire events, FRP is an excellent parameter to focus on because it is a direct measurement of fire intensity (Ichoku et al., 2008a). However, since the advent of satellite-derived FRP products, few, if any, studies have investigated the relationship between FRP and meteorological variables. Peterson et al. (2010) did attempt to investigate any such relationships (via MODIS FRP_p) over broad spatial domains located within the boreal forest of North America, but showed that there is a very weak correlation between FRP_p and most fire-related weather variables, except for the overall synoptic environment (e.g. 500 hPa heights). The lack of any significant correlation between FRP_p and the meteorological variables (e.g. wind speed), which are assumed to greatly influence its intensity, likely stems from the previously described limitation of pixel size in the current MODIS FRP_p data. Therefore, the incorporation of retrieved fire area via the sub-pixel FRP_f flux should greatly increase the usefulness of FRP data in fire weather studies and the resulting effects on smoke production.

In this study, meteorological data were obtained from the North American Regional Reanalysis (NARR), which blends a variety of observational data into Eta model output containing 45 vertical layers across the North American continent with ~32 km grid spacing every three hours (Ebisuzaki, 2004, Mesinger, 2006). The NARR data (obtained in 2011 via http://nomads.ncdc.noaa.gov/data.php?name=access#narr_datasets) were subsequently downscaled onto a 10 km grid with one-hour temporal resolution by the Weather Research and Forecasting (WRF) model (e.g. Grell et al., 2005; Skamarock et al., 2005; Wang et al., 2012), and the MODIS fire observations, including the sub-pixel output, were geographically matched to the mesh of 10 km grid boxes and summed for

each day. This data integration step is essentially the same as the clustering sum of pixel-level retrievals methodology (described in Section 2.2) and acts to reduce the previously described sensitivity effects by averaging out several systematic errors. Therefore, the grid boxes with a higher number of MODIS fire pixels will likely provide retrieved fire area with a higher accuracy, but this will be examined in greater detail in Chapter 6.

While the California test cases allowed for a simple creation of fire clusters, comprised of several, mostly contiguous MODIS fire pixels, the case study domain described here (Figure 5.1) includes many fire pixels that may not be part of a contiguous cluster. In addition, the relatively large MODIS pixel size, varying from 1 to 10 km (depending on VZA), also limits the number of observed contiguous pixels. Therefore, investigating FRP_f flux for all fire pixels contained within a 10 km grid box (or any similar model grid) is the most advantageous application of a clustering methodology for MODIS data. Additional output includes the number of fire pixels, total fire area, total FRP_f, and the total FRP_p for each grid box, as well as the total number of invalid pixels, currently produced from 11 μm BT_{bm} errors and reaching the fire temperature threshold of 1500 K. These fire data can then be compared to the meteorological data from each model grid box at each one-hour time step.

Drawing from the widely used Canadian Forest Fire Danger Rating System (CFFDRS), surface wind speed and temperature are key variables affecting fire-spread potential (Wagner and Pickett, 1985; Wagner, 1987). As a result, these variables should also be strongly correlated to the FRP observations. However, Figure 5.5a,c shows there is very little correlation between MODIS FRP_p and the surface (10-meter) wind speed or

temperature (R_{wind} = 0.14, R_{temp} = 0.18), which is similar to the aforementioned results in Peterson et al. (2010). In contrast, the correlations with surface wind speed and temperature are significantly stronger (R_{wind} = 0.55, R_{temp} = 0.77), when using the FRP_f flux (Figure 5.5b,d). In addition, the mean FRP_f for 13 (57%) of these fire pixel clusters is greater than 100 MW (red triangles in Figure 5.5), suggesting that the large sensitivity to BT_{bm} errors will be reduced via the fire area component (e.g. Figure 4.12).

While these results are very encouraging, it is important to note that Figure 5.5 only shows the 23 largest fire clusters, defined as a WRF grid box with at least six valid fire pixels. When this cluster criterion is reduced, the correlation between FRP_f flux and each meteorological variable decreases, while the number of available data points increases (Table 5.2). For example, a cluster size limit of at least three valid pixels allows for 71 data points, but the resulting correlations (R_{wind} = 0.21, R_{temp} = 0.48) are much lower than the case with a cluster limit of six pixels. However, even with smaller cluster sizes, the correlations using FRP_f flux typically remain stronger than the correlations using the basic number fire pixels, MODIS FRP_p, and sub-pixel FRP_f (Table 5.2).

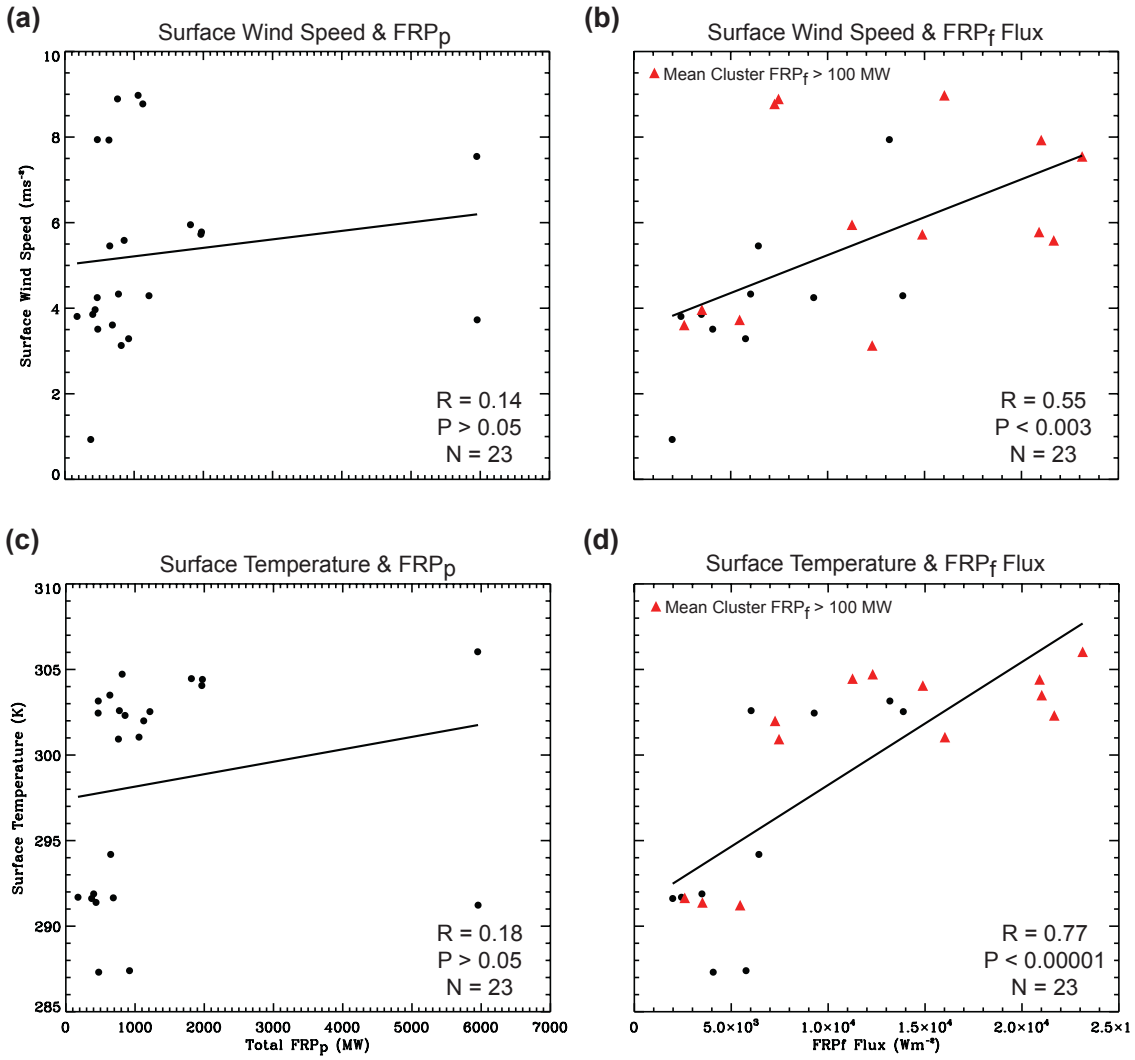

Figure 5.5: Analysis of meteorological and satellite-retrieved parameters for the 23 largest fire clusters in the case study domain (corresponding to Table 5.2). (a) Relationship between the MODIS FRP_p and surface (10-meter) wind speed. (b) Relationship between the cluster FRP_f flux and surface wind speed. (c) and (d) Same and (a) and (b) but for the surface (10-meter) temperature. The solid black line corresponds to the linear fit equation. R, P, and N denote the linear correlation coefficient, P-value, and number of data points, respectively. Red triangles in (b) and (d) indicate a fire pixel cluster with a mean $FRP_f > 100$ MW.

Table 5.2: Fire pixel cluster size and its effect on fire-weather correlations[1].

Variable	Cluster Limitation (Valid Pixels)	Number of Clusters	R Values	
			Wind Speed	Temperature
Fire Pixels	No limit	279	0.03	-0.05
FRP_p	No limit	279	0.11	0.07
FRP_f	No limit	279	0.09	0.03
FRP_f Flux	No limit	279	**0.02**	**0.19**
FRP_p	3	71	0.09	0.16
FRP_f	3	71	0.04	0.09
FRP_f Flux	3	71	**0.21**	**0.48**
FRP_p	4	52	0.08	0.17
FRP_f	4	52	0.03	0.10
FRP_f Flux	4	52	**0.33**	**0.54**
FRP_p	5	38	0.00	0.13
FRP_f	5	38	-0.05	0.05
FRP_f Flux	5	38	**0.37**	**0.55**
FRP_p	6	23	0.14	0.18
FRP_f	6	23	0.08	0.08
FRP_f Flux	6	23	**0.55**	**0.77**

[1] Fire pixel clusters are based on a 10 km model grid.

The effect of variations in cluster size threshold is further examined in Figure 5.6 by computing the correlation between the FRP and meteorological data for several fire pixel cluster size thresholds, ranging from 1 to 12 (a threshold of 12 indicates a cluster size ≥ 12 fire pixels). As random effects are averaged out, the correlations using FRP_f flux increase rapidly, become statistically significant, and begin to stabilize at a threshold of ~6 pixels, which is used in Figure 5.5 (upper limit in Table 5.2). In contrast, the correlations using the MODIS FRP_p remain very low ($R < 0.20$), and are not statistically significant for nearly every cluster size. This suggests that FRP_f flux is an improvement over FRP_p for characterizing fire weather, especially for large fire pixel clusters.

However, as described earlier, this case study is an idealized fire event with generally uniform meteorological conditions within a region that is devoid of any major topography. Therefore, attempting to identify relationships between meteorological variables and FRP_f flux in regions with complex topographic features, and potentially large mesoscale variability, will be more challenging (see Chapter 6).

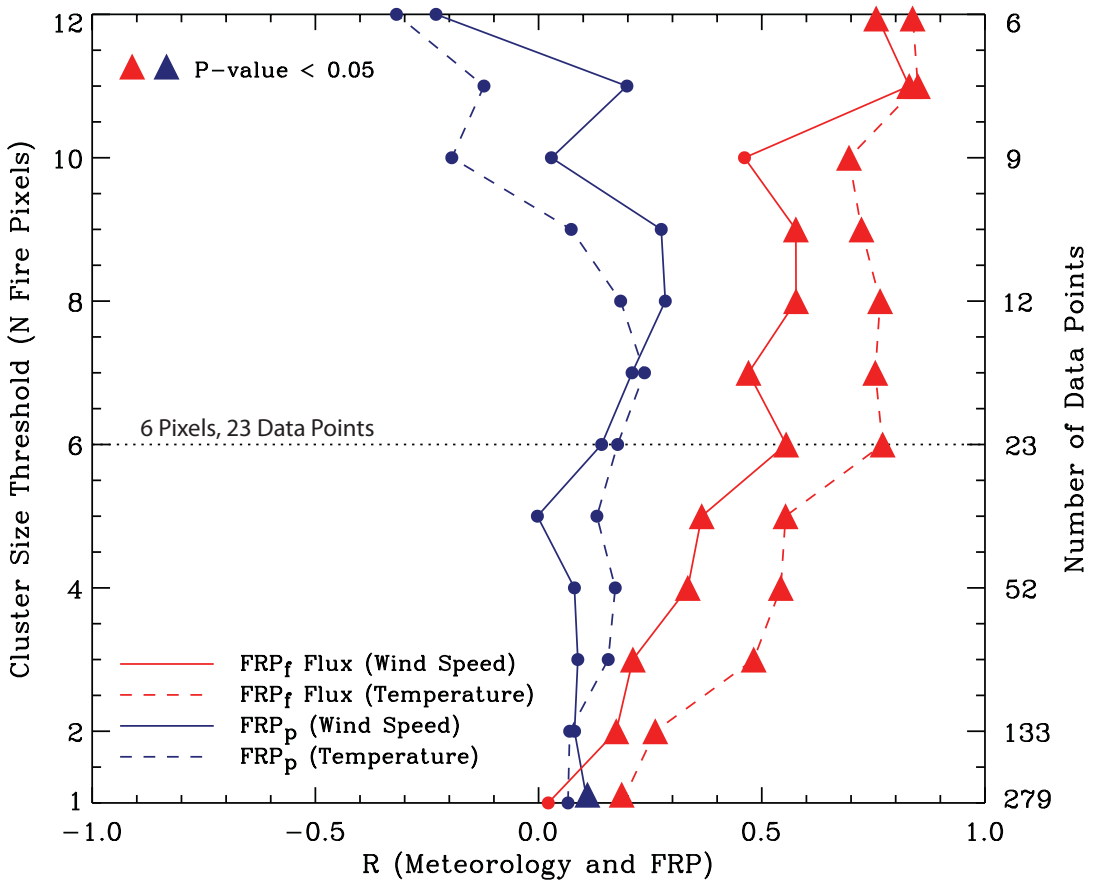

Figure 5.6: Correlations between the FRP data and the meteorological variables of surface wind speed (solid) and temperature (dashed) as a function of fire pixel cluster size and the number of available data points. Red curves indicate FRP_f flux and blue curves indicate FRP_p. Triangles are used to identify statistical significance, corresponding to a P-value < 0.05. The horizontal, dotted line indicates the fire pixel threshold used in Figure 5.5.

While this case study used a 10 km model grid, the methodology can easily be applied to any mesoscale model grid mesh. Increasing the grid size will produce larger fire clusters and reduce the uncertainty associated with the fire area component of the FRP_f flux, especially when the mean FRP_f is high. However, larger grid spacing may concurrently decrease the accuracy of the corresponding meteorological information; especially for variables like surface wind speed that often vary over short distances. As a result, caution must be used when integrating meteorological data archives and the MODIS sub-pixel fire output. Future sensors, such as NPP VIIRS (e.g. Csiszar et al., 2011), will have a higher spatial resolution (~750 m), and may allow for clustering based solely on contiguous fire pixel clusters, similar to the BIRD satellite (Zhukov et al., 2006). In these cases, the accuracy of FRP-based fire weather analysis will improve because large fire clusters will be predefined and easily separated from small fires.

5.4 Summary

This case study applied an operational version of the sub-pixel algorithm to a large 2011 fire event, centered on Texas and Oklahoma. Similar to the results in Chapter 4, this case study revealed that 17.6% of the 890 available fire pixels suffer from an overestimation error in the MODIS 11 μm background brightness temperature input data, with the vast majority, especially the large magnitude errors, occurring in daytime scenes. Similarly, background temperature underestimation errors, possibly associated with small fires, may produce an invalid fire temperature of 1500 K.

This chapter also showed that the sensitivity of the sub-pixel retrieval output is reduced when investigating large fire clusters (at least 4-6 MODIS fire pixels), which can defined based on the resolution of a mesoscale model grid. Subsequent comparisons with meteorological data showed that the cluster FRP_f flux, unlike the current MODIS FRP_p, has a statistically significant correlation with surface wind speed and temperature, especially for clusters 6 or more MODIS fire pixels. This encouraging result suggests that the cluster FRP_f flux is not only an improved parameter for investigating fire intensity, but may also be useful for characterizing the meteorological effects on fire intensity. In addition, the results discussed in this chapter provide valuable information for the potential applications of the sub-pixel retrieval, which are described in the following chapter.

Chapter 6. Potential Applications in Boreal North America

6.1 Introduction

In the previous chapter, the sub-pixel retrieval algorithm was tested on a single fire event in Texas and Oklahoma (4-8 September 2011), which highlighted the limitations and potential utility of FRP_f flux. This chapter reports on the first large-scale application of the algorithm, in which a much larger volume of data is incorporated from two recent fire seasons in the North American boreal forest. The specific study region, located primarily in central Alaska, is based on Peterson et al. (2010) and includes the core of the mountainous western boreal forest (Figure 6.1). Within the study region, the fire season typically falls between May and September (Skinner et al., 1999; Stocks et al., 2002; Fauria and Johnson, 2006), and the fire seasons of 2004 and 2005 were two of the three largest in the 73-year observational record (Kasischke et al., 2002). The North American boreal forest is an ideal region of study due to the potential for very large, intense fire events (example displayed in Figure 1.1). Previous research has shown that boreal fire events occasionally result in large-scale smoke transport, which may occasionally reach the Continental United States (e.g. Sapkota et al., 2005; Duck et al., 2007). In addition, over 30 years of research has focused on developing fire weather indices for operational use in the unique boreal ecosystem (e.g. Van Wagner and Pickett, 1985; Van Wagner, 1987; Amiro et al., 2004). This chapter will draw on these previous studies to examine the potential applications of FRP_f flux, including: (1) smoke plume injection height estimates, (2) fire weather, and (3) the potential for improved modeling and prediction of (1) and (2).

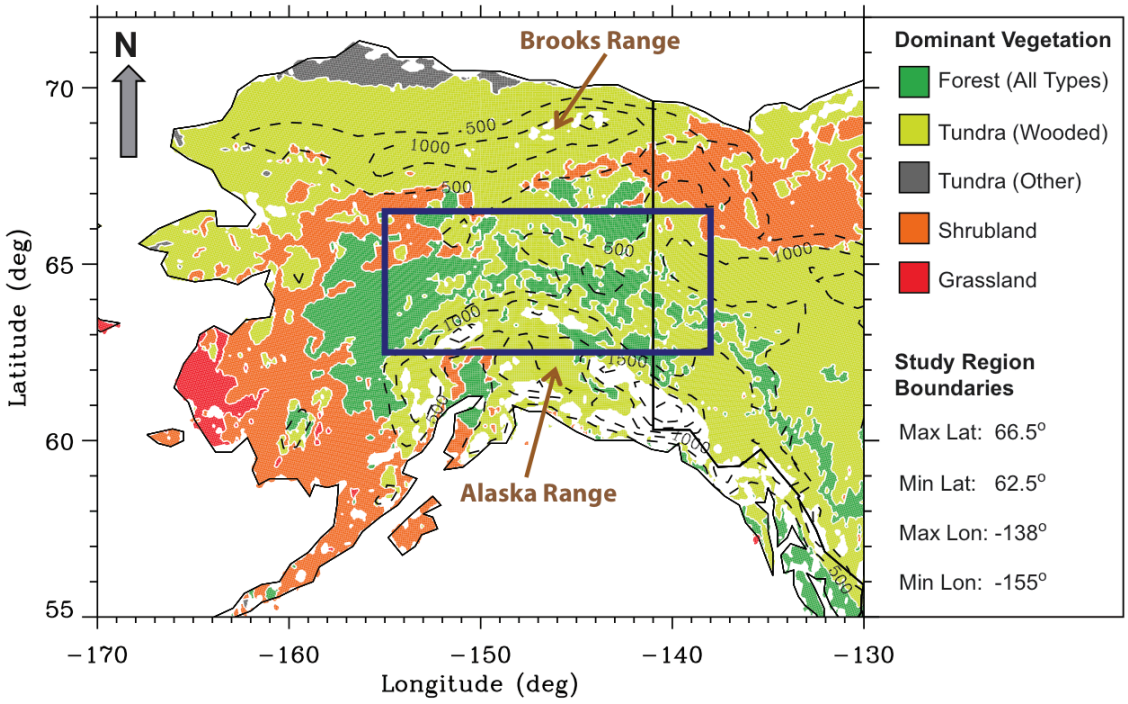

Figure 6.1: Map highlighting the boreal study region as a blue box (same as Figure A.1). The color scheme is based on the dominant vegetation types located within and surrounding the study region. Dashed black contours indicate variations in topography, with a contour interval of 500 meters.

6.2 Smoke Plume Injection Heights

Currently, many smoke emissions inventories and global chemical transport-modeling studies assume that smoke particles travel upward to a constant injection height based on an empirical relationship (e.g. Lavoue et al., 2000), or remain in the boundary layer (e.g. Reid et al, 2009). However, Wang et al. (2012) show an example where the injection height of 2 km, typically assumed in modeling studies in Southeast Asia (Figure 6.2a), should be reduced to ~0.8 km (Figure 6.2b) based on lidar observations provided by the Cloud-Aerosol Lidar with Orthogonal Polarization (CALIOP, Figure 6.2c). While it is commonly assumed that smoke aerosol particles are uniformly distributed up to a

peak altitude, Kahn et al. (2007) show that these particles tend to concentrate at discrete layers of increased atmospheric stability, located at the top of the boundary layer (BL) or another stable layer aloft. In addition, cases of pyroconvection, which have been observed in many regions across the globe, can inject aerosol particles into the stratosphere (Fromm et al., 2010). Indeed, fire characteristics can vary dramatically between individual fire events, biomes, and climate zones, greatly impacting smoke plume behavior, especially due to changes in fire intensity and local meteorological conditions. This suggests that accurate modeling of smoke plume dynamics will require plume height information for every observed fire.

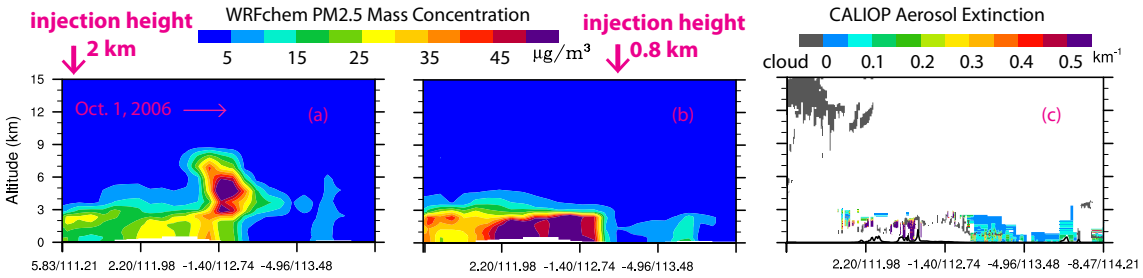

Figure 6.2: Inter-comparison of CALIOP-derived vertical profile of aerosol extinction coefficient (c) with the WRFchem simulated vertical profile of smoke concentration along the corresponding CALIPSO ground track (a) and (b) on 1 October 2006. The model results in (a) are from a simulation with a smoke injection height at 2 km, while (b) uses a smoke injection height of 0.8 km (adapted from Wang et al., 2012).

Unfortunately, the only two available satellite sensors that can give an indication of plume height at the global scale have severe limitations in spatial and temporal coverage. CALIOP observes only curtains over a set of north-south lines that are hundreds of kilometers apart, and sees plumes only sparingly (e.g. Kahn et al, 2008). Similarly, The Multi-angle Imaging SpectroRadiometer (MISR) can only observe a given location once every 8 days, and only during the daytime (e.g. Diner et al., 1998; Kahn et

al., 2007, 2008). Therefore, the only feasible way to obtain accurate plume height information for every observed fire is to derive it from the FRP data themselves.

As described in previous chapters, the potential link between the current MODIS FRP_p and smoke plume injection heights has not been quantitatively established, largely due to the lack of sub-pixel information for fires (e.g. Eckmann et al., 2010). Therefore, the FRP_f flux calculation could be a valuable asset to global fire monitoring (e.g. Zhukov et al., 2006; Peterson et al., 2012a) by providing estimates of the radiant energy (over the retrieved fire area) that in turn, relates to the true fire intensity that produces the thermal buoyancy of the smoke plume (Kahn et al., 2007, 2008). This information can then be used in combination with MISR and CALIOP plume height observations (where available) to derive quantitative relationships between observed FRP_f flux and smoke plume heights, ultimately improving smoke transport modeling and forecasts. The following sections provide an example comparison between MISR smoke plume height and FRP data (both FRP_p and FRP_f flux) within the study region highlighted in Figure 6.1.

6.2.1 MISR Smoke Plume Height Data

In this example, the MISR sensor aboard the Terra satellite is the primary source of smoke plume height data. MISR provides multi-angle radiance imagery from a set of 9 push-broom cameras, allowing the retrieval of buoyant smoke plumes and other aerosol layer heights above ground level, along with motion vectors via stereoscopic methods (e.g. Diner et al., 1998; Val Martin et al., 2010). MISR data are provided at vertical and horizontal resolutions of 500 m and 1.1 km, respectively (Kahn et al., 2007). As shown in Figure 6.3, individual smoke plumes are retrieved using the MISR INteractive

eXplorer (MINX), whereby a MINX user digitizes the source, boundaries, and smoke plume transport direction based on the corresponding Terra MODIS fire pixel locations (Figure 6.3a). Provided for several geographic regions between ~2001 and 2009, the output for each individual MISR data point, located within a digitized smoke plume, includes smoke heights (Figure 6.3b), wind speeds, albedos, and aerosol properties. This information (obtained in early 2012) is available from the MISR Plume Height Project (http://misr.jpl.nasa.gov/getData/accessData/MisrMinxPlumes).

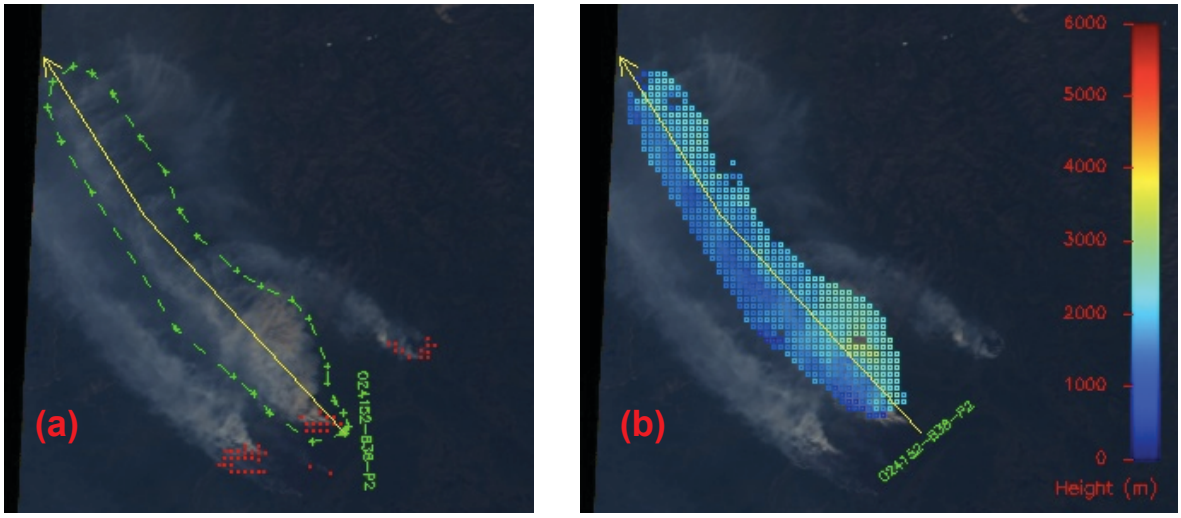

Figure 6.3: (a) MISR imagery showing an example of a digitized plume region (green), wind direction arrow (yellow) and Terra MODIS fire pixels (red). (b) Same as (a), but color-coded based on MISR wind-corrected plume heights (http://misr.jpl.nasa.gov/getData/accessData/MisrMinxPlumes/).

The MISR plume height data are limited by potential bias and errors inherent in the digitizing process as well as the exclusion of pyroconvection events (e.g. Val Martin et al., 2010). The Aqua satellite does not have a MISR sensor, thus only MODIS fire data obtained from the Terra satellite are applicable. In addition, the Terra daytime overpass, occurring in the late morning or early afternoon local time, does not coincide

with the late afternoon maximum of observed fire intensity (e.g. Ichoku et al., 2008). While additional smoke plume information is available from CALIOP (lidar data, Figure 6.2c), these data are better suited for horizontally extensive, but optically thin, boundary layer smoke located in downwind regions (e.g. Kahn et al., 2008). Therefore, despite several limitations, MISR data are the best available option for investigating smoke plume heights near the source.

This study uses the median height of each smoke plume, obtained by averaging the individual MISR data points within the digitized smoke plume boundary (e.g. Figure 6.3b). MISR plume heights are provided as the height above sea level (Kahn et al., 2008), and therefore must be corrected a priori for the terrain in the boreal study region (Figure 6.1). The MODIS fire pixel locations and FRP_p values, provided by the plume height database, are then used to locate the matching FRP_f flux values. However, the total number of FRP_p and FRP_f flux data points are rarely the same due to the pixel overlap correction included within the sub-pixel retrieval algorithm described in Chapters 2 and 3. Therefore, only the MODIS fire pixels that coincide with FRP_f flux observations are used to define a single fire pixel cluster because: (1) the standard MODIS fire product, including FRP_p data, does not account for pixel overlap, which likely creates a positive bias in the fire cluster's total FRP_p and (2) MISR plume height data are provided for individual smoke plumes that obviously correspond to the same fire event.

6.2.2 Comparing MISR Smoke Plume Heights with FRP Data

As highlighted in previous chapters, the FRP_f flux data should be used at the cluster-level (not the individual pixel-level) to reduce the effect from random sources of error, including PSF effects and background temperature. In this example, the cluster

size threshold is set at the minimum number of fire pixels required to reduce the noise in the FRP_f flux data located within the boreal study region (Figure 6.1). This is visualized in Figure 6.4 by computing the correlation between the FRP data and smoke plume height for several fire pixel cluster size thresholds, ranging from zero to 25 (a threshold of 25 indicates a cluster size > 25 fire pixels).

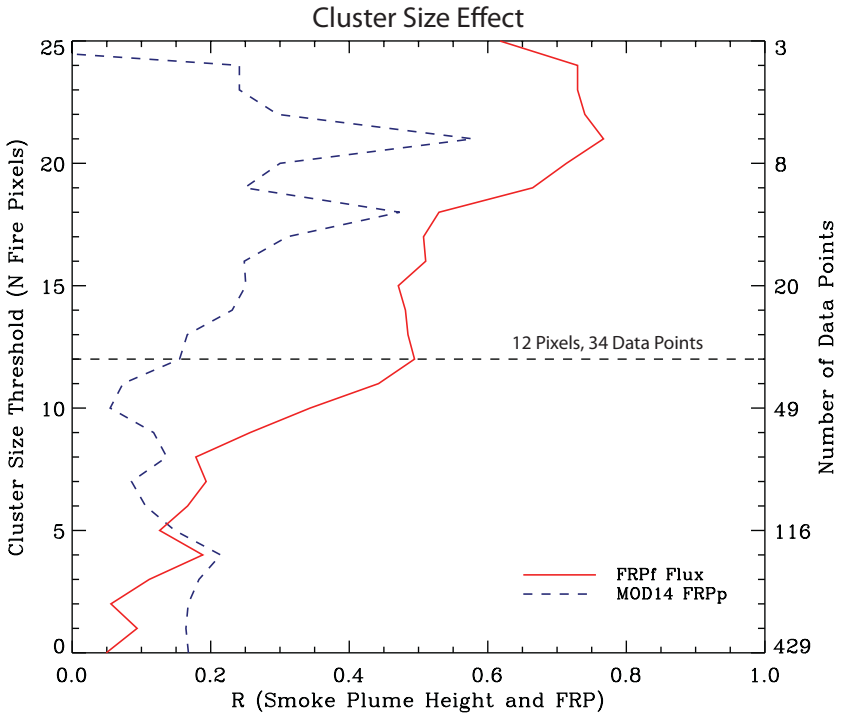

Figure 6.4: Relationship between MISR smoke plume heights and FRP data, including FRP_f flux (red line) and FRP_p (dashed blue line), as a function of fire pixel cluster size and the number of available data points.

This display shows that FRP_p is weakly correlated with smoke plume height, except when the fire pixel cluster threshold is more than 17 pixels and the number of remaining data points is small. In contrast, the correlation between FRP_f flux and smoke plume height increases rapidly as the fire pixel cluster size reaches 10 to 12 pixels, thus indicating the threshold where random effects begin to be averaged out. Above 12 pixels,

the R-value for the FRP_f flux curve (red line) remains consistently above ~0.5. However, it is obvious that the vast majority of fire events, corresponding to this sample of plume height data, contain only 1-5 fire pixels. Therefore, setting a cluster threshold between 10 and 12 pixels includes only about 8-11% of the available data points.

Using the 34 available data points provided by a cluster threshold of 12 fire pixels (highlighted by the dashed horizontal line in Figure 6.4), comparisons between MISR smoke plume heights and FRP data show that the current MODIS FRP_p produces a weak relationship with smoke plume heights (R = 0.16, Figure 6.5a). In contrast, Figure 6.5b shows that FRP_f flux displays a stronger relationship (R = 0.49), and therefore may offer a more reliable characterization of the thermal buoyancy required for estimating smoke plume height. While the sample size is small, improved plume height estimates have the most value for these large fire events due to the increased chance of injection above the BL and large-scale smoke transport.

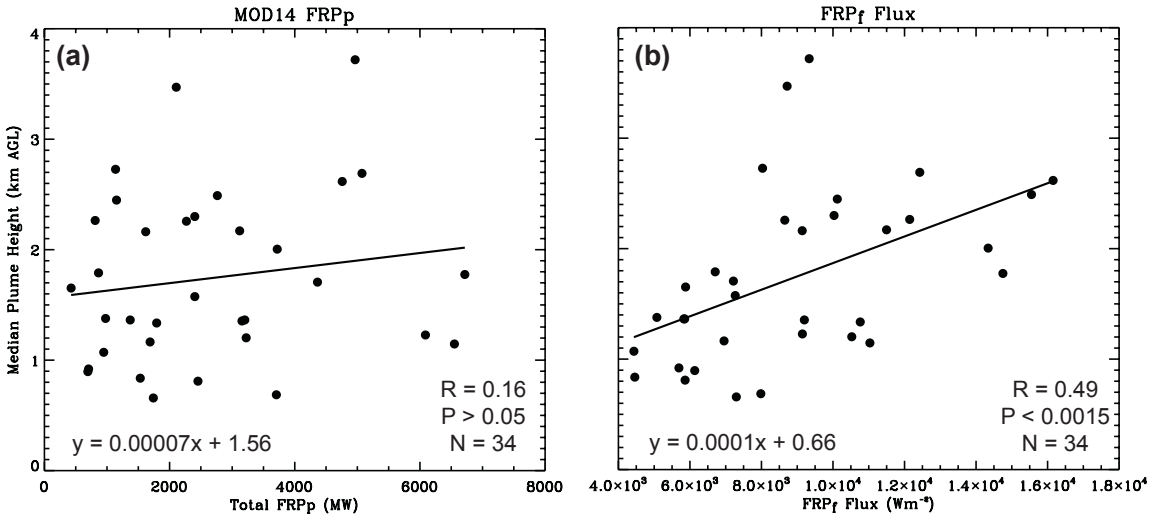

Figure 6.5: (a) Relationship between the Terra MODIS FRP_p and MISR smoke plume height for clusters of at least 12 MODIS fire pixels in the boreal forest of Alaska (2004 and 2005). (b) Same as (a), but using the cluster FRP_f flux. The solid black line corresponds to the linear fit equation. R, P, and N denote the linear correlation coefficient, P-value, and number of data points, respectively.

Using a similar study region, Kahn et al. (2008) show that while the height of the BL can range from 0.25 to 3.0 km, it is commonly observed between ~1.0 and 1.5 km, and only about 10% of smoke plumes are injected above this threshold. Figure 6.5b shows that the smoke plumes provided in this sample range in height from 0.5 – 4.0 km, and there is potential for smoke plumes to reach above 1.5 km for nearly the entire range of observed FRP_f flux values (4000 – 18000 Wm^{-2}). Therefore, drawing on the results by Kahn et al. (2008), there is at least some potential for smoke to be injected above the BL when the FRP_f flux of the fire cluster is greater than 4000 Wm^{-2}. While the results in Figure 6.5 are a useful first step, future studies are necessary to examine a much larger data sample that also includes BL height information. The slope and intercept of the regression line (as displayed in Figure 6.5) could then be used to derive smoke plume heights based on the observed value of FRP_f flux. When comparing these predicted plume heights to atmospheric stability information (e.g. local radiosonde data) and the fire weather information described in the following section, estimates can be produced for the potential of smoke injection above the BL, and therefore large-scale smoke transport.

6.3 Fire Weather Analysis and Prediction

The analysis from the case study (presented in Chapter 5) showed that FRP_f flux may be useful for characterizing the meteorological effects on fire intensity, and the previous section showed that smoke plumes may reach above 1.5 km, and potentially the BL, when the FRP_f is greater than 4000 Wm^{-2}. Therefore, the following sections are

devoted to identifying a key combination of meteorological variables that produce a high probability of occurrence for FRP_f flux values greater than 4000 Wm^{-2}.

6.3.1 Fire Weather Variables and Indices

A broad body of research over the past several decades has tried to discern the role of local meteorology, topography, climate, and land use in the formation of intense fire seasons (e.g. Skinner et al., 1999; Stocks et al., 2002). For example, active boreal fire seasons have been linked to positive 500 hPa geopotential height anomalies (Skinner et al., 1999, 2002), which must persist for approximately 10 days (Fauria and Johnson, 2006). Fire weather indices have also been developed to guide forecasts for the potential of fire ignition and spread. The Haines Index, which is widely used in the United States, is an integer scale (1-6) that indicates the potential for fire ignition and growth based on two equally weighted ingredients for moisture and stability, respectively derived from the surface dew point depression and atmospheric lapse rate (Haines, 1988; Potter et al., 2008).

In contrast to the Haines Index, the fire indices used in the boreal forest regions generally disregard atmospheric instability. The widely used Canadian Forest Fire Danger Rating System (CFFDRS) incorporates surface temperature, relative humidity, rainfall, and wind speed to produce operational forecasts of fire potential and spread in the unique boreal ecosystem (Amiro et al., 2004). The CFFDRS is calculated based on weather station observations at local noon and contains six components describing the potential for fire ignition and spread (Van Wagner and Pickett, 1985; Van Wagner, 1987). Of these, the three measures of biomass moisture include: (1) the fine fuel moisture code (FFMC) describing the moisture content of the fine plant litter in a thin

layer on the forest floor, (2) the duff moisture code (DMC) describing the moisture content of entire upper portion of the organic material on the forest floor, and (3) the drought code (DC) describing the long-term moisture content of deeper layers of organic material. The FFMC is combined with surface wind speed to produce the initial spread index (ISI), describing fire spread potential, while the DMC and DC are combined to produce the buildup index (BUI), which describes the overall fuel conditions. Finally, the ISI and BUI are combined to produce the fire weather index (FWI), which describes the overall fire weather situation for the next 24 hours. While the CFFDRS was developed for the North American boreal forest, it has recently been applied, with some skill, to the biomes of Southeast Asia (Dymond et al., 2004; 2005), suggesting that the CFFDRS may have the potential for global application.

In order to characterize fire variability, scattered reports of weather, fire, and burned area from ground observations are often used. However, these reports are sometimes unreliable and insufficient to describe the spatiotemporal distribution (including the start and end dates) of fire events and their intensity over the full domain of wildfire-affected regions in boreal North America (Flannigan and Wotton, 1991; Stocks et al., 2002; Roy et al., 2007; Pouliot et al., 2008; Soja et al., 2009). Therefore, a continuous source of data from a reanalysis or numerical weather prediction (NWP) is required (see Appendix). The case study in Chapter 5 used NARR data downscaled by the WRF model (~10 km). However, the example presented here is based entirely on the 32 km grid spacing of the NARR (Ebisuzaki, 2004; Mesinger, 2006). In addition to providing several key fire weather variables, the NARR data are also used to produce the six components of the CFFDRS, but several modifications required in the NWP-based

approach. While all six CFFDRS components are required for fire weather analysis, the FWI and ISI are the most relevant to short-term changes in fire activity (see Appendix).

6.3.2 Grid-Based Joint Probability Analysis Using FRP_f Flux

As described by Peterson et al. (2010), the probability of a specific event's occurrence (here FRP_f flux > 4000 Wm^{-2}) can be computed based on a combination of meteorological factors. The approach, similar to the MISR smoke plume analysis (Figure 6.4), begins by defining the fire pixel cluster threshold. However, in this case, the data integration methodology from the case study (Chapter 5) is applied to define fire clusters based on the number of fire pixels within a NARR grid box (aggregated to 32 km). In contrast to the case study, Figure 6.6 shows that the correlation FRP_f flux and weather information in the boreal study region is rather weak ($R < 0.50$), even at the largest fire pixel clusters. This may be a result of the larger grid spacing (32 km) compared to the case study (10 km), which likely affects the skill of each variable for prediction of fire activity. For example, the stronger correlation with wind speed observed in the Texas and Oklahoma case study ($R = 0.55$) was influenced by strong, unidirectional surface winds, which are unlikely to occur in the boreal study region due to the presence of complex topographic features (Figure 6.1). In addition, sub-regional variations in topography likely produce large variations in temperature and wind speed over short distances that are not resolved by the 32 km grid spacing. Despite this limitation, higher resolution data are not considered in this example because future operational forecasting applications will use a variety of regional or global NWP datasets that have similar or even coarser spatial resolutions than the NARR.

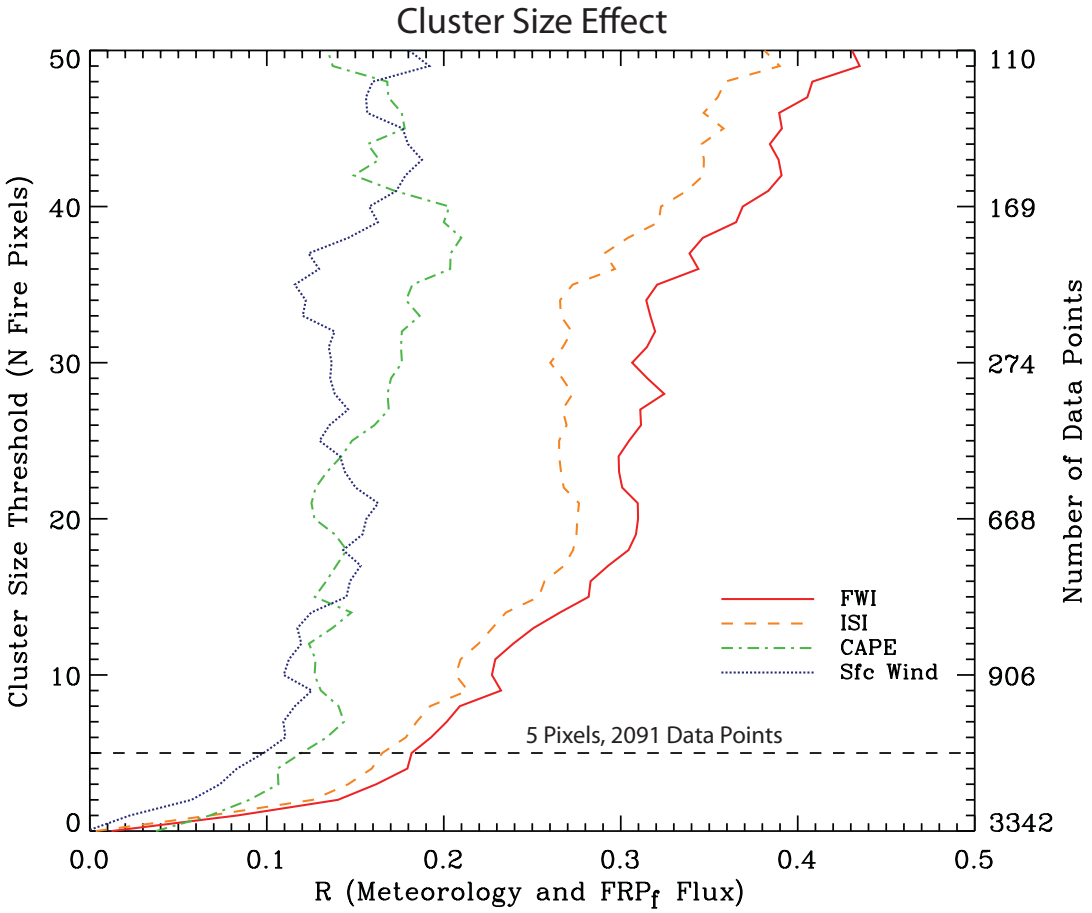

Figure 6.6: Relationship between several meteorological variables and FRP_f flux as a function fire pixel cluster size and the number of available data points. Fire pixel clusters are defined as the total number of MODIS fire pixels within a NARR grid box (32 km resolution).

Similar to the case study in Chapter 5, Figure 6.6 clearly shows that the FRP_f flux and weather comparisons begin to stabilize when there are more than five fire pixels in a cluster, providing 2091 available data points or 63% of the available data (horizontal, dashed black line). Therefore, 37% of the fire events are small, with a cluster size of five fire pixels or less (e.g. ≤ 5 fire pixels observed within a NARR grid box). The distribution of the available fire pixel clusters (pixels per grid box) is very asymmetric (a

gamma distribution, Figure 6.7a), thus fire events well above the threshold of five pixels, especially those with a cluster size greater than 50 fire pixels, occur rarely.

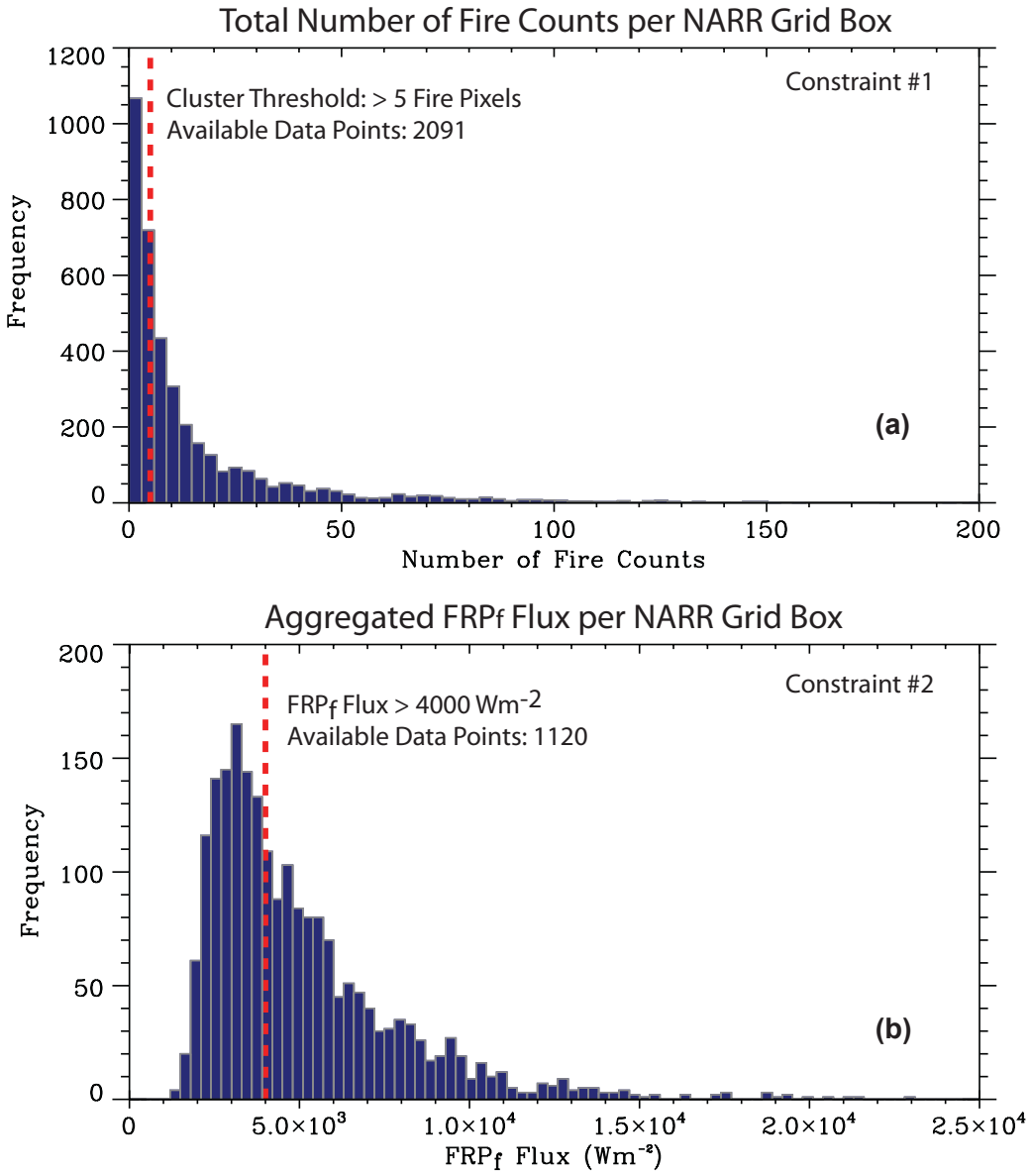

Figure 6.7: (a) Histogram showing the distribution of the number of MODIS fire pixels (fire counts) per NARR grid box, with the fire pixel cluster threshold denoted by the red, dashed line. (b) Histogram showing the distribution of the aggregated FRP_f flux for the fire pixel clusters that remain after applying the cluster threshold in (a). The red, dashed line indicates the lower limit of the FRP_f flux data (4000 Wm^{-2}) that will be considered in the joint probability analysis.

The cluster size threshold is a required preliminary constraint, but a secondary constraint is also required to isolate the cases of interest, defined as an FRP_f flux greater than 4000 Wm^{-2}. Figure 6.7b shows the distribution of the FRP_f flux data, after the cluster size threshold is applied, which is much more Gaussian than the cluster size distribution. The observations of an FRP_f flux above 4000 Wm^{-2} comprise 53% (1120 data points) of the available FRP_f flux data (2091 data points). Therefore, the remaining 1120 data points can be used, in combination with meteorological data, to calculate the probability of occurrence (or joint probability) for these high FRP_f flux events.

The components of the CFFDRS (FWI and ISI) displayed in Figure 6.6 clearly have a stronger relationship with FRP_f flux than the individual variables. However, as described in the Appendix, fire weather indices, while designed to describe the entire fire weather situation, are not perfect indicators of changes in fire activity, and must be supplemented with additional information. In the case of the CFFDRS, atmospheric instability is the key variable neglected in the calculations, especially for the ISI and FWI. Instability can be used as an indicator of dry lightning potential, and may also be important indicator of changes in ongoing fire activity (e.g. Peterson et al., 2010). Measures of instability can either be derived based on the Haines Index (Haines, 1988; Potter et al., 2008), which requires the combination of a dry lower troposphere with a large low-level lapse rate (inverted V sounding), or from convective available potential energy (CAPE), which is derived from the entire atmospheric column and requires a higher amount of lower-tropospheric water vapor (loaded gun sounding). Both methods have been linked to extreme fire events, including pyroconvection, but large fire events may be present when the Haines Index component is high and CAPE is low, or visa versa

(e.g. Peterson et al., 2010; Fromm et al., 2010). In this example, CAPE is used because it is has previously been linked to fire activity in the boreal forest and is specifically provided by the NARR.

In order to quantify the potential for lightning-ignited fires, Peterson et al. (2010) computed the probability of dry lightning strike occurrence as a function of 500 hPa geopotential heights and CAPE. For fire intensity investigations, this probability function can be easily modified to compute the probability of an FRP_f flux greater than 4000 Wm^{-2}, based on CAPE and the FWI (or a related variable). To begin, the observed range of the two meteorological variables of interest is divided into ~40 bins per variable. This forms a mesh of 1600 bin boxes per variable, with CAPE in one dimension and the FWI in the other dimension. By tallying the available NARR grid boxes in each bin box (N_{tot}), the joint number density distribution of data points based on the two input metrological variables can be ascertained. Figure 6.8a provides an example of N_{tot} based the FWI and CAPE, and shows that the majority of observations have an FWI below 10 and CAPE values below 400 Jkg^{-1}. Similarly, Figure 6.8b displays the total NARR grid boxes that correspond only to cases where the FRP_f flux exceeded 4000 Wm^{-2} (F_{tot}). While it is expected that the bin boxes with a high F_{tot} will correspond to high FWI values, many of these intense fire events occur below the FWI threshold corresponding to extreme fire activity (FWI between 20 and 30, Van Wagner, 1987). However, for both N_{tot} and F_{tot}, the bin boxes containing data are distributed across a wide range of FWI and CAPE values, suggesting that instability is likely a contributing factor. In some cases, the fires themselves may even contribute to the observed CAPE value, but this potential feedback effect should be reduced when averaged over a ~32 km NARR grid box.

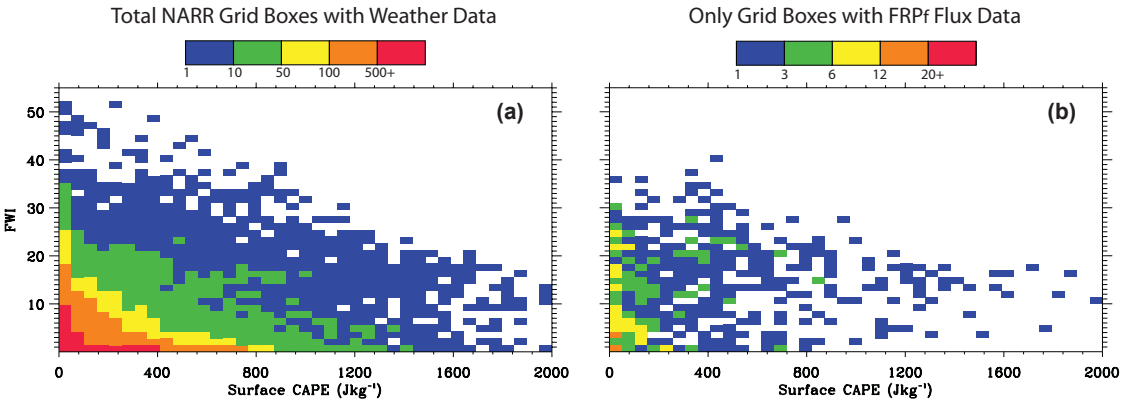

Figure 6.8: (a) Joint number (of data points) distribution of CAPE and the FWI for all available data points (N_{tot}) within the study region displayed in Figure 6.1. (b) Same as (a) but only for data points corresponding to an FRP_f flux > 4000 Wm^{-2} (F_{tot}).

Based on Figure 6.8, the probability of occurrence for an FRP_f flux above 4000 Wm^{-2} can be computed for each bin box by: F_{tot}/N_{tot} (Figure 6.9a). The resulting probability values greatly increase for increasing values of FWI and CAPE, and are at their highest (e.g. > 50%) when the FWI is greater than 20 and/or the CAPE is greater than 1200 Jkg^{-1}. However, regardless of the FWI observation, the probability of an intense fire event is low when there is less than 100 Jkg^{-1} of observed CAPE. Similar results are obtained when the FWI is replaced with the ISI (Figure 6.9b). In this case, the highest probability values occur when the ISI is greater than 10 (the value typically used to indicate extreme fire activity) and CAPE values are greater than 1200 Jkg^{-1}.

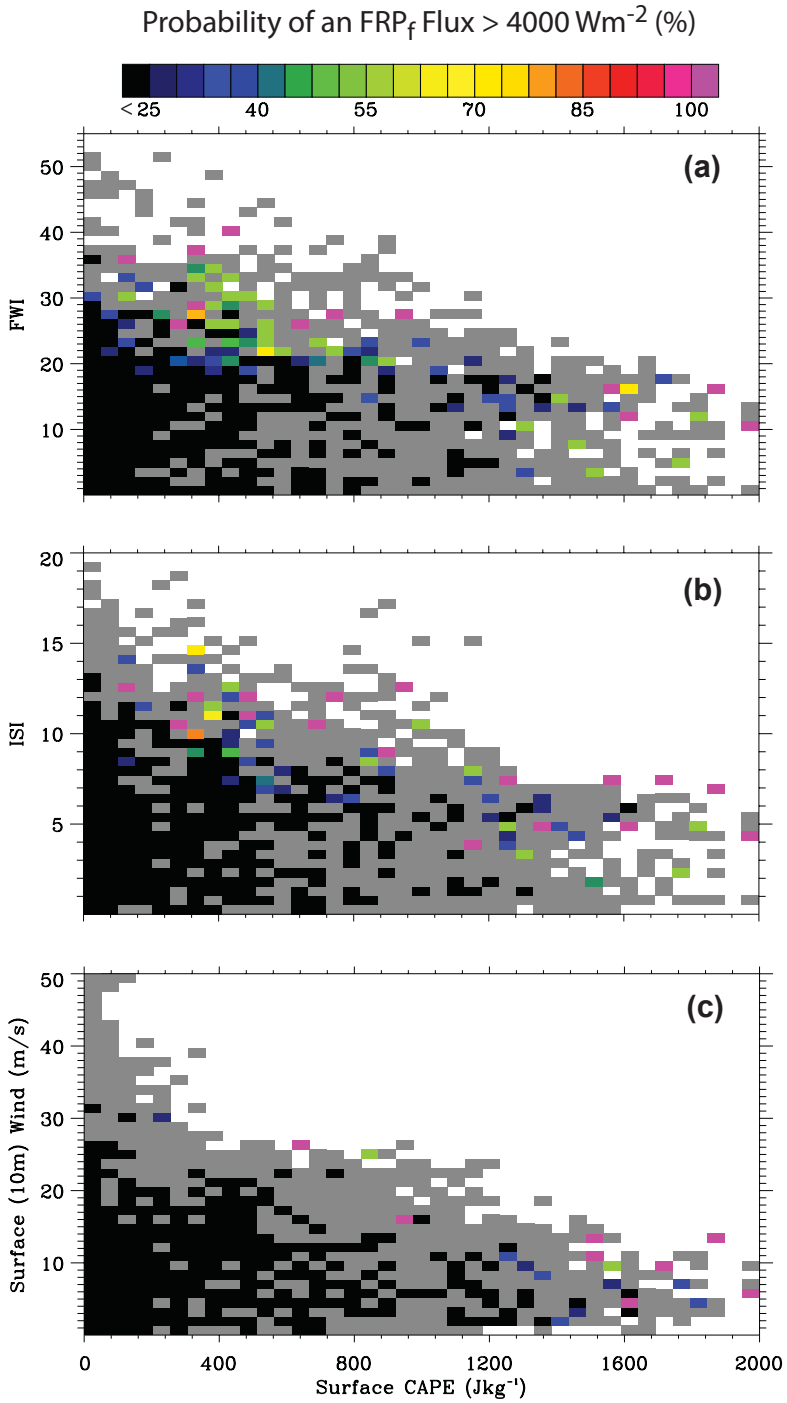

Figure 6.9: Probability (F_{tot}/N_{tot}) of an FRP$_f$ Flux > 4000 Wm^{-2} as a function of (a) CAPE and FWI, (b) CAPE and ISI, and (c) CAPE and surface (10 meter) wind speed for the boreal study region displayed in Figure 6.1. The observed meteorological values for 2005-2006 with a probability of FRP$_f$ Flux occurrence ≥ 25% are shaded in color, values with a probability of FRP$_f$ Flux occurrence between 0 and 25% are shaded in black, values without FRP$_f$ flux occurrence are shaded in grey, and white areas do not contain observed data.

In contrast, replacing the ISI or FWI with a single variable, such as surface (10 meter) wind speed, does not produce robust results (Figure 6.9c). This stems from the weaker correlation between surface wind speed and FRP_f flux, compared to the counterparts of the FWI or ISI, observed in Figure 6.4. Therefore, the probability function created from combination of the FWI (or ISI) and CAPE is the most useful tool for identifying the set of conditions required for a high probability of intense fire events (FRP_f flux > 4000 Wm^{-2}). This combination also serves as an improvement for examining the overall fire weather scenario by including an instability component that can partially explain the occurrence of intense fire events when the FWI (or ISI) is low.

6.4 Summary

By incorporating fire data from two large fire seasons (2004 and 2005) in the North American boreal forest, this chapter provided examples of the primary applications for FRP_f flux, including the analysis and prediction of smoke plume injection heights and fire weather. The strong correlation between FRP_f flux and MISR smoke plume height observations shows that it may be possible to use FRP_f flux to derive smoke plume height information for large fire pixel clusters. Drawing from previous studies, this example also showed that there is potential for smoke to be injected above the BL when the FRP_f flux is greater than ~4000 Wm^{-2}. Therefore, smoke plume information derived from FRP_f flux will be very useful in future smoke modeling studies, by allowing the smoke plume injection height to be specified with greater accuracy. However, additional

analysis is required to examine a variety of fire events across the globe and their associated atmospheric stability profiles.

Comparisons between FRP_f flux and meteorological data highlighted the importance of atmospheric instability (e.g. CAPE) and fire weather indices (generated by NWP), such as the FWI and ISI, for quantifying the potential for intense fire events (FRP_f flux > 4000 Wm^{-2}). This analysis showed that the probability of an intense fire event greatly increases for increasing values of FWI and CAPE. In addition, CAPE values above 1200 Jkg^{-1} partially explain the occurrence of intense fire events when the FWI (or ISI) is low, and replacing the fire weather indices with a single variable (e.g. wind speed) produces weaker results. By incorporating BL height information, future analysis will be able to compute a similar probability function for smoke injection above the BL, provided an FRP_f flux greater than 4000 Wm^{-2} is also observed (e.g. Peterson et al., 2010).

While a larger sample size is needed, the smoke plume height and fire weather analysis described in this chapter is an important first step toward understanding the mechanisms that drive intense fire events, potentially resulting in high-altitude smoke plumes. By supplementing the available suite of input variables, FRP_f flux may also be useful for improving short-term predictions of satellite-observed fire activity. These potential forecasting tools are currently based solely on the number of observed MODIS fire pixels (fire counts), and have limited prediction skill (described in the Appendix).

Chapter 7. Conclusions

7.1 Summary of Key Results

In an effort to provide a fire area and temperature-based FRP product, this study developed a MODIS sub-pixel retrieval algorithm for fire area and temperature, which is used to calculate FRP_f. The retrieval was designed such that it can be run on any MODIS granule across the globe and a radiative transfer model was used to account for atmospheric effects. Using a lookup table approach, the retrieval can be run at both the pixel and cluster levels and corrections are made for overlapping pixels. Currently, the 4 and 11 μm background temperatures are direct inputs from the MODIS fire product (Collection 5).

For the first time, the near-coincident observations obtained from the AMS, flown aboard the NASA Ikhana UAS, allowed the retrieved MODIS fire areas to be assessed with unprecedented accuracy (3-50 meter resolution). In addition, comparisons between the AMS and MODIS fire areas revealed the impacts from several indirect effects on the retrieval that are difficult to characterize, such as PSF effects, location relative to nadir (viewing zenith angle), and the overall distribution of sub-pixel hot spots within the fire pixel. As a result, it was suggested that a clustering methodology should be implemented to reduce the error potential in retrieved fire area, and the clustering sum of individual retrievals method may have the greatest relevance to future operational algorithms. These fire clusters, along with the sub-pixel-based FRP_f, allowed a large fire burning at a low intensity to be separated from a small fire burning at a high intensity, and also facilitated calculations of FRP_f flux over the retrieved fire area.

A theoretical sensitivity analysis was provided for the three major outputs of the sub-pixel retrieval algorithm (fire area, FRP_f, and FRP_f flux) based on direct input variables and assumptions. This analysis focused primarily on variations in the atmospheric profile, background emissivity, and background brightness temperature, which were analyzed to varying levels of detail. Results indicate that significant reductions in the retrieved pixel-level fire area will occur if the observed column water vapor is very low with respect to the mid-latitude summer, climatologically based profile. The effect on FRP_f is much smaller because the decrease in retrieved fire area is offset by an increase in retrieved fire temperature. Therefore, the overall sensitivity of the cluster FRP_f flux falls between that of retrieved fire area and FRP_f, but is highly influenced by changes in fire area. In contrast, potential variations in the assumed values for the 4 and 11 μm background emissivities have a minor effect on all retrieval output (e.g. < 15% change in fire area and FRP_f), except when fire events are surrounded by large regions of highly reflective, brown vegetation.

When considering all potential sources of direct error, small deviations in the 11 μm BT_{bm} (background noise) produce the greatest affect on all retrieval outputs. For example, a ±1 K error can produce a change in retrieved fire area of more than an order of magnitude, with the potential for large impacts on FRP_f and the cluster FRP_f flux as well. For some MODIS fire pixels, the sub-pixel retrieval can even become irrelevant when the 11 μm BT_{bm} (provided by MODIS) is greater than the pixel brightness temperature. The case study application (in Texas and Oklahoma) showed that 17.6% of the 890 available fire pixels suffered from this BT_{bm} error, with the vast majority, especially the large magnitude errors, occurring in daytime scenes. While additional

input variables can alleviate potential errors caused by the water vapor and emissivity assumptions, BT_{bm} errors stem from the MODIS fire product, and are therefore the primary sources of error in sub-pixel calculations.

For fire weather applications, clusters of fire pixels can be created to reduce the aforementioned sensitivity by geographically matching each pixel's location to the mesh of grid boxes provided by NWP datasets. While the skill of NWP data is limited by changes in spatial resolution, the idealized case study in Texas and Oklahoma revealed that the cluster FRP_f flux, unlike the current MODIS FRP_p, has a statistically significant correlation with several meteorological variables. Drawing from these results and the potential for smoke injection above the BL, the probability of occurrence for intense fire events (e.g. FRP_f flux > 4000 Wm^{-2}) was computed based on a combination of meteorological factors, including NWP-generated fire weather indices and CAPE. This analysis showed that the probability of an intense fire event greatly increases for increasing values of FWI and CAPE, and replacing the fire weather indices with a single variable (e.g. wind speed) produces weaker results. By incorporating MISR smoke plume height observations that correspond to large fire pixel clusters, this study also showed that FRP_f flux may be useful for the direct derivation of smoke plume height information, and assessing the potential for smoke injection above the BL.

7.2 Implications of this Study and Future Work

Over the next decade, the new generation of satellite sensors, such as NPP VIIRS (e.g. Csiszar et al., 2011) and GOES-R (Schmidt et al., 2011, http://www.goes-r.gov/),

will replace the current generation sensors, including MODIS. The sub-pixel algorithm described in this study is designed for easy application to these future sensors, provided the basic spectral properties are similar. The VIIRS and GOES-R fire detection algorithms, currently being designed and evaluated, will perform sub-pixel fire characterization (e.g. Schmidt et al., 2011). However, in contrast to MODIS, the NPP VIIRS sensor will provide a finer pixel resolution of about 750 m across the entire scan (nadir and off-nadir), reducing off-nadir pixel growth (Csiszar et al., 2011), and thereby enhancing any potential FRP_f flux product. Due to the large potential for error in the 11 μm BT_{bm}, all future applications (regardless of sensor) will benefit from an improved background brightness temperature selection methodology, potentially based on land cover, topographic, and aspect data sets. Additional satellite observations, such as the Normalized Difference Vegetation Index (NDVI), can also be used to facilitate this analysis.

The initial assessment methodology for the MODIS sub-pixel retrieval can also be applied to future studies. In fact, as sub-pixel retrievals are incorporated into operational satellite missions, increasing quantities of high-resolution validation data will be required. This highlights the value of airborne-sensor-collected fire data, such as those obtained from the AMS sensor aboard NASA's Ikhana aircraft. Currently, the Ikhana is flown over large fire events to support fire suppression operations on the ground. However, these flights also have an enormous scientific value for understanding wildfire behavior and are a potential tool for the direct validation of FRP_f. This study has shown that the greatest potential for error occurs with small sub-pixel fires, but validation data for these events are currently unavailable. Therefore, future airborne missions must focus

on data collection for both large and small fire events over a wide variety of biomass types. In addition, the AMS engineering team is currently exploring modifications to the scanner, which would allow for a large increase in the measured pixel temperatures of the ~4 um channel. This improvement would result in an increased probability of accurately determining FRP estimates from the AMS, thereby facilitating direct validations of MODIS FRP_f and FRP_f flux.

From the operational perspective, there is a growing need for a near-real-time fire intensity rating system (Ichoku et al., 2008a). While these fire-rating techniques are currently based on FRP_p, the incorporation of FRP_f flux will allow future versions to include aspects of fire front size, which will likely help fire suppression teams to allocate their resources more efficiently during a fire emergency. Similarly, the fire weather analysis provided in this study (based on FRP_f flux) can be used to enhance the prediction of changes in satellite-observed fire activity, thereby improving smoke emissions estimates (see Appendix). Perhaps the most valuable application of the sub-pixel retrieval output will be improvements to forecasts of smoke transport. As shown in this study, the FRP_f flux obtained from medium to large fire pixel clusters (> 5-10 pixels) may offer a reliable characterization of thermal buoyancy for estimates of smoke plume height. This information is critical for discerning how far the smoke will be transported and what regions will be affected. Therefore, FRP_f flux, and the sub-pixel algorithm used to derive it, can be implemented to enhance forecasts of air quality and visibility, which may be beneficial to a variety of end users.

Appendix: A Short-Term Predictor of Satellite-Observed Fire Activity in the North American Boreal Forest: Toward Improving the Prediction of Smoke Emissions

A.1 Introduction

Smoke produced by global biomass burning is a key source of aerosol particles, greenhouse gases, and other trace constituents in the atmosphere, which affect the global climate system by altering atmospheric composition and radiative processes (e.g. Randerson et al., 2006; Spracklen et al., 2007; Jordan et al., 2008; Kopacz et al., 2011). The combination of an intense fire event with suitable atmospheric conditions (Kahn et al, 2007, 2008; Val Martin et al., 2010) can allow smoke particles to be injected above the boundary layer, and transported thousands of miles (e.g. Westphal and Toon 1992; Damoah et al., 2005; Sapkota et al., 2005; Duck et al., 2007). These intense fire events, common in the boreal forest of North America, affect air quality and visibility, create health concerns, and may interact with meteorological processes a great distance from a fire (e.g. Wang and Christopher, 2006; Wang et al., 2006, 2012). Several global and regional inventories of biomass burning emissions have been developed over the past decade in an effort to quantify sources and transport of aerosol particles and trace gases. Examples include the Fire Locating and Monitoring of Burning Emissions (FLAMBÉ), produced by the Naval Research Laboratory (Reid et al., 2009), the Fire INventory (FIN), produced by the National Center for Atmospheric Research (Wiedinmyer et al., 2011), the Global Fire Emissions Database (GFED) (van der Werf et al., 2010; Mu et al., 2011), the Global Fire Assimilation System (GFAS) (Kaiser et al., 2011), and the emissions

inventory produced by the National Oceanic and Atmospheric Administration (Zhang et al., 2008, 2012). While the methodology of these emissions inventories varies, the first step for systems operating in near real time is always dependent on observations of active fires, because they are the only consistent source of data over continental scales available in near real time. The observed spatial and temporal patterns of satellite fire observations drive the patterns of estimated smoke emissions from these systems.

Across the globe, biomass-burning activity is highly sensitive to the local climate, including variations in the synoptic weather pattern (e.g. Brotak and Reifsnyder, 1977). In the boreal forest, the fire season is short relative to other ecosystems, and a large majority of fire activity is often concentrated in just a few days of active burning (Hyer et al., 2007). Active fire seasons have been linked to positive 500 hPa geopotential height anomalies (Skinner et al., 1999, 2002), which must persist for approximately 10 days (Fauria and Johnson, 2006). This synoptic environment is conducive to active fire weather conditions at the surface, such as warmer temperatures and suppressed precipitation. The duration of dry conditions typically has a much stronger relation to burned area observations than the total seasonal precipitation (e.g. Flannigan and Harrington, 1988), and therefore sets the stage for active fire weather conditions (Peterson et al, 2010). In addition, low-level instability has been linked to intense fire activity (e.g. Haines, 1988; Potter et al., 2008), and may increase the potential for fire ignition via dry lightning strikes, provided the synoptic environment is favorable (Peterson et al., 2010). Unstable conditions may also result in higher smoke plumes, stronger entrainment of the air near the fires, and faster spread rate, all of which can lead

to “extreme fire behavior” and pyroconvection (e.g. Werth and Ochoa, 1993; Fromm et al., 2010).

While the synoptic environment is a useful first step, additional information is required to characterize variations in localized, short-term meteorological conditions and their effect on fire observations, especially when managing active fires that may threaten life and property. As a result, over 30 years of research has focused the development of several fire weather indices that are currently used operationally in boreal North America. The most well-known of these, the Canadian Forest Fire Danger Rating System (CFFDRS), uses surface temperature, relative humidity, rainfall, and wind speed to derive the biomass moisture content used for assessing daily fire potential and spread in the unique boreal ecosystem (Van Wagner and Pickett, 1985; Van Wagner, 1987; Amiro et al., 2004). The CFFDRS is typically calculating using observations from nearby weather stations, however large regions within the boreal forest are sparsely populated, limiting the available observations. Therefore, a continuous source of weather data via Numerical Weather Prediction (NWP) is highly desirable, especially when trying to develop an automated fire weather forecast in the boreal regions. Mölders (2008) showed that the Weather Research and Forecasting (WRF) model, at a fairly coarse spatiotemporal resolution of 1.0° and 6-hours, can successfully calculate fire weather indices in interior Alaska, assuming the corresponding meteorological variables are accurately predicted. Therefore, the current study explores the potential for using NWP data to capture day-to-day changes in fire activity.

This study is further motivated by the fact that all near-real-time fire emission inventories, including FLAMBÉ, which is used operationally by the Navy Aerosol

Analysis and Prediction System (NAAPS), at the Fleet Numerical Meteorological and Oceanographic Center (the US Navy's forecast center), use observations of fire pixels (known as fire counts) from geostationary and polar-orbiting satellite sensors (e.g. Reid et al., 2009). For numerical forecasting of smoke, however, FLAMBÉ and other models typically assume that the number of observed fire counts does not change throughout the forecast period – a forecast of persistence. This may result in large errors in the final smoke emissions forecast, especially due to changes in local meteorological conditions, which undoubtedly affect fire activity. Therefore, drawing from continued improvements in NWP accuracy, the current study makes the first attempt at developing an automated, NWP-based statistical model that can be used to characterize the effect of a given set of meteorological conditions on the following day's satellite-observed fire counts, including ignition and spread potential, with the ultimate goal of enhancing the estimation and forecast of smoke emissions.

A.2 Study Region and Data

Drawing from a copious base of previous research and the potential for very large, intense fire events, the North American boreal forest is an ideal location for developing a fire count prediction model. The specific study region, located primarily in Alaska, is based on Peterson et al. (2010) and includes the core of the mountainous western boreal forest (Figure A.1). Within the study region, the fire season typically falls between May and September (Skinner et al., 1999; Stocks et al., 2002; Fauria and Johnson, 2006), and the fire seasons of 2004 and 2005 were two of the three largest in the 73-year

observational record (Kasischke et al., 2002). The MODIS sensors aboard the Terra (launched in 1999) and Aqua (launched in 2002) satellites are the primary source of fire count data (MOD14) in this study (Giglio et al., 2003; Giglio, 2010), and the GOES Wildfire Automated Biomass Burning Algorithm (WF_ABBA) fire product (Prins and Menzel, 1994; Prins et al., 1998) is used for independent testing of the algorithm.

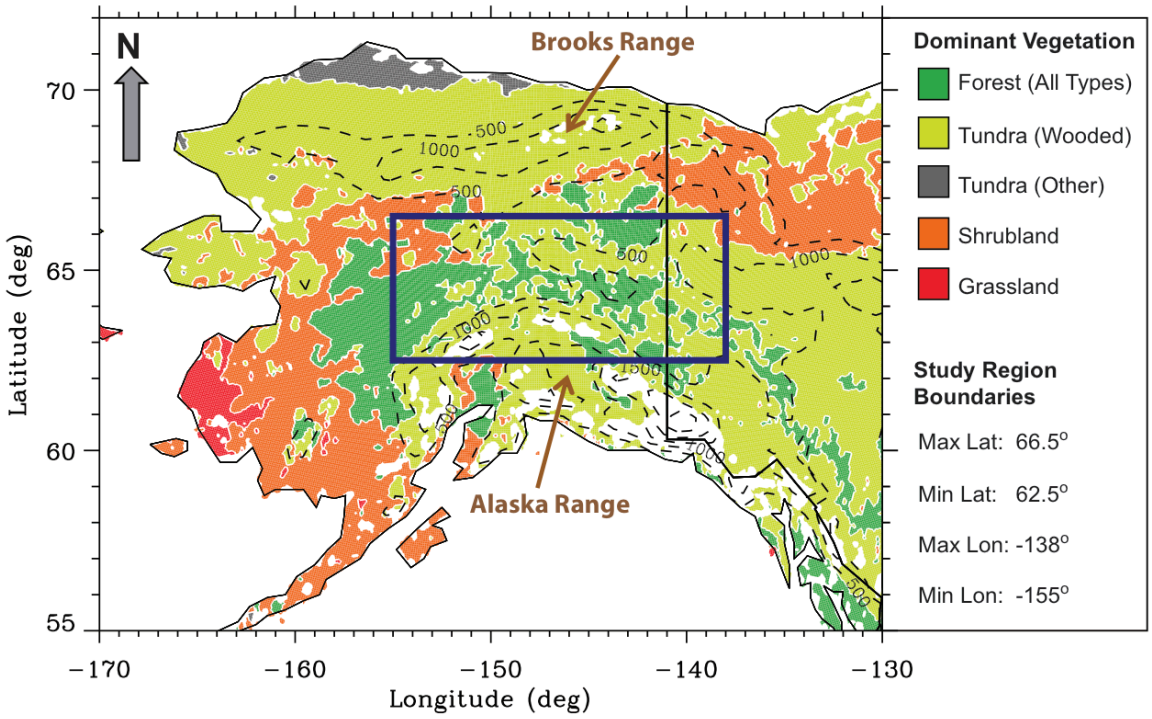

Figure A.1: Map highlighting the boreal study region as a blue box (same as Figure 6.1). The color scheme is based on the dominant vegetation types located within and surrounding the study region. Dashed black contours indicate variations in topography, with a contour interval of 500 meters.

As a polar-orbiting sensor, the MODIS fire detections are not a perfect indicator of fire activity, and have known biases including the inability to detect fires beneath opaque clouds and large variations in pixel size depending on the satellite viewing zenith angle (Masuoka et al., 1998; Gomez-Landesa et al., 2004). However, MODIS data are

best suited for developing a fire prediction model for the study region because: (a) MODIS observed fire counts are a primary source for estimates of fire emissions in FLAMBÉ and FIN, (b) MODIS has the ability to detect smaller fires relative to GOES, and (c) MODIS may be better suited for high-latitude locations than GOES.

For the meteorological component of this study, data are obtained from the North American Regional Reanalysis (NARR), which blends a variety of observational data into Eta model output containing 45 vertical layers across the North American continent with ~32 km grid spacing every three hours (Ebisuzaki, 2004; Mesinger, 2006). The NARR data are also used to produce three modified components of the CFFDRS that are relevant to short-term changes in fire activity, including (1) the fine fuel moisture code (FFMC) describing the moisture content of the fine plant litter in a thin layer on the forest floor, (2) the initial spread index (ISI) created from the combination of the FFMC and surface wind speed, and (3) the fire weather index (FWI), which is created from all six CFFDRS components and describes the overall fire weather situation for the next 24 hours (Van Wagner and Pickett, 1985; Van Wagner, 1987). Drawing from the fire weather relationships identified by Peterson et al. (2010), additional indices are also computed to describe the ignition potential, synoptic influence, and the moisture deficit affecting boreal wildfire activity. Therefore, a large suite of meteorological information, including both single variables and fire weather indices for day 1 (observation) and day 2 (forecast), are available to this study. To facilitate the analysis, the MODIS (or GOES) fire counts are geographically matched onto the mesh of NARR grid boxes and summed for each day, based on the temporal requirements of the CFFDRS (18:00Z to 18:00Z). The CFFDRS are calculated at 10 AM local time (18:00Z) rather than at noon

(operational standard) in an effort to define a single observation time that can be used across the boreal forest of North America and to match the daytime MODIS observations (~10:30 AM and 1:30 PM local time), which typically contain the maximum daily fire activity (Ichoku et al. 2008).

A.3 Statistical Prediction of Fire Growth and Decay

The primary goal of the prediction model is to establish an empirical relationship between weather, fire ignition, and fire evolution, expressed in terms of the change in MODIS fire counts (day 1 vs. day 2) as a function of meteorological variables and fire weather indices. The specific methodology is largely based on a maximum likelihood classification (MLC) score, which is given by

$$\mathrm{MLC_i(x)} = -\ln|\Sigma_i| - (\mathrm{x_{input}} - \mathrm{m_i})^{\mathrm{t}}\Sigma_i^{-1}(\mathrm{x_{input}} - \mathrm{m_i}) \qquad \text{(A.1)}$$

where m_i and Σ_i are the mean vector and covariance matrix for a predetermined number (i) of training classes (Richards and Jia, 2006). This method is widely used in satellite remote sensing for the classification of images (into vegetation, water, clouds, etc.), where m_i and Σ_i are computed from training data (a pre-selected vector of radiometric data $x_{training}$ at various spectral channels) corresponding to each class i. For any given vector of input data (x_{input}), its MLC score, or the likelihood for x_{input} to be in class i, is computed via equation (A.1), and x_{input} is assigned to the class that provides the largest MLC score.

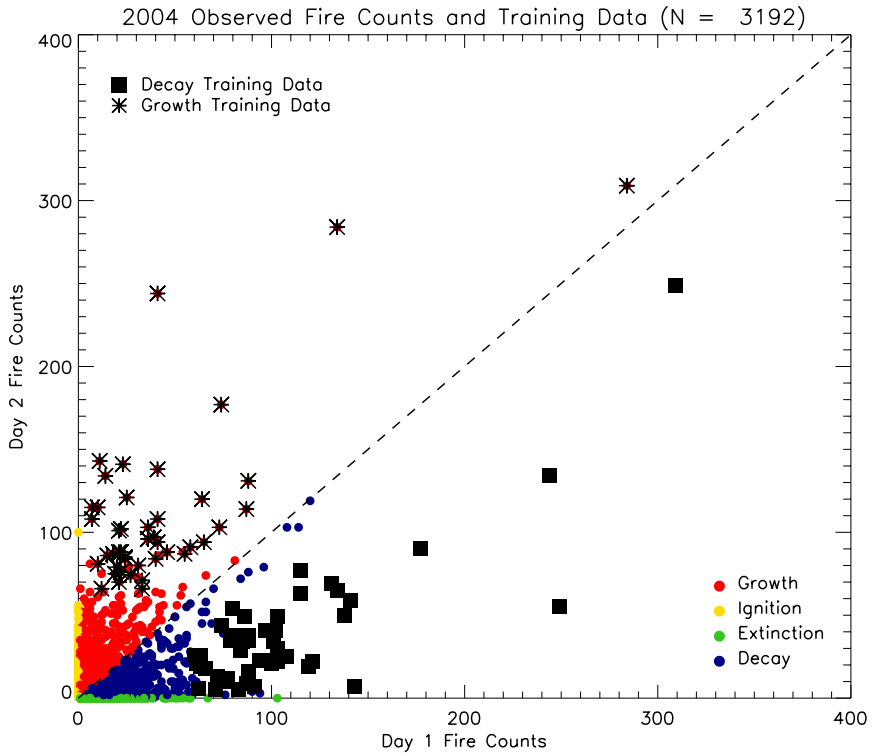

Figure A.2: Comparison between day 1 and day 2 MODIS fire counts observed during the fire season of 2004 in the study region (Figure A.1). The black asterisks and squares respectively highlight the 45 growth and 49 decay training data points. Additional colors separate the remaining cases of growth, decay, ignition, and extinction.

In an analogy to image classification, the MLC technique can be applied to classify the day-to-day change in fire counts based on a variety of meteorological factors that form the elements of the vector x_{input} in equation A.1. To begin, the change in observed MODIS fire counts between day 1 and day 2 are stratified into five classes based on the ~32 km resolution of the NARR: (1) ignition, (2) extinction, (3) growth, (4) decay, and (5) no change. However, with the limitations in satellite fire data (e.g. cloud cover and scan-to-scan variations), the current version of the MLC is largely based on classes (3) and (4). As displayed in Figure A.2, training data are defined from the largest cases, defined by the 75th percentile, within the growth and decay fire count classes, from which m_i and Σ_i are computed. Finally, the x_{input} corresponding to each individual event

is compared to m_i and Σ_i via equation A.1, thus producing the MLC growth (MLC_{grow}) and decay (MLC_{decay}) scores. The complete list of inputs used to create x_{input} is provided in Table A.1, and includes the fire weather indices and other single variables, such as relative humidity and convective available potential energy (CAPE), that display the largest separability between cases of fire growth and decay (illustrated in Figure A.3). Therefore, the modified MLC output determines whether a given fire event best fits the growth or decay fire class.

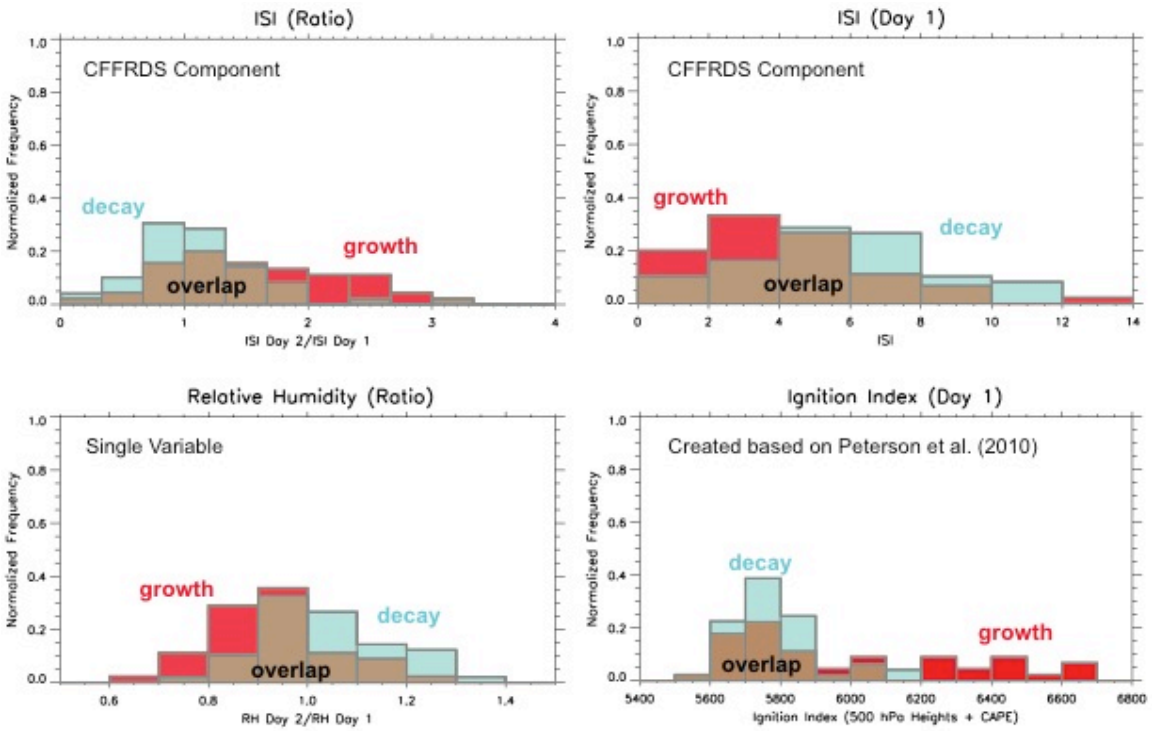

Figure A.3: Histograms showing the separability of the meteorological data corresponding the growth (red) and decay (blue) training data (displayed in Figure A.2) using four examples from Table A.1. Overlap of the growth and decay histograms is displayed in light brown.

Table A.1: Input variables for the MLC.

	Input Variable
Ratios (Day 2/Day 1)	
1	Fire Weather Index (FWI)
2	Initial Spread Index (ISI)
3	Fine Fuel Moisture Content (FFMC)
4	Synoptic Index (500 hPa Heights, ISI, & Dry Days)[1]
5	Moisture Index (Consecutive Dry Days & FFMC)[1]
6	Relative Humidity
Daily Variables	
7	Day 1 Initial Spread Index (ISI)
8	Day 1 Fine Fuel Moisture Content (FFMC)
9	Day 1 Ignition Index (CAPE & 500 hPa Heights)[1]
10	Day 1 Moisture Index (Consecutive Dry Days & FFMC)[1]
11	Day 1 Conv. Available Pot. Energy (CAPE)
12	Day 2 Conv. Available Pot. Energy (CAPE)
Other	
13	Observed Fire Count Tendency (Previous 3 Days)

[1] Additional fire weather indices developed specifically for this study.

While the MLC training data are only derived from fire classes (3) and (4), the MLC_{grow} and MLC_{decay} scores can be computed for all five classes. Figure A.4a shows an example MLC output for the large 2004 fire season, with 3192 NARR grid boxes containing fire pixels in central Alaska. The output is provided in a log scale, and cases of observed growth and decay are evidently concentrated in distinct clusters. However, it is also evident that many NARR grid boxes, especially those with <10 MODIS fire counts on day 1 (small circles in Figure A.4a), are misclassified, which likely results from the uncertainty introduced by scan-to-scan variations of the MODIS sensor. Therefore, emphasis is placed on grid boxes with at least 10 fire counts on day 1 (large triangles in Figure A.4a), ensuring the fire is large in size and likely to appear in a subsequent scan.

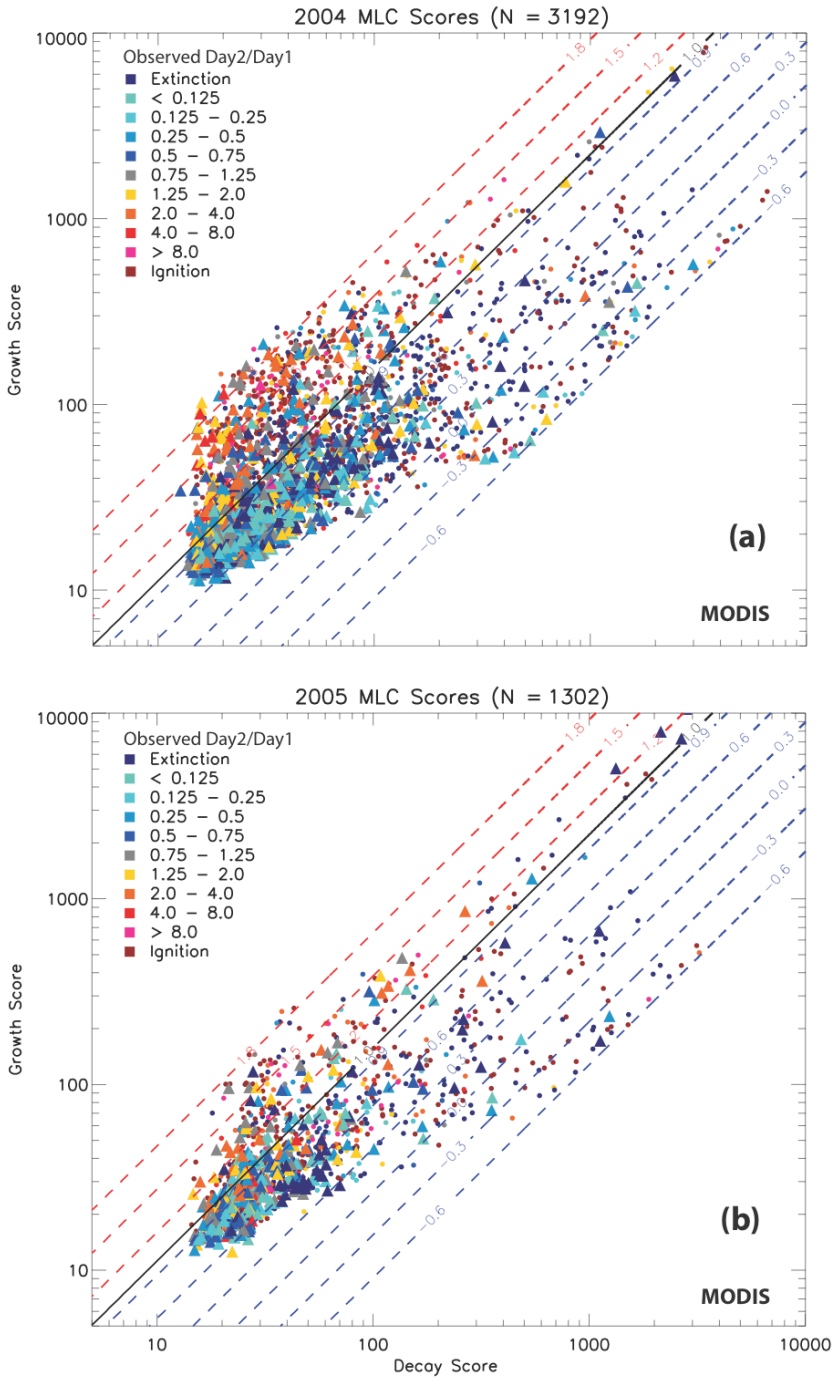

Figure A.4: Output of MLC_{grow} and MLC_{decay} from the 2004 development test and the 2005 independent test, respectively. Small circles indicate where the number of MODIS fire counts on day 1 are <10 and large triangles indicate where the day 1 fire counts are at least 10. The color scheme indicates the observed relative change in fire counts (or ΔFC_{obs}). Red and blue contours indicate the prediction score (or ΔFC_p) obtained from a multiple regression as a function of MLC_{grow} and MLC_{decay}. The black contour indicates no change or a forecast of persistence ($\Delta FC_p = 1$).

The MLC_{grow} and MLC_{decay} scores for the large symbols in Figure A.4a indicate that the training data, which are drawn from limited data samples (e.g. 75th percentile), generally capture the statistics that needed to separate the growth and decay of the fires. However, in a real atmosphere, meteorological variables generally co-vary, and therefore the observed relative change in fire counts (ΔFC_{obs}) is usually determined by how MLC_{grow} and MLC_{decay} are relatively weighted: a larger growth score and small decay score may indicate larger ΔFC_{obs}. As a result, the MLC output is further refined via a linear regression of MLC_{grow} and MLC_{decay} against ΔFC_{obs} to produce a fire count prediction score (ΔFC_p)

$$\Delta FC_p = a_1 \ln (MLC_{grow}) + a_2 \ln (MLC_{decay}) + a_0 \quad (A.2)$$

where a_1 and a_2 respectively equal the slopes for growth and decay (calculated from only the large day 1 cases, triangles in Figure A.4a) and a_0 is a constant. The resulting contour lines of ΔFC_p for all data points are also overlaid on Figure A.4a,b (blue and red parallel lines).

As described above, equations (A.1) and (A.2) are the two key steps in the fire prediction methodology for the meteorological input vector (x_{input}). First, MLC_{grow} and MLC_{decay} are computed using equation (1), and the regression equation (2) is subsequently used to compute ΔFC_p. As shown in Figure A.5a, this ΔFC_p score can then be evaluated against the true ΔFC_{obs} (here the absolute change in fire counts) for all the cases in 2004. It is found that while the ΔFC_p score and ΔFC_{obs} are consistent in terms of sign, there are considerable deviations from the 1:1 line.

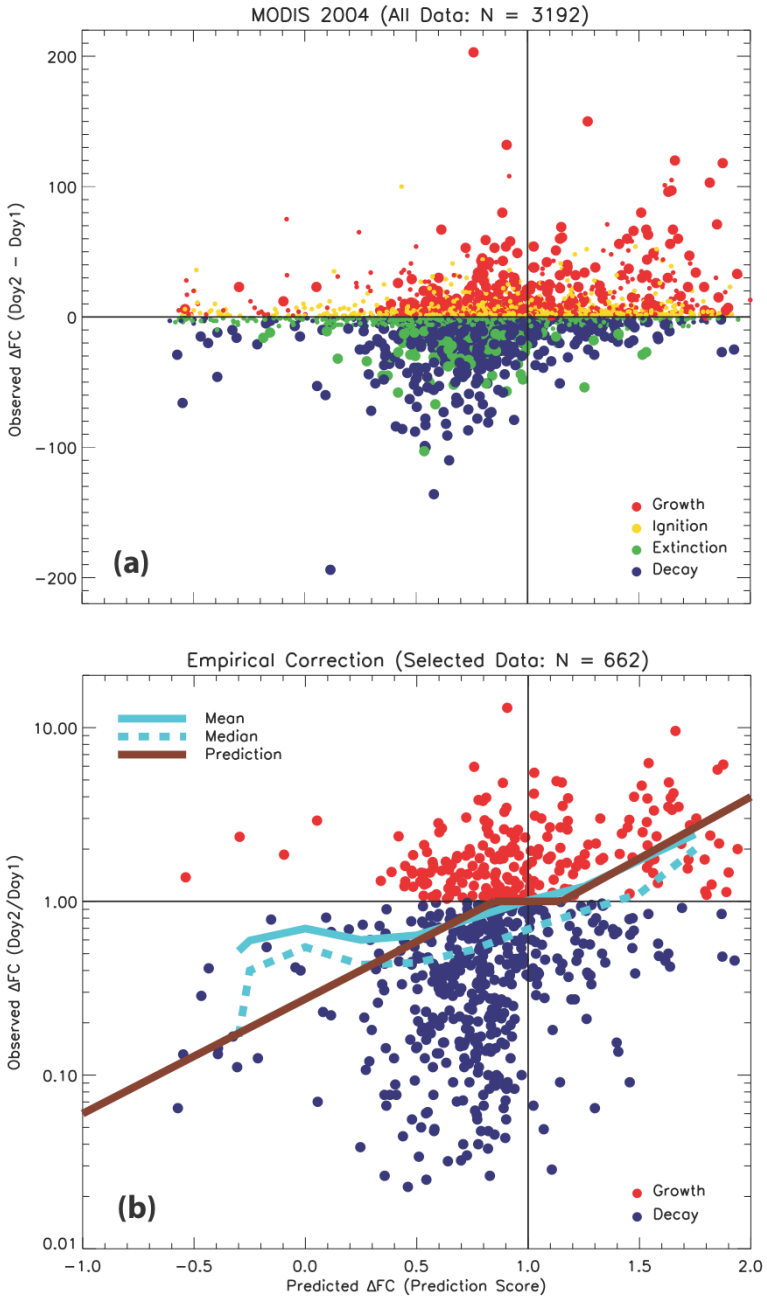

Figure A.5: Results of the multiple regression function displayed as red and blue contours in Figure A.4a. (a) Comparison between the prediction score (ΔFC_p) and the observed absolute change in fire counts (day 2 – day 1, ΔFC_{obs}) for all data points. Small symbols indicate where the number of fire counts on day 1 are <10 and large symbols indicate where the day 1 fire counts are at least 10. (b) Comparison between the prediction score (ΔFC_p) and the observed relative change in fire counts (day 2/day 1, ΔFC_{obs}) with the ignition, extinction, and small day 1 cases (small symbols) removed. The brown line indicates the three-zone quantitative predictor curve that is based on the running mean and median, which are respectively displayed as solid and dashed blue curves.

In order to transform ΔFC_p into a quantitative predictor, the extinction and ignition cases are removed, as well as cases with small day 1 fire counts, and a running mean and median are applied to the remaining cases (blue curves in Figure A.5b). Based on the running mean and median curves, four parameters are empirically estimated to derive the three-zone quantitative predictor (displayed as a brown curve in Figure A.5b): (1) the slope of the growth zone (M_{grow}), which relates ΔFC_{obs} to the predicted growth in fire counts, (2) the slope of the decay zone (M_{decay}), which relates ΔFC_{obs} to the predicted decay in fire counts, (3-4) the lower and upper bounds of the persistence zone (P_{min}/P_{max}), where no change will be forecast. When ΔFC_p is above P_{max}, growth is forecast as $(\Delta FC_p - P_{max})*M_{grow}$, and when ΔFC_p is below P_{min}, decay is forecast as $(\Delta FC_p - P_{min})*M_{decay}$. This quantitative predictor is analogous to a step commonly used in the Model Output Statistics (MOS) for a weather forecast, where NWP output, (here the regression model) is further corrected/adjusted to produce a final forecast (Wilks, 2006). Parameters (1-4) are derived using only the 2004 MODIS fire counts, and subsequently applied to all tests using MODIS and GOES fire count data for 2004 and 2005.

A.4 Evaluating the Fire Count Prediction Model

Results from the 2004 MODIS development test suggest that the fire count prediction model can reduce the RMSE by 13.06% compared to a forecast of persistence – the method currently employed in FLAMBÉ and other emission products (Table A.2). A larger reduction in error is obtained for cases where decay occurred (reduction in RMSE = 24.27%), partly because decay processes are often abrupt, driven by

precipitation. An independent test, conducted by applying the prediction method to the fire season of 2005, shows a smaller but still significant 11.36% reduction in RMSE for cases where decay occurred, as well as an overall reduction in RMSE. However, growth predictions do not seem to offer an improvement over a forecast of persistence. The reason for this is clear from the 2005 MLC scores, displayed in Figure A.4b, where decay cases are found in a distinct cluster while many growth cases are misclassified.

Table A.2: RMSE statistics for the fire count prediction model compared to persistence.

		Persistence	CFFDRS Inputs Only		All Inputs (Table A.1)	
Observation	**N**	**RMSE**	**RMSE**	**% Reduction**	**RMSE**	**% Reduction**
		2004 Development Test (MODIS)				
Overall	3192	18.30	17.55	**-4.10**	15.91	**-13.06**
Growth/Ignition	435	34.58	34.54	**-0.12**	32.86	**-4.97**
Persistence[1]	2328	3.94	4.16	5.58	4.38	11.17
Decay/Extinction	429	34.57	31.41	**-9.14**	26.18	**-24.27**
		2005 Independent Test (MODIS)				
Overall	1302	21.21	20.56	**-3.06**	20.10	**-5.23**
Growth/Ignition	228	33.54	34.03	1.46	34.04	1.49
Persistence[1]	857	4.11	4.17	1.46	4.13	0.49
Decay/Extinction	217	38.10	35.36	**-7.19**	33.77	**-11.36**
		2004 Development Test (GOES)				
Overall	1235	7.56	7.43	**-1.72**	7.10	**-6.08**
Growth/Ignition	236	11.23	11.36	1.16	11.36	1.16
Persistence[1]	768	2.22	2.19	**-1.35**	2.19	**-1.35**
Decay/Extinction	231	12.66	12.13	**-4.19**	11.02	**-12.95**
		2005 Independent Test (GOES)				
Overall	821	7.61	7.56	**-0.66**	7.30	**-4.07**
Growth/Ignition	177	10.97	11.10	1.19	11.08	1.00
Persistence[1]	485	2.20	2.26	2.73	2.19	**-0.45**
Decay/Extinction	159	12.26	11.93	**-2.69**	11.12	**-9.30**

[1] Observed persistence is bounded by ±10 and ±5 fire counts for MODIS and GOES, respectively.

While the fire count prediction methodology was developed using MODIS, the same MLC output (m_i and Σ_i in equation 1) can also be applied to GOES observations, or any other satellite sensor. The resulting GOES application yields similar results to MODIS, with an overall reduction in RMSE for both 2004 and 2005, due in part to large RMSE reductions in cases of decay. The agreement between the MODIS and GOES tests shows that the fire count prediction is a robust fire count prediction for the western boreal forest of North America. In addition, Table A.2 shows that experimenting with various combinations of the day 1 and day 2 components of the CFFDRS alone (e.g. FWI, ISI, and FFMC) does not produce better results than the larger combination of variables displayed in Table A.1, suggesting that the additional considerations of instability (e.g. CAPE), ignition potential, and general synoptic conditions are necessary for x_{input} and the resulting fire count prediction.

A.5 Summary and Discussion

This study has taken the first step toward linking day-to-day changes in satellite fire counts to variations in meteorological variables obtained from NWP using an MLC-based prediction model in the North American boreal forest. While MODIS fire counts are affected by the daily variation of several unavoidable factors, including the location within the scan (viewing angle) and cloud cover, the 2004 development test and the 2005 independent test (for both MODIS and GOES) indicate that the decay prediction alone can be incorporated as an improvement over persistence, thus yielding a forecast of either persistence or decay. The results also show that the current suite of fire weather indices

(e.g. the CFFDRS) must be supplemented with additional variables (e.g. CAPE) to improve prediction accuracy at the daily regional scale.

As shown in this study, forecasting the decay of a fire event is often a simpler problem compared with fire growth, primarily due to the impact from precipitation events. However, several meteorological variables that greatly impact fire ignition and growth, such as lightning strikes, are either unreliable or unavailable in the current NWP output. Therefore, the prediction methodology must be further refined to improve growth predictions, perhaps by accounting for holdover effects from previous lightning strikes or incorporating additional satellite fire products. In the near future, higher resolution (and spatially uniform) fire data from NPP VIIRS (Csiszar et al., 2011) and improved lightning data from GOES-R (http://www.goes-r.gov), can be used in combination with a modified measure of fire radiative power, scaled by the retrieved, instantaneous fire area (Peterson et al., 2012a; Peterson and Wang, 2012), as additional inputs for the fire prediction model. These potential improvements warrant future studies in an effort to achieve the ultimate goal of producing a global fire prediction model (with similar NWP input variables) that can be ingested into the smoke emissions modeling process (e.g. FLAMBÉ), allowing a 24-hour or longer forecast of smoke emissions to be calculated based on the predicted change in fire activity.

Glossary of Symbols and Acronyms

a_0	regression constant (multiple regression)
a_1, a_2	slopes for the fire growth, decay cases (multiple regression)
A_f	retrieved fire area
AGL	above ground level
AMS	Autonomous Modular Sensor
A_p	area of a pixel
ASTER	Advanced Spaceborne Thermal Emission and Reflection Radiometer
AVHRR	Advanced Very High Radiometer
$B(\lambda,T)$	Planck function for a given wavelength and temperature
BIRD	Bi-Spectral Infrared Detection
BL	boundary layer
BT_b	background top-of-atmosphere brightness temperature (in-pixel)
BT_{bm}	MODIS approximated background top-of-atmosphere brightness temperature
BT_{bp}	true in-pixel background brightness temperature provided by the AMS
BT_{TOA}	top-of-atmosphere brightness temperature (general)
BUI	buildup index
CALIOP	Cloud-Aerosol Lidar with Orthogonal Polarization
CAPE	convective available potential energy
CFFDRS	Canadian Forest Fire Danger Rating System
DC	drought code
DMC	duff moisture code

e_{4b}, e_{11b}	background emissivities at 4 and 11 μm
ETM+	Enhanced Thematic Mapper Plus (Landsat)
FFMC	fine fuel moisture code
FIN	Fire INventory
FLAMBÉ	Fire Locating and Monitoring of Burning Emissions
FOV	field of view
FRP	fire radiative power
FRP_f	MODIS sub-pixel-based fire radiative power
FRP_p	MODIS pixel-based fire radiative power
FT_{AMS}	sub-pixel fire brightness temperature provided by the 11 μm AMS channel
F_{tot}	total NARR grid boxes that correspond only to cases where the FRP_f flux exceeded 4000 Wm^{-2}
FWI	fire weather index (derived from all six CFFDRS components)
GFAS	Global Fire Assimilation System
GFED	Global Fire Emissions Database
GOES	Geostationary Operational Environmental Satellite
GOES VAS	GOES VISSR Atmospheric Sounder
GOES-R	Geostationary Operational Environmental Satellite – R Series
HTM	high temperature median
i	predetermined number of training classes (for maximum likelihood classification)
I_{4ref}	reflected solar radiance in the 4 μm channel at the surface
ICT	interchannel comparison test

IFOV	instantaneous field of view
ISI	initial spread index
L_4, L_{11}	observed radiances at 4 and 11 μm (top-of-atmosphere)
M_{decay}, M_{grow}	slope of the decay, growth zones (prediction curve)
MESMA	multiple endmember spectral mixture analysis
m_i	mean vector (for maximum likelihood classification)
MINX	MISR INteractive eXplorer
MIR	middle infrared
MISR	Multi-angle Imaging SpectroRadiometer
MLC	maximum likelihood classification
MLC_{grow}, MLC_{decay}	maximum likelihood classification fire growth, decay score output
MODIS	MODerate Resolution Imaging Spectroradiometer
NAAPS	Navy Aerosol Analysis and Prediction System
NARR	North American Regional Reanalysis
NDVI	Normalized Difference Vegetation Index
NPP	National Polar-orbiting Operational Environmental Satellite System Preparatory Project
N_{tot}	total available NARR grid boxes in each bin box
NWP	numerical weather prediction
P	fractional area covered by fire (usually flaming) within any given pixel
P_{min}, P_{max}	lower, upper bounds of the persistence zone (prediction curve)
PSF	point-spread-function
RAZ	relative azimuth angle

RMSE	root-mean-square error
SBDART	Santa Barbara DISORT Atmospheric Radiative Transfer
SZA	solar zenith angle
T_4	brightness temperature of the fire pixel (4 μm)
T_{4b}	background brightness temperature (4 μm)
T_b	surface kinetic background temperature
T_f	retrieved kinetic fire temperature at the surface
TIR	thermal infrared
TOA	top-of-atmosphere
T_{sfc}	surface kinetic temperature (fire or non-fire)
UAS	unmanned airborne system
VIIRS	Visible Infrared Imaging Radiometer Suite
VZA	viewing zenith angle
WF_ABBA	Wildfire Automated Biomass Burning Algorithm
WRF	Weather Research and Forecasting (model)
x_{input}	vector of input data for the maximum likelihood classification
$x_{training}$	pre-selected vector of training (usually radiometric) data for the maximum likelihood classification
ΔFC_{obs}	observed relative change in fire counts
ΔFC_p	fire count prediction score
λ	wavelength
σ	Stefan-Boltzmann constant
Σ_i	covariance matrix (for the maximum likelihood classification)

τ_4	upward MIR (4 μm) atmospheric transmittance
τ_{11}	upward TIR (11 μm) atmospheric transmittance

References

Ambrosia, V.G., Sullivan, D.V., & Buechel, S.W. (2011a). Integrating sensor data and geospatial tools to enhance real-time disaster management capabilities: Wildfire observations. *Societal Challenges and Geoinformatics, 482*, 1-12

Ambrosia, V.G., & Wegener, S. (2009). Unmanned Airborne Platforms For Disaster Remote Sensing Support. In Pei-Gee Peter Ho (Ed.), *Geoscience and Remote Sensing* (pp. 91-114): InTech

Ambrosia, V.G., Wegener, S., Zajkowski, T., Sullivan, D.V., Buechel, S., Enomoto, F., Lobitz, B., Johan, S., Brass, J., & Hinkley, E. (2011b). The Ikhana unmanned airborne system (UAS) western states fire imaging missions: from concept to reality (2006-2010). *Geocarto International, 26*, 85-101

Amiro, B.D., Logan, K.A., Wotton, B.M., Flannigan, M.D., Todd, J.B., Stocks, B.J., & Martell, D.L. (2004). Fire weather index system components for large fires in the Canadian boreal forest. *International Journal of Wildland Fire, 13*, 391-40

Brotak, E.A., & Reifsnyder, W.E. (1977). Investigation of synoptic situations associated with major wildland fires. *Journal of Applied Meteorology, 16*, 867-870

Byram, G.M. (1959). Combustion of forest fuels. In K.P. Davis (Ed.), *Forest Fire: Control and Use* (pp. 61-89). New York: McGraw-Hill

Cahoon, D. R., Jr., Stocks, B. J., Levine, J. S., Cofer, W. R., III, and Chung, C. C., (1992). Evaluation of a technique for Satellite-derived area estimation of forest fires. *Journal of Geophysical Research*, 97, 805-3814.

Calle, A., Casanova, J.L., & Gonzalez-Alonso, F. (2009). Impact of point spread function of MSG-SEVIRI on active fire detection. *International Journal of Remote Sensing, 30*, 4567-4579

Csiszar, I.A., Schroeder, W., Giglio, L., Justice, C. O., & Ellicott, E. (2011). Quantitative evaluation of active fire detection capabilities from VIIRS. In, *91st American Meteorological Society Annual Meeting*. Seattle, WA

Damoah, R., Spichtinger, N., Servranckx, R., Fromm, M., Eloranta, E.W., Razenkov, I.A., James, P., Shulski, M., Forster, C., & Stohl, A. (2006). A case study of pyro-convection using transport model and remote sensing data. *Atmospheric Chemistry and Physics, 6*, 173-185

Dennison, P.E., Charoensiri, K., Roberts, D.A., Peterson, S.H., & Green, R.O. (2006). Wildfire temperature and land cover modeling using hyperspectral data. *Remote*

Sensing of Environment, 100, 212-222

Diner, D.J., Beckert, J.C., Reilly, T.H., Bruegge, C.J., Conel, J.E., Kahn, R.A., Martonchik, J.V., Ackerman, T.P., Davies, R., Gerstl, S.A.W., Gordon, H.R., Muller, J.P., Myneni, R.B., Sellers, P.J., Pinty, B., & Verstraete, M.M. (1998). Multi-angle Imaging SpectroRadiometer (MISR) - Instrument description and experiment overview. *Ieee Transactions on Geoscience and Remote Sensing, 36*, 1072-1087

Dozier, J. (1981). A method for satellite identification of surface temperature fields of subpixel resolution. *Remote Sensing of Environment, 11*, 221-229

Duck, T.J., Firanski, B.J., Millet, D.B., Goldstein, A.H., Allan, J., Holzinger, R., Worsnop, D.R., White, A.B., Stohl, A., Dickinson, C.S., & van Donkelaar, A. (2007). Transport of forest fire emissions from Alaska and the Yukon Territory to Nova Scotia during summer 2004. *Journal of Geophysical Research-Atmospheres, 112*

Dymond, C.C., Field, R.D., Roswintiarti, O., & Guswanto (2005). Using satellite fire detection to calibrate components of the Fire Weather Index system in Malaysia and Indonesia. *Environmental Management, 35*, 426-440

Dymond, C.C., Roswintiarti, O., & Brady, M. (2004). Characterizing and mapping fuels for Malaysia and western Indonesia. *International Journal of Wildland Fire, 13*, 323-334

Ebisuzaki, W. (2004). National Climatic Data Center Data Documentation for NOAA Operational Model Archive and Distribution System (NOMADS) North American Regional Reanalysis. In G. Rutledge (Ed.) (pp. 1-11). Camp Springs, MD: National Climatic Data Center

Eckmann, T.C., Roberts, D.A., & Still, C.J. (2008). Using multiple endmember spectral mixture analysis to retrieve subpixel fire properties from MODIS. *Remote Sensing of Environment, 112*, 3773-3783

Eckmann, T.C., Roberts, D.A., & Still, C.J. (2009). Estimating subpixel fire sizes and temperatures from ASTER using multiple endmember spectral mixture analysis. *International Journal of Remote Sensing, 30*, 5851-5864

Eckmann, T.C., Still, C.J., Roberts, D.A., & Michaelsen, J.C. (2010). Variations in Subpixel Fire Properties with Season and Land Cover in Southern Africa. *Earth Interactions, 14*

Fauria, M.M., & Johnson, E.A. (2006). Large-scale climatic patterns control large lightning fire occurrence in Canada and Alaska forest regions. *Journal of*

Geophysical Research-Biogeosciences, 111

Filippi, J.B., Bosseur, F., Mari, C., Lac, C., Le Moigne, P., Cuenot, B., Veynante, D., Cariolle, D., & Balbi, J. (2009). Coupled Atmosphere–Wildland Fire Modelling. *J. Adv. Model. Earth Syst., 1*, 1-9

Flannigan, M.D., & Vonder Haar, T. H. (1986). Forest fire monitoring using NOAA satellite AVHRR. *Canadian Journal of Forest Research, 16*, 975-982

Flannigan, M.D., & Harrington, J.B. (1988). A Study of the Relation of Meteorological Variables to Monthly Provincial Area Burned by Wildfire in Canada (1953-80). *Journal of Applied Meteorology, 27*, 441-452

Flannigan, M.D., & Wotton, B.M. (1991). Lightning-ignited forest-fires in northwestern Ontario. *Canadian Journal of Forest Research-Revue Canadienne De Recherche Forestiere, 21*, 277-287

Flasse, S. P., & Ceccato P. S., (1996), A contextual algorithm for AVHRR fire detection. *International Journal of Remote Sensing*, 17, 419-424.

Fromm, M., Lindsey, D.T., Servranckx, R., Yue, G., Trickl, T., Sica, R., Doucet, P., & Godin-Beekmann, S.E. (2010). The untold story of pyrocumulonimbus. *Bulletin of the American Meteorological Society, 91*, 1193-1209

Gao, B.C., Xiong, X.X., Li, R.R., & Wang, D.Y. (2007). Evaluation of the Moderate Resolution Imaging Spectrometer special 3.95-mu m fire channel and implications on fire channel selections for future satellite instruments. *Journal of Applied Remote Sensing, 1*

Giglio, L. (2010). MODIS Collection 5 Active Fire Product User's Guide Version 2.4. In (pp. 1-61): University of Maryland, Department of Geography

Giglio, L., Descloitres, J., Justice, C.O., & Kaufman, Y.J. (2003). An enhanced contextual fire detection algorithm for MODIS. *Remote Sensing of Environment, 87*, 273-282

Giglio, L., & Justice, C.O. (2003). Effect of wavelength selection on characterization of fire size and temperature. *International Journal of Remote Sensing, 24*, 3515-3520

Giglio, L., Kendall, J.D. & Justice, C.O. (1999). Evaluation of global fire detection algorithms using simulated AVHRR infrared data. *International Journal of Remote Sensing, 20*, 1947-1985

Giglio, L., & Kendall, J.D. (2001). Application of the Dozier retrieval to wildfire

characterization - A sensitivity analysis. *Remote Sensing of Environment, 77*, 34-49

Gomez-Landesa, E., Rango, A., & Bleiweiss, M. (2004). An algorithm to address the MODIS bowtie effect. *Canadian Journal of Remote Sensing, 30*, 644-650

Green, R.O. (1996). Estimation of biomass fire temperature and areal extent from calibrated AVIRIS spectra. *Summaries of the sixth annual JPL airborne earth science workshop, JPL Publication 96-4, 1*, 105–113

Grell, G.A., Peckham, S.E., Schmitz, R., McKeen, S.A., Frost, G., Skamarock, W.C., & Eder, B. (2005). Fully coupled "online" chemistry within the WRF model. *Atmospheric Environment, 39*, 6957-6975

Haines, D.A. (1988). A lower atmosphere severity index for wildland fire. *National Weather Digest*, 23-27

Hyer, E.J., Kasischke, E.S., & Allen, D.J. (2007). Effects of source temporal resolution on transport simulations of boreal fire emissions. *Journal of Geophysical Research-Atmospheres, 112*

Hyer, E.J., & Reid, J.S. (2009). Baseline uncertainties in biomass burning emission models resulting from spatial error in satellite active fire location data. *Geophysical Research Letters, 36*

Ichoku, C., Giglio, L., Wooster, M.J., & Remer, L.A. (2008a). Global characterization of biomass-burning patterns using satellite measurements of fire radiative energy. *Remote Sensing of Environment, 112*, 2950-2962

Ichoku, C., & Kaufman, Y.J. (2005). A method to derive smoke emission rates from MODIS fire radiative energy measurements. *Ieee Transactions on Geoscience and Remote Sensing, 43*, 2636-2649

Ichoku, C., Martins, J.V., Kaufman, Y.J., Wooster, M.J., Freeborn, P.H., Hao, W.M., Baker, S., Ryan, C.A., & Nordgren, B.L. (2008b). Laboratory investigation of fire radiative energy and smoke aerosol emissions. *Journal of Geophysical Research-Atmospheres, 113*

Jordan, N.S., Ichoku, C., & Hoff, R.M. (2008). Estimating smoke emissions over the US Southern Great Plains using MODIS fire radiative power and aerosol observations. *Atmospheric Environment, 42*, 2007-2022

Justice, C.O., Giglio, L., Korontzi, S., Owens, J., Morisette, J.T., Roy, D., Descloitres, J., Alleaume, S., Petitcolin, F., & Kaufman, Y. (2002). The MODIS fire products. *Remote Sensing of Environment, 83*, 244-262

Kahn, R.A., Chen, Y., Nelson, D.L., Leung, F.-Y., Li, Q., Diner, D.J., & Logan, J.A. (2008). Wildfire smoke injection heights: Two perspectives from space. *Geophysical Research Letters, 35*

Kahn, R.A., Li, W.H., Moroney, C., Diner, D.J., Martonchik, J.V., & Fishbein, E. (2007). Aerosol source plume physical characteristics from space-based multiangle imaging. *Journal of Geophysical Research-Atmospheres, 112*, 20

Kaiser, J.W., Suttie, M., Flemming, J., Morcrette, J.J., Boucher, O., & Schultz, M.G. (2009). Global Real-time Fire Emission Estimates Based on Space-borne Fire Radiative Power Observations. In T. Nakajima & M.A. Yamasoe (Eds.), *Current Problems in Atmospheric Radiation (IRS 2008) CP1100* (pp. 1-4): American Institute of Physics

Kaiser, J.W., Heil, A., Andreae, M.O., Benedetti, A., Chubarova, N., Jones, L., Morcrette, J.J., Razinger, M., Schultz, M.G., Suttie, M., & van der Werf, G.R. (2011). Biomass burning emissions estimated with a global fire assimilation system based on observed fire radiative power. *Biogeosciences, 9*, 527-554

Kasischke, E.S., Williams, D., & Barry, D. (2002). Analysis of the patterns of large fires in the boreal forest region of Alaska. *International Journal of Wildland Fire, 11*, 131-144

Kaufman, Y.J., Ichoku, C., Giglio, L., Korontzi, S., Chu, D.A., Hao, W.M., Li, R.R., & Justice, C.O. (2003). Fire and smoke observed from the Earth Observing System MODIS instrument - products, validation, and operational use. *International Journal of Remote Sensing, 24*, 1765-1781

Kaufman, Y.J., Justice, C.O., Flynn, L.P., Kendall, J.D., Prins, E.M., Giglio, L., Ward, D.E., Menzel, W.P., & Setzer, A.W. (1998a). Potential global fire monitoring from EOS-MODIS. *Journal of Geophysical Research-Atmospheres, 103*, 32215-32238

Kaufman, Y.J., Kleidman, R.G., & King, M.D. (1998b). SCAR-B fires in the tropics: Properties and remote sensing from EOS-MODIS. *Journal of Geophysical Research-Atmospheres, 103*, 31955-31968

Kelha, V., Rauste, Y., Hame, T., Sephton, T., Buongiorno, A., Frauenberger, O., Soini, K., Venalainen, A., San Miguel-Ayanz, J., & Vainio, T. (2003). Combining AVHRR and ATSR satellite sensor data for operational boreal forest fire detection. *International Journal of Remote Sensing, 24*, 1691-1708

King, M.D., Menzel, W.P., Kaufman, Y.J., Tanre, D., Gao, B.C., Platnick, S., Ackerman, S.A., Remer, L.A., Pincus, R., & Hubanks, P.A. (2003). Cloud and aerosol

properties, precipitable water, and profiles of temperature and water vapor from MODIS. *Ieee Transactions on Geoscience and Remote Sensing, 41*, 442-458

Kopacz, M., Mauzerall, D.L., Wang, J., Leibensperger, E.M., Henze, D.K., & Singh, K. (2011). Origin and radiative forcing of black carbon transported to the Himalayas and Tibetan Plateau. *Atmospheric Chemistry and Physics, 11*, 2837-2852

Koren, I., Remer, L.A., & Longo, K. (2007). Reversal of trend of biomass burning in the Amazon. *Geophysical Research Letters, 34*

Langaas, S. (1993). A parameterized bispectral model for savannah fire detection using AVHRR night images. *International Journal of Remote Sensing, 14*, 2245-2262

Lavoue, D., Liousse, C., Cachier, H., Stocks, B.J., & Goldammer, J.G. (2000). Modeling of carbonaceous particles emitted by boreal and temperate wildfires at northern latitudes. *Journal of Geophysical Research-Atmospheres, 105*, 26871-26890

Lee, T.F., & Tag, P.M. (1990). Improved detection of hotspots using the AVHRR 3.7-um channel. *Bulletin of the American Meteorological Society, 71*, 1722-1730

Li, Z., Kaufman, Y., Ichoku, C., Fraser, R., Trishchenko, A., Giglio, L., Jin, J.-Z., & Yu, X. (2001). A review of AVHRR-based active fire detection algorithms: principles, limitations, and recommendations. In F. Ahern, Goldammer, J., and Juctice, C. O. (Ed.), *Global and regional vegetation fire monitoring from space: planning a coordinated international effort* (pp. 199–225): SPB Academic Publishing

Li, Z., Nadon, S., & Cihlar, J. (2000a). Satellite-based detection of Canadian boreal forest fires: development and application of the algorithm. *International Journal of Remote Sensing, 21*, 3057-3069

Li, Z., Nadon, S., Cihlar, J., & Stocks, B. (2000b). Satellite-based mapping of Canadian boreal forest fires: evaluation and comparison of algorithms. *International Journal of Remote Sensing, 21*, 3071-3082

Masuoka, E., Fleig, A., Wolfe, R.E., & Patt, F. (1998). Key characteristics of MODIS data products. *Ieee Transactions on Geoscience and Remote Sensing, 36*, 1313-1323

Matson, M., & Dozier, J. (1981). Identification of subresolution high temperature sources using a thermal IR sensor. *Photogrammetric Engineering and Remote Sensing, 47*, 1311 –1318

McClatchey, R.A., R. W. Fenn, J. E. A. Selby, F. E. Volz,, & Garing, J.S. (1972). Optical properties of the atmosphere (third edition). In, *AFCRL Environ. Res. Papers No. 411* (pp. 1-108). L. G. Hanscom Field, Bedford. MA

Mell, W., Jenkins, M.A., Gould, J., & Cheney, P. (2007). A physics-based approach to modelling grassland fires. *International Journal of Wildland Fire, 16*, 1-22

Mesinger, F., DiMego, G., Kalnay, E., Mitchell, K., Shafran, P.C., Ebisuzaki, W., Jovi, Du, an, Woollen, J., Rogers, E., Berbery, E.H., Ek, M.B., Fan, Y., Grumbine, R., Higgins, W., Li, H., Lin, Y., Manikin, G., Parrish, D., & Shi, W. (2006). North American Regional Reanalysis. *Bulletin of the American Meteorological Society, 87*, 343-360

Molders, N. (2008). Suitability of the Weather Research and Forecasting (WRF) Model to Predict the June 2005 Fire Weather for Interior Alaska. *Weather and Forecasting, 23*, 953-973

Mu, M., Randerson, J.T., van der Werf, G.R., Giglio, L., Kasibhatla, P., Morton, D., Collatz, G.J., DeFries, R.S., Hyer, E.J., Prins, E.M., Griffith, D.W.T., Wunch, D., Toon, G.C., Sherlock, V., & Wennberg, P.O. (2011). Daily and 3-hourly variability in global fire emissions and consequences for atmospheric model predictions of carbon monoxide. *Journal of Geophysical Research-Atmospheres, 116*

Oertel, D., Zhukov, B., Thamm, H.P., Roehrig, J., & Orthmann, B. (2004). Space-borne high resolution fire remote sensing in Benin, West Africa. *International Journal of Remote Sensing, 25*, 2209-2216

Peterson, D., Wang, J., Ichoku, C., & Remer, L.A. (2010). Effects of lightning and other meteorological factors on fire activity in the North American boreal forest: implications for fire weather forecasting. *Atmospheric Chemistry and Physics, 10*, 6873-6888

Peterson, D., Hyer, E., & Wang. J. (2012b). A short-term predictor of satellite-observed fire activity in the North American boreal forest: toward improving the prediction of smoke emissions. *Atmospheric Environment*, in review

Peterson, D., & Wang, J. (2012). A sub-pixel-based calculation of fire radiative power from MODIS observations: 2. Sensitivity analysis and potential fire weather application. *Remote Sensing of Environment*, in revision

Peterson, D., Wang, J., Ichoku, C., Hyer, E., & Ambrosia, V. (2012a). A sub-pixel-based calculation of fire radiative power from MODIS observations: 1. Algorithm development and initial assessment. *Remote Sensing of Environment*, accepted

Petitcolin, F., & Vermote, E. (2002). Land surface reflectance, emissivity and temperature from MODIS middle and thermal infrared data. *Remote Sensing of Environment, 83*, 112-134

Potter, B.E., Winkler, J.A., Wilhelm, D.F., & Shadbolt, R.P. (2008). Computing the low-elevation variant of the Haines index for fire weather forecasts. *Weather and Forecasting, 23*, 159-167

Pouliot, G., Pierce, T., Zhang, X., Kondragunta, S., Wiedinmyer, C., Pace, T., & Mobley, D. (2008). The impact of satellite-derived biomass burning emission estimates on air quality. In Remote sensing of fire: Science and application, edited by: Hao, W. M., *Proceedings of the society of photo-optical instrumentation engineers*

Prins, E.M., Feltz, J.M., Menzel, W.P., & Ward, D.E. (1998). An overview of GOES-8 diurnal fire and smoke results for SCAR-B and 1995 fire season in South America. *Journal of Geophysical Research-Atmospheres, 103*, 31821-31835

Prins, E.M., & Menzel, W.P. (1992). Geostationary satellite detection of biomass burning in South-America. *International Journal of Remote Sensing, 13*, 2783-2799

Prins, E.M., & Menzel, W.P. (1994). Trends in South-American biomass burning detected with the GOES Visible Infrared Spin Scan Radiometer Atmospheric Sounder from 1983 to 1991. *Journal of Geophysical Research-Atmospheres, 99*, 16719-16735

Randerson, J.T., Liu, H., Flanner, M.G., Chambers, S.D., Jin, Y., Hess, P.G., Pfister, G., Mack, M.C., Treseder, K.K., Welp, L.R., Chapin, F.S., Harden, J.W., Goulden, M.L., Lyons, E., Neff, J.C., Schuur, E.A.G., & Zender, C.S. (2006). The impact of boreal forest fire on climate warming. *Science, 314*, 1130-1132

Reid, J.S., Hyer, E.J., Prins, E.M., Westphal, D.L., Zhang, J.L., Wang, J., Christopher, S.A., Curtis, C.A., Schmidt, C.C., Eleuterio, D.P., Richardson, K.A., & Hoffman, J.P. (2009). Global Monitoring and Forecasting of Biomass-Burning Smoke: Description of and Lessons From the Fire Locating and Modeling of Burning Emissions (FLAMBE) Program. *Ieee Journal of Selected Topics in Applied Earth Observations and Remote Sensing, 2*, 144-162

Ricchiazzi, P., Yang, S.R., Gautier, C., & Sowle, D. (1998). SBDART: A research and teaching software tool for plane-parallell radiative transfer in the Earth's atmosphere. *Bulletin of the American Meteorological Society, 79*, 2101-2114

Richards, J.A., & Jia, X. (2006). Supervised Classification Techniques. *Remote Sensing Digital Image Analysis: An Introduction* (pp. 192-204): Springer-Verlag Berlin Heidelberg

Riggan, P.J., Brass, J.A., & Lockwood, R.N. (1993). Assessing fire emissions from tropical savanna and forests of central Brazil. *Photogrammetric Engineering and Remote Sensing, 59*, 1009-1015

Roberts, G., Wooster, M.J., & Lagoudakis, E. (2009). Annual and diurnal african biomass burning temporal dynamics. *Biogeosciences, 6*, 849-866

Roberts, G., Wooster, M.J., Perry, G.L.W., Drake, N., Rebelo, L.M., & Dipotso, F. (2005). Retrieval of biomass combustion rates and totals from fire radiative power observations: Application to southern Africa using geostationary SEVIRI imagery. *Journal of Geophysical Research-Atmospheres, 110*

Roy, B., Pouliot, G.A., Gilliland, A., Pierce, T., Howard, S., Bhave, P.V., & Benjey, W. (2007). Refining fire emissions for air quality modeling with remotely sensed fire counts: A wildfire case study. *Atmospheric Environment, 41*, 655-665

Roy, D.P., Boschetti, L., Justice, C.O., & Ju, J. (2008). The collection 5 MODIS burned area product - Global evaluation by comparison with the MODIS active fire product. *Remote Sensing of Environment, 112*, 3690-3707

Sapkota, A., Symons, J.M., Kleissl, J., Wang, L., Parlange, M.B., Ondov, J., Breysse, P.N., Diette, G.B., Eggleston, P.A., & Buckley, T.J. (2005). Impact of the 2002 Canadian forest fires on particulate matter air quality in Baltimore City. *Environmental Science & Technology, 39*, 24-32

Schmidt, C.C., Hoffman, J.P., & Prins, E.M. (2011). Detection and characterization of biomass burning in the GOES-R era In, *91st American Meteorological Society Annual Meeting*. Seattle, WA

Schroeder, W., Csiszar, I., Giglio, L., & Schmidt, C.C. (2010). On the use of fire radiative power, area, and temperature estimates to characterize biomass burning via moderate to coarse spatial resolution remote sensing data in the Brazilian Amazon. *Journal of Geophysical Research, 115*, D21121

Schroeder, W., Prins, E., Giglio, L., Csiszar, I., Schmidt, C., Morisette, J., & Morton, D. (2008). Validation of GOES and MODIS active fire detection products using ASTER and ETM plus data. *Remote Sensing of Environment, 112*, 2711-2726

Shephard, M.W., & Kennelly, E.J. (2003). Effect of band-to-band coregistration on fire property retrievals. *Ieee Transactions on Geoscience and Remote Sensing, 41*, 2648-2661

Skamarock, W.C., Klemp, J. B., Dudhia, J., Gill, D. O., Barker, D. M., Wang, W., & Powers, J. G. (2005). A Description of the Advanced Research WRF Version 2. In, *NCAR Technical Note*. Mesoscale and Microscale Meteorology Division, National Center for Atmospheric Research, Boulder, Colorado, USA

Skinner, W.R., Flannigan, M.D., Stocks, B.J., Martell, D.L., Wotton, B.M., Todd, J.B.,

Mason, J.A., Logan, K.A., & Bosch, E.M. (2002). A 500 hPa synoptic wildland fire climatology for large Canadian forest fires, 1959-1996. *Theoretical and Applied Climatology, 71*, 157-169

Skinner, W.R., Stocks, B.J., Martell, D.L., Bonsal, B., & Shabbar, A. (1999). The association between circulation anomalies in the mid-troposphere and area burned by wildland fire in Canada. *Theoretical and Applied Climatology, 63*, 89-105

Smith, A.M.S., Wooster, M.J., Drake, N.A., Dipotso, F.M., & Perry, G.L.W. (2005). Fire in African savanna: Testing the impact of incomplete combustion on pyrogenic emissions estimates. *Ecological Applications, 15*, 1074-1082

Soja, A.J., Al-Saadi, J., Giglio, L., Randall, D., Kittaka, C., Pouliot, G., Kordzi, J.J., Raffuse, S., Pace, T.G., Pierce, T.E., Moore, T., Roy, B., Pierce, R.B., & Szykman, J.J. (2009). Assessing satellite-based fire data for use in the National Emissions Inventory. *Journal of Applied Remote Sensing, 3*

Spracklen, D.V., Logan, J.A., Mickley, L.J., Park, R.J., Yevich, R., Westerling, A.L., & Jaffe, D.A. (2007). Wildfires drive interannual variability of organic carbon aerosol in the western US in summer. *Geophysical Research Letters, 34*

Stephens, S.L., Weise, D.R., Fry, D.L., Keiffer, R.J., Dawson, J., Koo ,E., Potts, J., & Pagni, P.J. (2008). Measuring the rate of spread of chaparral prescribed fires in northern California. *Fire Ecology, 4*, 74-86

Stocks, B.J., Mason, J.A., Todd, J.B., Bosch, E.M., Wotton, B.M., Amiro, B.D., Flannigan, M.D., Hirsch, K.G., Logan, K.A., Martell, D.L., & Skinner, W.R. (2002). Large forest fires in Canada, 1959-1997. *Journal of Geophysical Research-Atmospheres, 108*

Tang, B.H., Li, Z.L., & Bi, Y. (2009). Estimation of land surface directional emissivity in mid-infrared channel around 4.0 μm from MODIS data. *Optics Express, 17*, 3173-3182

Val Martin, M., Logan, J.A., Kahn, R.A., Leung, F.Y., Nelson, D.L., & Diner, D.J. (2010). Smoke injection heights from fires in North America: analysis of 5 years of satellite observations. *Atmospheric Chemistry and Physics, 10*, 1491-1510

van der Werf, G.R., Randerson, J.T., Giglio, L., Collatz, G.J., Mu, M., Kasibhatla, P.S., Morton, D.C., DeFries, R.S., Jin, Y., & van Leeuwen, T.T. (2010). Global fire emissions and the contribution of deforestation, savanna, forest, agricultural, and peat fires (1997-2009). *Atmospheric Chemistry and Physics, 10*, 11707-11735

van der Werf, G.R., Randerson, J.T., Giglio, L., Gobron, N., & Dolman, A.J. (2008). Climate controls on the variability of fires in the tropics and subtropics. *Global*

Biogeochemical Cycles, 22

Van Wagner, C.E., & Pickett, T.L. (1985). Equations and FORTRAN Program for the Canadian Forest Fire Weather Index System. In, *Forestry Technical Report 33*. Ottawa: Canadian Forestry Service, Government of Canada

Van Wagner, C.E. (1987). *Development and structure of the Canadian Forest Fire Weather Index System*. Canadian Forestry Service

Vermote, E., Ellicott, E., Dubovik, O., Lapyonok, T., Chin, M., Giglio, L., & Roberts, G.J. (2009). An approach to estimate global biomass burning emissions of organic and black carbon from MODIS fire radiative power. *J. Geophys. Res., 114*, D18205

Wang, J., Ge, C., Yang, Z., Hyer, E. J., Reid, J. S., Chew, B. N., Mahmud, M., Zhang, Y., & Zhang, M. (2012). Mesoscale modeling of smoke transport over the Southeast Asian Maritime Continent: interplay of sea breeze, trade wind, typhoon, and topography. *Atmospheric Research 7SEAS special issue*, in press

Wang, J., & Christopher, S.A. (2006). Mesoscale modeling of Central American smoke transport to the United States: 2. Smoke radiative impact on regional surface energy budget and boundary layer evolution. *Journal of Geophysical Research-Atmospheres, 111*

Wang, J., Christopher, S.A., Nair, U.S., Reid, J.S., Prins, E.M., Szykman, J., & Hand, J.L. (2006). Mesoscale modeling of Central American smoke transport to the United States: 1. "Top-down" assessment of emission strength and diurnal variation impacts. *Journal of Geophysical Research-Atmospheres, 111*

Werth, P., & Ochoa, R. (1993). The evaluation of Idaho wildfire growth using the Haines Index. *Weather and Forecasting, 8*, 223-234

Westerling, A.L., Gershunov, A., Brown, T.J., Cayan, D.R., & Dettinger, M.D. (2003). Climate and wildfire in the western United States. *Bulletin of the American Meteorological Society, 84*, 595-604

Westphal, D.L., & Toon, O.B. (1991). Simulations of microphysical, radiative, and dynamic processes in a continental-scale forest-fire smoke plume. *Journal of Geophysical Research-Atmospheres, 96*, 22379-22400

Wiedinmyer, C., Akagi, S.K., Yokelson, R.J., Emmons, L.K., Al-Saadi, J.A., Orlando, J.J., & Soja, A.J. The Fire INventory from NCAR (FINN): a high resolution global model to estimate the emissions from open burning. *Geoscientific Model Development, 4*, 625-641

Wilks, D.S. (2006). *Statistical methods in the Atmospheric Sciences*: Academic Press

Wolfe, R.E., Nishihama, M., Fleig, A.J., Kuyper, J.A., Roy, D.P., Storey, J.C., & Patt, F.S. (2002). Achieving sub-pixel geolocation accuracy in support of MODIS land science. *Remote Sensing of Environment, 83*, 31-49

Wooster, M.J. (2002). Small-scale experimental testing of fire radiative energy for quantifying mass combusted in natural vegetation fires. *Geophysical Research Letters, 29*

Wooster, M.J., Roberts, G., Perry, G.L.W., & Kaufman, Y.J. (2005). Retrieval of biomass combustion rates and totals from fire radiative power observations: FRP derivation and calibration relationships between biomass consumption and fire radiative energy release. *Journal of Geophysical Research-Atmospheres, 110*

Wooster, M.J., Zhukov, B., & Oertel, D. (2003). Fire radiative energy for quantitative study of biomass burning: derivation from the BIRD experimental satellite and comparison to MODIS fire products. *Remote Sensing of Environment, 86*, 83-107

Zhang, X., S. Kondragunta, J. Ram, C. C. Schmidt, & H. C. Huang (2012). Near real time global biomass burning emissions product from geostationary satellite constellation. *J. Geophys. Res.*, in press

Zhang, X.Y., Kondragunta, S., Schmidt, C., & Kogan, F. (2008). Near real time monitoring of biomass burning particulate emissions (PM2.5) across contiguous United States using multiple satellite instruments. *Atmospheric Environment, 42*, 6959-6972

Zhukov, B., Briess, K., Lorenz, E., Oertel, D., & Skrbek, W. (2005). Detection and analysis of high-temperature events in the BIRD mission. *Acta Astronautica, 56*, 65-71

Zhukov, B., Lorenz, E., Oertel, D., Wooster, M., & Roberts, G. (2006). Spaceborne detection and characterization of fires during the bi-spectral infrared detection (BIRD) experimental small satellite mission (2001-2004). *Remote Sensing of Environment, 100*, 29-51